

Inspired by Photonics: Switching in Graphene using Gate-Tunable Electron Optics

A Dissertation

Presented to

the faculty of the School of Engineering and Applied Science

University of Virginia

in partial fulfillment

of the requirements for the degree

Doctor of Philosophy

by

Mirza M. Elahi

May 2019

APPROVAL SHEET

This Dissertation
is submitted in partial fulfillment of the requirements
for the degree of
Doctor of Philosophy

Author Signature: Manzure Elahi

This Dissertation has been read and approved by the examining committee:

Advisor: Avik Ghosh

Committee Member: Mircea R. Stan

Committee Member: N. Scott Barker

Committee Member: Mona Zebarjadi

Committee Member: Stephen J. McDonnell

Committee Member: _____

Accepted for the School of Engineering and Applied Science:



Craig H. Benson, School of Engineering and Applied Science

May 2019

To my family

Abstract

Graphene has established itself as a wonder material with a number of intriguing and record-setting properties, such as ultra-high mobility [$\sim 200,000 \text{ cm}^2/\text{V-s}$ on hexagonal Boron Nitride (h-BN) at room temperature], room temperature anomalous quantum Hall, and conductivity quantization. In addition, manipulation of ballistic electron trajectories across graphene junctions explains the photon-like behavior of electrons (electron optics); these electrons, however, are directly tunable with gate fields and can thus show highly unconventional analogs of Snell, Fresnel, and Malus' law. Electrons can be focused without a lens using a p-n junction by making the refractive index negative. The electrons at zero degrees of incidence cannot back-scatter because of symmetry rules, so they transmit through arbitrarily high voltage barriers (Klein tunneling). Using two angled junctions, we can turn back these electrons like a polarizer-analyzer (creating transport-gap). Moreover, this method allows us to control the degree of polarization precisely. All these attributes come together to help us design an electron optics based Klein tunnel switch in graphene [Graphene Klein Tunnel Field Effect Transistor (GKTFET)]. Such a switch (with ideal structure) can help us turn off graphene in the absence of a band-gap, thus making good use of the graphene's high transmission speed. As GKTFET utilizes the angular resolution of electrons, this kind of device is particularly susceptible to geometrical non-idealities. Among the non-idealities, edge roughness, junction roughness, and non-ideal potential (across the junctions) strongly affect the on-off ratio by creating states inside the transport-gap. By comparing experimental data with simulation results, we characterized and benchmarked the edge and junction roughness.

The results show that these non-idealities increase the floor value of the transport gap. Even in the presence of non-idealities, the pseudo-gap in the transport window helps to obtain saturation in the output characteristics; this saturation is similar to that found in conventional logic devices. GKTFET is a suitable candidate for analog applications due to high output resistance as a route to increasing maximum oscillation frequency (f_{max}) without hurting mobility. Furthermore, bilayer graphene (BLG) provides more degrees of freedom for gate control at low scattering by utilizing anti-Klein tunneling. This opens the door for bilayer graphene's application in electron optics based devices.

Acknowledgments

I want to extend my sincere gratitude to my advisor, Avik Ghosh, for guiding me in the right direction towards achieving the qualities of being a good researcher and engineer. He unraveled the art of research and the true sense of accomplishment which it brings in a nearly perfect way. His constant guidance and insights are essential parts of my graduate journey which will also help me in my future life.

I am thankful to my committee members, Mircea Stan, N. Scott Barker, Mona Zebarjadi and Stephen J. McDonnell, for helping me prepare my proposal and defense by providing constructive comments on my work and future career goals.

I consider myself fortunate to have been acquainted with some brilliant colleagues: K. M. Masum Habib, Redwan N. Sajjad, Yaohua Tan, and Yunkun Xie. Countless hours of discussions and arguments with them heavily influenced my thesis work. I would also like to acknowledge the fellow graduate students, past and present, from the VINO group – for their support, feedback, and friendship.

I also appreciate my collaborators at other universities – Cory Dean (Columbia University), James Hone (Columbia University), Philip Kim (Harvard University), Abhay Pasupathy (Columbia University), Azad Naeemi (Georgia Tech.), Shaowen Chen (Columbia University), Zheng Han (Columbia University; Shenyang National Laboratory for Materials Science, China), Ke Wang (Harvard University, University of Minnesota), Gil-Ho Lee (Harvard University; Pohang University of Science and Technology, South Korea), Xiaodong Zhou (Columbia University), Alexander Kerelsky (Columbia University), Chenyun Pan (Georgia

Tech.), and Yihang Zeng (Columbia University) for productive collaboration and fruitful discussions.

I want to express my heartfelt gratitude for all the supports from my friends at UVA, old friends from my school and undergraduate life, teammates from different soccer teams, and colleagues from work life who helped me to grow not only as a researcher but also as a rational human being. Especially, I want to mention a few names – Kawser Ahmed, Zubair Al Azim, Aswad Adeeb, Mahmud Reaz, Md Sariful Islam, Fuad Naser, Samiul Haque, Mostakim Hossain, Muhammed R. Imam, Kamruzzaman Khan, Ramendra Das, Ahmed N. Ahsan, Prinon Mahajan, Shaheen Mahmud, Rajiur Rahman, Jayanta K. Datta, Hasib I. Rafique, Sanjana Solaiman, Golam Kayas, Mahmud Hossain, Anwarul Hoque, Mohammad Nuruzzaman, and Maruful Haque.

I would like to acknowledge the financial support by the Semiconductor Research Corporation (SRC) through the Institute for Nanoelectronics Discovery and Exploration (INDEX), computational resources provided by the University of Virginia Advanced Research Computing Services (ARCS), and consultations with Graduate Writing Lab at UVA Engineering for this work.

It goes without saying, but I'm forever indebted to my parents, Md. Fozle Elahi and Latifa Begum, for giving their wise counsel throughout my life and laying the first stepping stones of the path to where I am today. I also appreciate my brothers, Mirza Mohammad Lutfel Elahi, Mirza Mohammad Mahbube Elahi, and Mirza Mohammad Maqbule Elahi, for their constant support. For the last couple of years in my graduate life, the smiling face of my infant niece, Sanaaz Afrin Elahi, has been a spontaneous source of inspiration. Her cute little face over video calls helped me rejuvenate myself when the hours were darkest. Finally, my sincere thanks to my loving wife, Faeza Hafiz, for her relentless patience and encouragement throughout my graduate life in terms of providing both mental support and intellectual input.

Contents

Contents	i
List of Figures	k
List of Abbreviations	m
1 Introduction	1
1.1 Background	1
1.2 Electrons behaving as photons	2
1.3 Dissertation organization	3
2 Electron optics in graphene p-n junction	5
2.1 Probing electron optics	6
2.2 Abrupt vs. graded junction	13
3 Graphene Klein tunnel field effect transistor (GKTFET)	15
3.1 Utilizing Klein tunneling	16
3.2 Switching in graphene	18
3.3 GKTFET for analog RF applications	23
3.3.1 Pseudo transport gap for saturating output characteristics	24
3.3.2 Improvement in cut-off frequencies	29
3.4 Double source device	35
3.5 Conclusion	38
4 Metrology and optimization: benchmarking non-idealities	40
4.1 Edge roughness	42
4.1.1 Simulation method	45
4.1.2 Results and Discussions	46
4.1.3 Improving device performance	50
4.1.4 Conclusion	51
4.2 Junction roughness	52
4.2.1 Effect of roughness on collimation	52
4.2.2 Effect of roughness on Veselago lensing	55
4.2.3 Conclusions	56
4.3 Characterization of edge roughness	57
4.3.1 Single electron picture, $\sigma_{inj} = 0^\circ$	58
4.3.2 Multi-electron picture ($\sigma_{inj} > 0^\circ$)	59

5	Characterization of graphene p-n junction and Corbino geometry	63
5.1	Graphene p-n junction characterization	63
5.1.1	Contact to contact distance	65
5.1.2	Junction position	69
5.2	Corbino geometry	71
5.2.1	Monolayer graphene	71
5.2.2	Bilayer graphene	73
5.2.3	Exploring devices with bilayer graphene:	74
5.3	Conclusion	75
6	Conclusion	76
	Appendices	79
A	Semi-classical ray tracing simulation	80
B	Geometry improvement of Double Source (DS) device	82
C	Non-Equilibrium Green's Function (NEGF) formalism	84
D	Publications	86
D.1	Journal Articles	86
D.2	Conferences Proceedings	87
	Bibliography	88

List of Figures

2.1	Electron Refraction.	7
2.2	Snell's law for electrons.	10
2.3	Veselago lensing.	14
3.1	Device Schematic of GKTFET	19
3.2	Transfer characteristics using analytical equations	21
3.3	Transfer and output characteristics from semi-classical ray tracing simulations	21
3.4	Transmission engineering in GKTFET	23
3.5	Klein tunnel FET based on dual tilted graphene p-n junctions (GPNJ)	26
3.6	Conductance and output characteristics	28
3.7	Transconductance (g_m) and output resistance (r_{out}) for GFET and GKTFET	30
3.8	Cut-off frequencies for GFET and GKTFET	31
3.9	Graphene quantum switch	36
4.1	Graphene Klein Tunnel transistor using electron optics.	43
4.2	DJT Device characteristics.	44
4.3	Device family schematic.	45
4.4	Low-bias resistance characteristics and effect of edge roughness	48
4.5	Effect of junction roughness	53
4.6	Specularity characterization device schematic	58
4.7	Single electron path for rough edge.	58
4.8	Path of electron for first resonance	59
4.9	Path of electron for second resonance	60
4.10	Specularity vs. edge spreading	61
5.1	Graphene p-n junction characterization	64
5.2	Extracting L_{CC} from the TMF experiment (density matched)	65
5.3	Second resonance	67
5.4	Second resonance analytical expression	69
5.5	Extracting Junction Position	70
5.6	Electron optics in graphene (monolayer) p-n junction with Corbino geometry	72
5.7	Electron optics in graphene (bilayer) p-n junction with Corbino geometry	74
5.8	Monolayer and bilayer graphene device	74
A.1	Potential profile for asymmetric junction	80

B.1 Improving DS device geometry 83

List of Abbreviations

2DEG	2D electron gas
AFM	Atomic Force Microscopy
BLG	Bilayer Graphene
CMOS	Complementary metal-oxide-semiconductor
DFO	Dirac fermion optics
GKT	graphene Klein tunnel
GKTFET	Graphene Klein Tunnel Field Effect Transistor
GPNJ	graphene p-n junction
h-BN	hexagonal Boron Nitride
NEGF	Non-Equilibrium Green's Function
polySi	poly Silicon
TMF	transverse magnetic focusing

Chapter 1

Introduction

1.1 Background

The expansive worlds of electronic and photonic technologies have stayed fairly complementary over the years. Electrons constitute natural candidates for fast switches - Pauli exclusion limits their low-bias conductivity close to the Fermi energy E_F , making them monochromatic. In fact, the spread in electron energy $\sim k_B T$ is bounded by the lower frequency atomic motion in the surrounding reservoirs, making it much smaller than typical E_F and semiconducting band-gaps set by ultra-light electrons. As a result, electron conductivity is readily altered by orders of magnitude (cumulatively spanning almost 19 decades!) simply by gating the Fermi energy in and out of a semiconducting band-gap. The ability to gate electrons and holes separately has led to complementary networks [[Complementary metal-oxide-semiconductor \(CMOS\)](#)] that are low-power and have dominated the semiconducting industry for decades.

Photons, on the other hand, are ultra-light and naturally lead to communication networks, as their high speeds and linear dispersion help them transmit quickly at low distortion. Being bosonic they do not have a naturally occurring large band-gap or antiparticles, which limits the range and nature of optical switching. The fundamentally distinct physical properties of

electrons and photons have kept their domains of application fairly separate.

As electronic devices keep shrinking, there emerges a growing desire for combining switching, i.e., computation, with communication, and thus electronics with photonics. This has historically proved challenging. Electronic switching requires a device-interconnect combination. This combination was built out of differentially doped silicon in the past (e.g. n^+ - p - n^+) and lately of Ohmic metal-semiconducting contacts. Switching set-ups in photonics require solid-state laser sources, optical modulators, advanced photodetectors – a diverse set of components involving different materials needing heterogeneous integration and frequency mixing. All these are absent in any existing foundry, not to mention added multiplexers and mixers to create photonic circuits. It is certainly of intellectual (perhaps even practical) interest to raise the question on what electrons could do if they had photon like dispersions with low mass, and whether that would allow monolithically integrated and scalable computation and communication fabrics based on electronics alone.

1.2 Electrons behaving as photons

A particular enabler of electron optics based devices has been the rapid emergence over the last decade of an entire class of single atom thick 2D materials, ranging from insulators such as [hexagonal Boron Nitride \(h-BN\)](#), silicene, phosphorene and borophene, topological insulators such as Bi_2Se_3 , semiconductors such as MoS_2 and WSe_2 , half-metals such as CrO_2 and CrS_2 , semi-metals such as graphene, metals such as VO_2 and VS_2 and even superconductors such as NbSe_2 . A small class of these 2D materials is Dirac-cone semi-metals with linear dispersion, making them fascinating not only from an application point of view (as ultrafast conductors), but as electronic analogs of photonic devices and relativistic Dirac fermions, bound by an analogous linear dispersion. The purpose of this work is to explore the electronic counterparts

of well known photonic phenomena in such 2D Dirac materials.

For the sake of concreteness, in this work, much of the physics is illustrated with graphene and its progeny (bilayer graphene), although they apply equally to 3D topological insulator surfaces like Bi_2Se_3 with minor changes in nomenclature - viz. replacing pseudospins with real spins. Graphene consists of a single atom layer of carbon arranged in a honeycomb lattice structure. Its discovery [1] has spawned intense research into its intriguing physical properties, such as its photon-like linear dispersion [2], record high mobility [3–5], extremely high thermal conductivity [6], highest mechanical strength [7] and high optical transparency [8]. Spurred by these intriguing properties, the growth and fabrication of graphene devices have progressed rapidly approaching the ballistic limit. A number of recent experiments have demonstrated extremely long mean free paths (up to microns) [5, 9–12], along with ultrahigh mobilities on h-BN (more than $100,000 \text{ cm}^2/\text{V}\cdot\text{s}$ at low carrier density and $25,000 \text{ cm}^2/\text{V}\cdot\text{s}$ at high carrier density) [12], leading to the observation of ballistic transport phenomena such as quantum interference in a Fabry-Pérot cavity [9, 10, 13].

1.3 Dissertation organization

In this work, non-interacting electrons are considered for transport across a [graphene p-n junction \(GPNJ\)](#), created and modulated electrostatically with local gates. In optical parlance, the local gate-dependent potential sets its refractive index [14, 15] while the p-n junction acts as a focusing lens. Since voltage can have any polarity, the corresponding carrier trajectory in [GPNJ](#) imitates Veselago lensing of negative refractive index metamaterials [16] (challenging to realize in optics and typically involving split ring LC circuits). [GPNJ](#) transport can be described very well with such a ray tracing approach. The electron trajectory is accompanied with an equivalent Fresnel's equation, which dictates the transmission probability depending

upon the incident angle [17, 18]. Important similarities (and dissimilarities) with optical transport is described. Transmission probability in GPNJ is shown to be very similar to the transmission of light at an interface, except the velocity of electrons in graphene does not change. This leads to perfect transmission at normal incidence while the optical transmission is never perfect. We then discuss how the conductance can be modulated with gate parameters and geometry (chapter 3), e.g. gate split and the angle of the p-n interface relative to the transport direction. These phenomena have optical analogies, e.g. waveguiding with a cut-off frequency and Malus's law (in a polarizer-analyzer). The gate geometry control implicates interesting device ideas to achieve high current on-off ratio, which is otherwise not available in graphene. Instead of a bandgap, the GPNJ has promised to achieve a transmission gap, a novel way of achieving high modulation of current (section 3.2). Considering geometrical non-idealities, switching in p-n junction based devices can be utilized for analog RF application by imposing saturation in output characteristics utilizing pseudo transport gap (section 3.3). Those non-idealities have been benchmarked and, based on these analyses, optimization of geometry has been introduced (chapter 4). At last, we developed analytical expressions for characterizing graphene p-n junction from experimental data and proposed a method for probing electron optics in bilayer graphene (chapter 5).

Chapter 2

Electron optics in graphene p-n junction

Ballistic electrons in a uniform 2D electron gas (2DEG) behave in close analogy to light [19,20]: electrons follow straight-line trajectories and their wave nature can manifest in a variety of interference and diffraction effects. When transmitted across a boundary separating regions of different density, electrons undergo refraction [21,22], much like light rays crossing a boundary between materials with different optical index. This makes it possible to manipulate electrons like photons by using components inspired by geometrical optics, such as mirrors, lenses, prisms and splitters [14, 21–26]. A particularly striking feature of electronic optics is the prediction of negative refraction [16, 26], which is difficult to achieve in photonic systems but conceptually straightforward for electrons, arising when carriers cross a p-n junction separating electron and hole bands. In optical metamaterials [27–29], negative refraction is enabling exotic new device technologies such as superlenses [30], which can focus beyond the diffraction limit, and optical cloaks [31], which make objects invisible by bending light around them. This chapter is reprinted from Ref. [32] with permission from AAAS coauthored with S. Chen, Z. Han, K. M. M. Habib, L. Wang, B. Wen, Y. Gao, T. Taniguchi, K. Watanabe, J. Hone, A. W. Ghosh, and C. R. Dean.

Graphene has been considered an ideal platform for demonstrating electron optics in the solid state [10,14,33,34]. The high intrinsic mobility allows ballistic transport over micrometer length scales at ambient temperatures [12], while the lack of a bandgap makes graphene p-n junctions highly transparent [9,10,14,35–41] compared with conventional semiconductors. However, experimental demonstration of electron lensing in graphene junctions, has remained conspicuously difficult to realize: separating the junction response from mesoscopic effects (such as contacts and boundary scattering) in transport experiments has proven difficult, while direct probe techniques [42–44] have not provided real-space mapping of transmission across a junction. It is demonstrated that by utilizing a **transverse magnetic focusing (TMF)** measurement scheme in a split gate device, isolation and measurement of direct relationship between the incident and refracted electron trajectories are possible. An electronic Snell’s law relation is confirmed and unambiguous evidence of negative refraction across a p-n junction is found [32]. This technique additionally provides a direct quantitative measure of the transmission coefficient with incidence angle, which is found to be in excellent agreement with theory [35,40]. Together with semi-classical simulations, results reveal the crucial role played by the junction profile for electron optics, and provide a roadmap for new device technologies based on graphene p-n junctions.

2.1 Probing electron optics

For electrons, conservation of the transverse component of the momentum vector, \mathbf{k} , across the junction leads to the Snell’s law relation $k_1 \sin \theta_1 = k_2 \sin \theta_2$, where θ_1 and θ_2 are the incident and refracted angle with respect to the boundary normal, and the Fermi wavevector, $k_i = \sqrt{\pi n_i}$ replaces the optical index of refraction. Since the group velocity is defined by the energy band dispersion $\mathbf{v} = dE/d(\hbar k)$, the sign changes between the valence and conduction bands, making it parallel to the Fermi momentum for n-type carriers, but antiparallel for

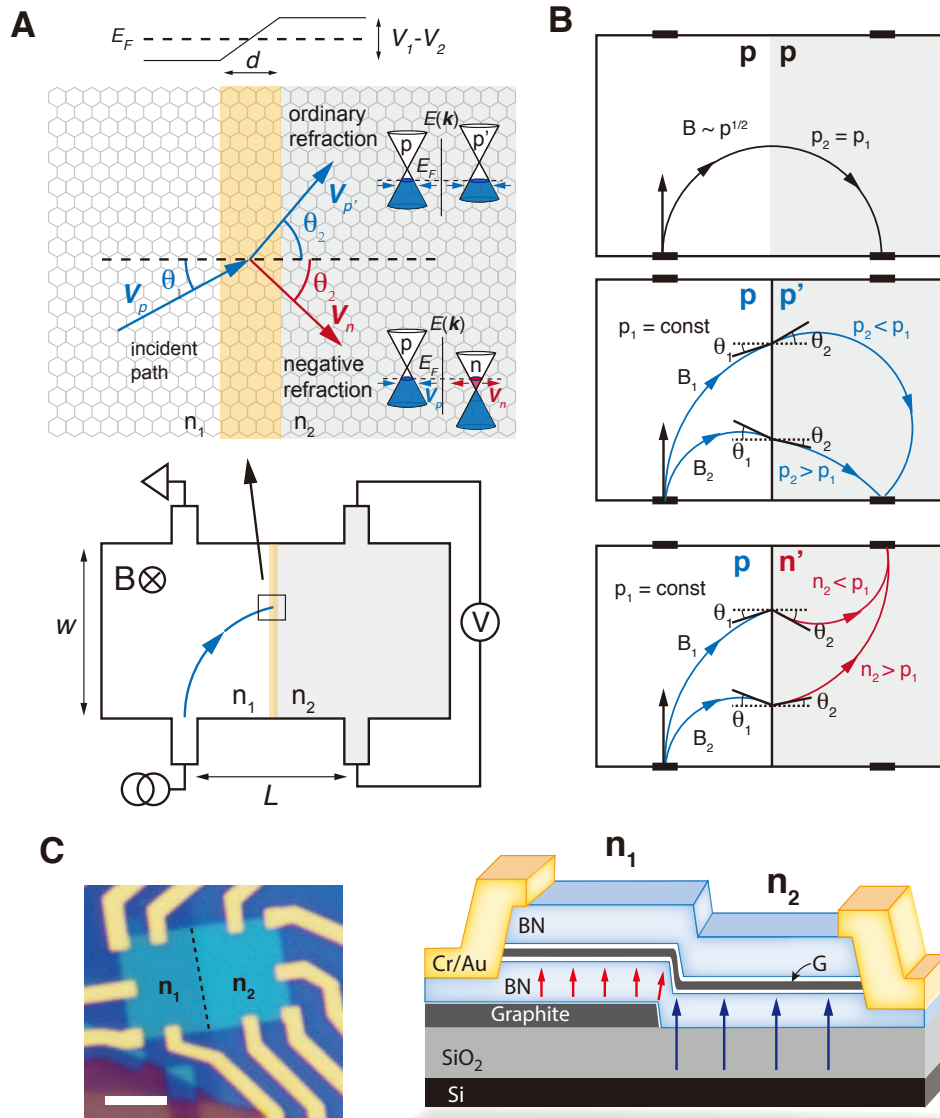


Figure 2.1: **Electron Refraction.** (A) Transverse magnetic field is used to focus electrons onto a split gate junction at variable incident angles. The cyclotron radius, determined by the magnetic field and Fermi momentum (or related carrier density), determines the incidence angle. The density difference across the boundary, induced by the two gate voltages, determines the refraction angle (see text). (B) A resonant path is shown for three example scenarios corresponding to p-p (equal hole density), p-p' (unequal hole density) and p-n' (unequal hole-electron densities). In measurement scheme, density n_1 is fixed, while varying B and n_2 . (C) Optical image (left) and cartoon schematic (right) of split gate device. A naturally cleaved graphite edge is utilized to define an atomically smooth electrostatic boundary. Scale bar is 5 μm . Reproduced from Ref. [32]. Reprinted with permission from AAAS.

p-type. In the case of a p-n junction, the transverse component of the group velocity must change sign in order to conserve momentum [Fig. 2.1(A)] and a negative refraction angle results.

Figure 2.1(A, B) illustrates the device structure used to test this relation. A sample with a junction separating areas of different carrier density is contacted by multiple electrodes in both regions. Under a transverse magnetic field, injected electrons undergo cyclotron motion with radius determined by the Lorentz force. In the absence of a junction, a resonant conduction path (measured as a voltage peak) is realized when the cyclotron radius is half the distance between the current and voltage electrodes, corresponding the condition $B = j \cdot 2\hbar\sqrt{\pi n}/qL$, where, j is the resonant mode number (physically corresponding to the number of half circles that fit between the electrodes), q is the electron charge, B is the magnetic field, L is the distance between the electron emitter and voltage detector, and n is the charge carrier density [45]. In a split-gate geometry, the resonant path depends on the carrier density in each region, and can be considered separately for the three distinct scenarios, shown in Fig. 2.1(B). i) Equal density (n-n or p-p): the junction is fully transparent and there is no refraction, recovering the same resonance condition given above. ii) Same carrier type but unequal density (p-p' or n-n'): positive refraction across the boundary, resulting in a deviation of the resonance condition, but with carriers still focused to the voltage probe on the same side of the sample. iii) p-n' (unequal electron-hole densities): negative refraction occurs and there is a change in the sign of the Lorentz force, causing the charge carriers to be focused to the voltage probe on the opposite side of the sample. The sample geometry fully determines the relation between the magnetic field, B , and charge densities, n_1 and n_2 , of the two gated regions. For all three cases, varying the magnetic field changes the angle of incidence (θ_1) at the boundary, while varying the carrier density on the right side changes both the angle of refraction (θ_2) and the cyclotron radius on the right side. Thus, by mapping out the resonance condition for transmission between the injection and collection electrodes,

we can effectively measure θ_2 as a function of θ_1 to directly verify Snell's law for both positive and negative refraction.

An optical micrograph and schematic cross section of a typical device measured in this study are shown in Fig. 2.1(C) (experiment was done at [Dean Lab](#), Columbia University). Monolayer graphene was encapsulated in [hexagonal Boron Nitride \(h-BN\)](#) and placed half across a few-layer graphite bottom gate that was previously exfoliated onto an oxidized, heavily doped Si wafer. The heterostructure was then plasma etched into a rectangular shape and side-contacted using previously described techniques [5]. Independently voltage-biasing the bottom layer graphite and doped-silicon gates allows us to realize a split gate p-n junction. (Fig. 2.1(B)). Since a naturally cleaved graphite edge is used, the junction is expected to be atomically smooth.

In the [TMF](#) measurement, electrons are injected at one side of the graphite gated region and collected at an electrode on the opposing side, while the voltage is measured across parallel electrodes in the Si gated region [Fig. 2.1(A)]. Figure 2.2(A) shows a typical result, in which the four-terminal resistance is acquired at constant hole density in the injection region ($V_{graphite} = -1$ V corresponding to a density of $6.76 \times 10^{11} \text{ cm}^{-2}$) as a function of detection side gate voltage (V_{Si}) and magnetic field. For the p-p' configuration, both the fundamental resonance and multiple higher order resonant peaks appear. The resonance paths can not be fit to a simple $B \sim \sqrt{n}$ dependence, with the most notable deviation a pronounced kink in the second order resonance. For positive Si gate values (p-n' configuration) only the lowest order resonance mode is observed, with all higher orders apparently suppressed. The resonance peak is opposite in sign compared to the p-p' case. This is a direct signature of carrier focusing to the upper voltage terminal.

A detailed simulation of electron trajectories using semi-classical Billiard model [46, 47]

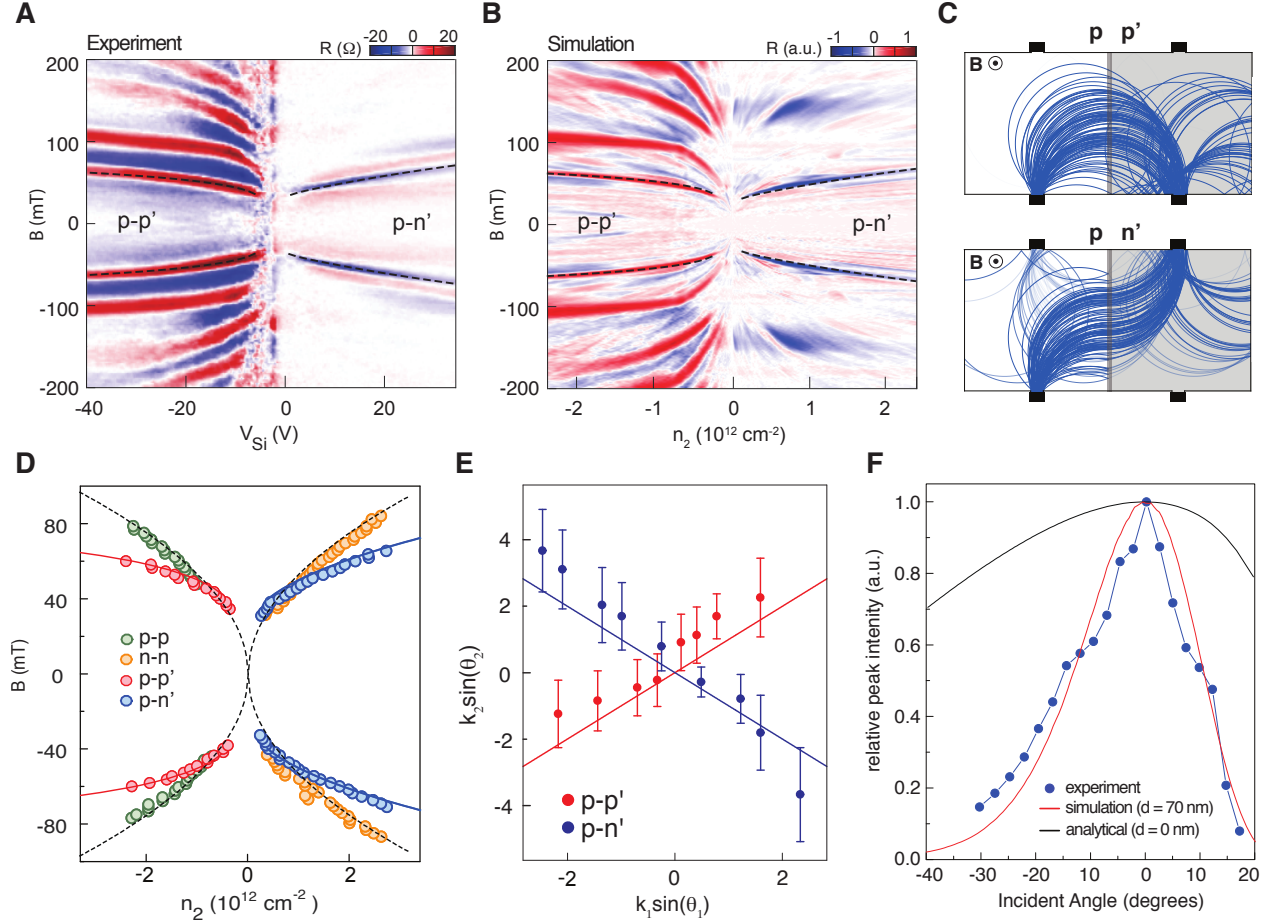


Figure 2.2: **Snell's law for electrons.** (A) Resistance parallel to the junction [corresponding to the measurement configuration shown in Fig. 2.1(B)] versus magnetic field and Silicon gate, V_{Si} . The graphite gate region is fixed to constant p-type carrier density ($V_G = -1 \text{ V}$). (B) Simulation of the experimental data in (A), from ray tracing paths. The horizontal axis in (A) and (B) span over the same range in carrier density. Representative resonant electron trajectories are shown in (C) for a $p-p'$ (top) and $p-n'$ (bottom) junction. (D) Position of the peak plotted as B versus n_2 from the lowest order resonance modes. $p-p'$ and $p-n'$ data points are taken from (A). $p-p$ and $n-n$ data points are determined from a similar map in which the gates are synchronized to maintain a matched density (see SI of Ref. [32]). Dashed line represents the theoretical resonance condition for graphene with matched density (i.e. no junction). Solid red line and blue lines are the theoretical curves deduced from our geometric model, including refraction, for $p-p'$ and $p-n'$ junctions, respectively (see text). (E) Snell's law parameters calculated from the peak points (see text). (F) Transmission intensity versus incident angle. Blue circles correspond to the normalized peak resistance values extracted from (A). Red line is the normalized intensity from simulation for a device with a graded junction of width 70 nm. Black line is the theoretical angle dependence for an abrupt ($d = 0 \text{ nm}$) junction. Reproduced from Ref. [32]. Reprinted with permission from AAAS.

were performed and compared to experiment. In this model, electrons are injected from the source at randomly distributed angles, weighted by a normal distribution of standard deviation $\sigma_{inj} = 12^\circ$. By following their cyclotron trajectories across the junction (junction roughness is not included in the model) the probabilities of reaching the voltage probes are calculated. Transmission across the junction is modeled assuming the electronic Snell's law and momentum filtering [35, 40]. Figure 2.2(B) shows the difference in probability between the two voltage leads from our simulation using identical conditions as the experiment data in Fig. 2.2(A). The simulation matches well with the general features of experimental data for both p-p' and p-n' cases, reproducing the trajectory of all higher order resonances in the p-p' condition, as well as the existence of only a single mode, with opposite sign for the p-n' case. Simulation reveals that the kink in p-p' case results from electron hitting the edge of device at the junction (see SI of Ref. [32] and Appendix A). For p-n' only lowest order is observed as the number of electrons reaching the upper electrode reduces exponentially due to filtering effect every time electrons cross p-n junction [34, 41]. There is some discrepancy in the higher order p-p' resonances between experiment [Fig. 2.2(A)] and simulation [Fig. 2.2(B)]. This is due to uncertainty in the fabricated device geometry (~ 50 nm), finite contact width (~ 300 nm) and edge roughness (see SI of Ref. [32]), all of which become increasingly significant as the cyclotron radius approaches a similar length scale.

In both the experimental and simulated data sets, the trajectory of the lowest order resonance is well captured by our geometric model (dashed lines in Fig. 2a and 2b). Figure 2.2(D) shows this in more detail. The peak position is shown as a function of B and n_2 for both p-p' (red circles) and p-n' (blue circles). Also plotted are similar data points acquired by synchronizing the gates to maintain matched carrier density, giving the trajectory of the p-p (green circles) and n-n (yellow circles) response (see SI of Ref. [32] for the magnetic focusing in the matched density regime). The theoretical resonant peak positions calculated from the geometric model are shown as solid and dashed lines. Excellent agreement is found between

the peak positions and the theoretical curves for all four cases. We note that in generating the theoretical curves we use as inputs only the sample geometry (length $L = 4.05 \mu\text{m}$, and width $W = 3.95 \mu\text{m}$), and the gate efficiencies as extracted from Hall effect measurements (see SI of Ref. [32]), so that effectively there are no free parameters. Three devices of varying sizes and with various gate configurations are measured, all giving similar results. For any combination of B , n_1 , and n_2 , the device geometry dictates the intersection of the electron trajectory with the junction. For each point along the first order resonant peak in Fig. 2.2(A), the angle between the charge carrier trajectory and the boundary normal in each region can be deduced. In Fig. 2.2(E), the corresponding values of $k_i \sin(\theta_i)$ for each region are plotted. The data shows a linear relation with unity slope, confirming the expected Snell's law relation for electrons. For the case of opposite carrier type, the relation shows a negative unity slope, unambiguously confirming negative refraction.

Since the points along the resonance mode can be correlated with the incidence angle, comparing the peak intensity at each point provides a measure of the angular dependent transmission coefficient across the junction. The transmission probability across a p-n junction is theoretically determined by a chiral tunneling process between the bands, and depends strongly on both the incidence angle and effective junction width [35, 40, 48]. For a symmetrically biased junction the transmission probability is given by [35]-

$$T \sim e^{-\pi k_F \frac{d}{2} \sin^2 \theta} \quad (2.1)$$

where θ is the incident and refracted angle, k_F is the graphene Fermi wavevector on two sides, and d is the junction width. In Fig. 2f the normalized peak intensity for the p-n' resonance curve is plotted versus incident angle, with the blue circles and solid red line deduced from the experimental and simulated data sets, respectively. In simulation, the transmission probability for each electron trajectory at the boundary is calculated using a more generalized form of Eq. (2.1) that allows for asymmetric bias [40] (see SI of Ref. [32]).

Experimental results are compared with simulated response for varying junction widths (see SI of Ref. [32]), finding excellent agreement for $d = 70$ nm [Fig. 2.2(F)]. This is consistent with device geometry where a junction width on the order of 60 nm by electrostatic modeling is anticipated. Various σ_{inj} are also tested in simulation but no dependence is found. The results provide strong experimental support for angle-dependent transmission coefficient given by Eq. (2.1), which can be viewed as the electron equivalent of the Fresnel equations in optics, relating the transmitted and reflected probability intensities. It is also demonstrated that wide junctions result in selective collimation [9, 10, 35, 38] of the electron beam compared to abrupt junctions with zero width [solid black line in Fig. 2.2(F)].

2.2 Abrupt vs. graded junction

A striking consequence of negative refraction in graphene is Veselago lensing, in which a planar p-n' junction focuses diverging electrons [14]. Recent transport measurement suggests evidence of this effect [49], but the response is remarkably weak appearing in the signal derivative. Good agreement between simulation and measurement for magnetic focusing, allows one to use the same model to revisit zero-field focusing across p-n' junctions. In Fig. 2.3, the transmission coefficient for the device is calculated from simulation for varying junction widths d . It is found that, owing to the strong reflection of non-normally incident electrons, the transmission decays rapidly with increasing d , and indeed, to realize transmission of 50% compared to abrupt junction requires the d to be less than 5 nm. This experimental constraint provides one explanation for why Veselago-type lensing has been difficult to achieve in previous devices and suggests scaling the p-n' junction width to the few nm limit to be an important criterion for realizing electron optics based on negative refraction in graphene. On the other hand for filtering effect, naturally graded p-n junction device helps.

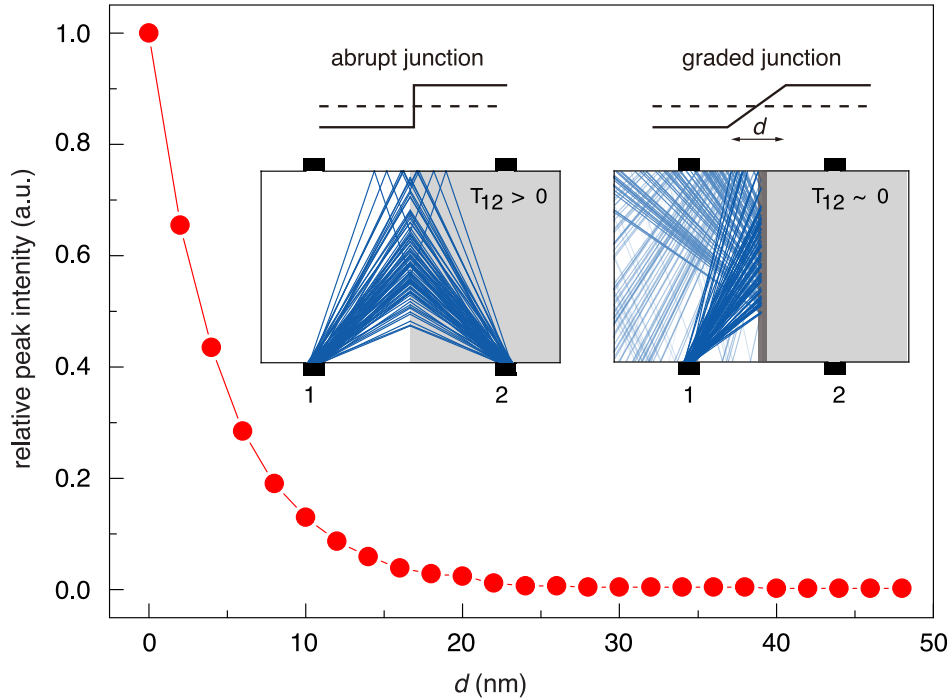


Figure 2.3: **Veselago lensing.** Transmission coefficient for electrons focused across a p-n junction. Main panel shows the variation in transmission probability versus junction width d , determined from simulation. Diverging electrons across a p-n junction theoretically converge to an equidistant point owing to negative refraction. For a graded junction the majority of the electrons are reflected, explaining why Veselago focusing is not observed. Inset shows representative simulated electron trajectories for an abrupt (left) and graded (right) junction. Reproduced from Ref. [32]. Reprinted with permission from AAAS.

Chapter 3

Graphene Klein tunnel field effect transistor (GKTFET)

With the impending end of Moore's Law and the abandonment of the ITRS roadmap, there is now a pressing need to explore new materials, architectures and possibly a new way of computation beyond Boolean logic. Of particular interest is the exploration of fundamental concepts that utilize novel physical mechanisms to beat the Boltzmann limit on the steepness of the gate transfer curve. Complimentary Metal Oxide Semiconductor (CMOS) technology is built around silicon based field-effect devices where the sub-threshold swing ($k_B T \ln 10/q \approx 60$ mV/decade) is fundamentally limited by the tail of the Fermi-Dirac distribution of electrons in the contacts. To overcome this limit, new devices have emerged utilizing novel physical mechanisms such as - Tunnel FETs that abruptly open a tunneling channel in a p-i-n junction [50], negative capacitance based MOSFETs [51] that amplify voltage division across a regular oxide in series with a ferroelectric near transition, metal-to-insulator transition hyperFETs [52] that use opening of a Mott bandgap for voltage amplification at the source, NEMFETs that abruptly withdraw the channel from the drain end [53] and electrostrictive FET [54] that opens a physical gap with a piezoelectric field. All of these systems rely on depletion physics in addition to a gate enhancement of the transmission modes in the channel,

except negative capacitance and hyperFETs where the enhancement happens externally at the voltage input. In this chapter, it is shown how angular filtering in pristine graphene can produce a tunable transport-gap [55, 56] which can in principle beat the Boltzmann limit over several decades while preserving its high mean-free path (section 3.2). Then with more practical considerations analog applications of GPNJ devices are described in section 3.3. At last, a double source device structure is shown to improve on-off ratio in experiments considering geometrical non-ideality (edge roughness) in section 3.4. Part of this chapter is reproduced from Ref. [57] © 2017 IEEE coauthored with K. M. M. Habib, and A. W. Ghosh; Ref. [58] coauthored with Y. Tan, H. Tsao, K. M. M. Habib, N. S. Barker, and A. W. Ghosh; and Ref. [59] coauthored with K. Wang, L. Wang, K. M. M. Habib, T. Taniguchi, K. Watanabe, J. Hone, A. W. Ghosh, G. Lee, and P. Kim.

3.1 Utilizing Klein tunneling

Recently a number of related ideas have appeared on the horizon that specifically seek to exploit alternate properties unique to 2D Dirac cone systems at p-n junctions - such as the ease of interband transfer as well as underlying symmetry rules arising from orthogonal states (pseudospins for graphene, real spins for 3D topological insulator surfaces). Electron trajectories for interband transfer are governed by the plane wave part of the electron wavefunctions, where the conservation of transverse quasi-momentum at the p-n junction leads to negative index and Veselago focusing. The transmittivities on the other hand arise from the atomic (Bloch) part of the wavefunction, where the orthogonality of pseudospins at low energy leads to suppressed back-scattering (Klein tunneling) - perfect electron transmission at normal incidence [17]. It is worth exploring new kinds of switches that specifically capitalize on these unique attributes of graphene, rather than simply mimicking conventional transistors where silicon technology has at the least, the enormous advantage of history, familiarity and inertia.

Initial device ideas with GPNJs often relied on negative index and Veselago lensing. A diverging beam of electrons can be converged to a single point in graphene [14] using an abrupt p-n junction, because the positive velocity components v_x perpendicular to the junction involve opposite wavevector signs $\pm k_x$ even as k_y is conserved. At the same time, wide angle electrons on the higher doped side are totally internally reflected due to their inability to conserve quasimomentum k_y along the junction boundary. The gate voltage on each side acts as a refractive index, allowing us to voltage steer electrons towards or away from a particular contact. However, the switching properties of such a wave-guide are bound to be very modest, even for perfect geometries. A single drain would always pull out electrons regardless of where they focus, while multiple drains would create strong leakage paths (current is always on between the two binary states). The associated Binary Decision Diagram (BDD) logic comes with its own significant energy overheads and significant architectural complexity. Moreover, the sharp and precise injector needed for sharp focusing is hard to fabricate due to inherent challenges with dielectric scaling.

Klein tunneling on the other hand might offer more practical ramifications. Specifically, since the normally incident electrons always perfectly transmit while other angles do not, ramping up the voltage barrier across a p-n junction would collimate the electrons by narrowing their distribution in k-space. This narrowing can be further enhanced with a smoothly varying barrier spanning a split gated junction, where the added Gaussian filtering narrows down the collimation lobe. Subsequently, putting a second junction at a relative angle would reject all the electrons as long as the tilt angle of the second junction exceeds the critical angle of the filtered and collimated electrons.

3.2 Switching in graphene

Graphene Klein tunnel field effect transistors (GKTFET) [60] utilize the electrons' pseudospin-momentum locking across p-n junctions to modulate electron transmission with the gate dependent barrier height. Due to the angular filtering, two junctions at different angles to each other open up a transport-gap, eventually turning off the device (off state, $n^+ - p - n^+$) [60], assuming all reflected electrons make it back to the source. In the on state ($n^+ - n - n^+$) however, the device acts like a homogeneous graphene sheet with high mobility and small gap. This combination will be referred as biasing scheme I where the central gate bias is varied (i.e. both junction barriers simultaneously). In biasing scheme II, the on state is defined as $n^+ - p^+ - p$ and off state as $n^+ - p^+ - n$, meaning only the barrier at the second junction varies. The device structure is shown in Fig. 3.1(A). The channel can be divided into three regions, where the first and second regions form a junction parallel to the source, while the second and the third form a junction at a relative angle δ . This has been realized in Fig. 3.1(A) with a local gate at region two and a Si back gate for regions one and three. Figure 3.1(A,B) is for biasing scheme I. For biasing scheme II, two local gates are needed (region one and three) and a back gate for region two [inset in Fig. 3.2(B)]. In edge free graphene structures (e.g. with absorbing boundaries), such a Graphene Klein Tunnel transistor (GKT) shows excellent promise as a low power switching device, since the gate bias creates a variable transport gap [55].

In many ways, the GKTFET acts like a tunnel field effect transistor (TFET), except its tunneling matrix has additional symmetry rules arising from the chiral variation of its pseudospins. Unlike conventional TFETs, the on current of a GKT is not limited by tunneling and set by current flow across uniformly gated graphene, while the off current is low because of the opening of a *gate tunable transport gap*. Indeed, on-off ratios $\sim 10^4$ and sub-threshold swings of < 60 mV/decade (arising again from the tunable transport gap) are obtained in our simulations for edge free structures about $1 \mu\text{m}$ wide, where the junction transmissions are assumed to be completely decoupled [60]. The low subthreshold swing arises from the gate-

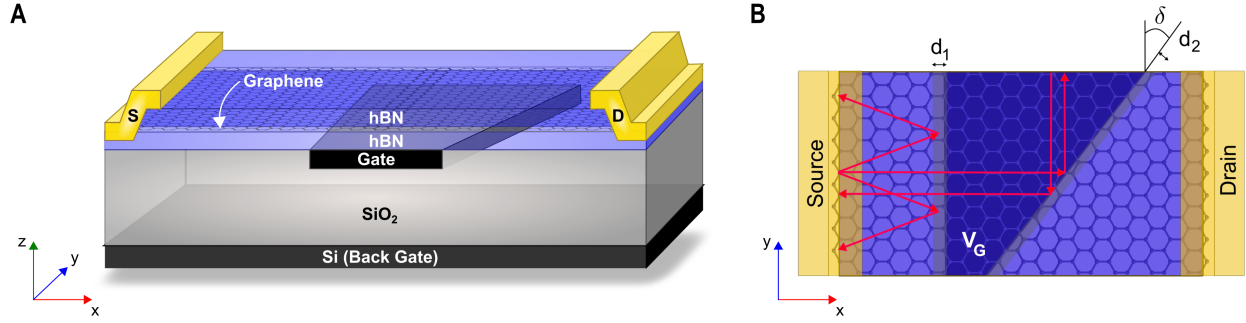


Figure 3.1: **Device Schematic of GKTFET.** (A) Schematic Klein tunnel transistor based on dual tilted graphene p-n junctions. SiO_2 is grown on top of Si back gate, after which polysilicon/graphite gates are deposited/stamped (in case of graphite gate one extra layer of hBN is used underneath it [32]). A graphene flake is sandwiched between hBN and then transferred on top of the SiO_2 . (B) Top view of the patterned gate. First junction is aligned with source whereas the second junction is tilted at an angle δ . d is the split length of the junctions ($d = 80\text{nm}$ in our simulations which is comparable to experiment [32]). Red arrows show the schematic path of electrons in the off state (more details emerge from ray tracing, not shown). Each junction only transmits electrons perpendicular to it. Thus in off state the first junction acts as a collimator and second one as a filter. Since the collimations disappear for homogeneous gating, we have a gate tunable transport-gap that is at the heart of low SS and high on-off ratio while retaining high mean free path with pristine graphene. This figure is reproduced from Ref. [57] with permission © 2017 IEEE.

ability of the mode-averaged transmission function in addition to the electrostatic depletion of charge, which serves to provide an internal voltage gain mechanism.

The simplest way to calculate current is by analytically coupling the transmissions across two junctions including 1-D back and forth scattering (Fig. 3.2) and putting that in Landauer equation.

$$I_{DS} = \frac{2q}{h} \int T_{av} M [f(\mu_S) - f(\mu_D)] dE \quad (3.1)$$

where M is the number of modes, T_{av} is their mode-averaged transmission, q is the charge of the electron, h is the Planck's constant, f is the Fermi-Dirac distribution, and $\mu_{S,D}$ are the bias-separated electrochemical potentials in the source and drain. The mode-averaged transmission T_{av} and number of modes M at energy E are controlled by the potential drops on the channel V_{GS} .

More detailed is semi-classical ray tracing supplemented with analytical expressions for chiral tunneling across the junction [32], which accounts for edge reflections (Fig. 3.3). In all cases considered, we assume the width of the device is 1 μm . From both approaches, the number of modes M per spin per valley, as well as mode averaged transmission T_{av} between source (S) and drain (D) can be extracted. The current (I_{DS}) is calculated using the Eq. (3.1). Biasing scheme I shows high on-off ratio [Fig. 3.2(A)] when the barrier is eliminated, but a low SS as the barriers work against each other. On the other hand biasing scheme II shows lower on-off ratio since the front barrier is unchanged, but gets us SS \approx 60 mV/decade [Fig. 3.2(B)] since the transport gap is tuned directly. In fact, biasing scheme II shows SS $<$ 60 mV/decade at least over two decades of I_{DS} (maximum four decades for low bias) [Fig. 3.2(C)]. However, the key assumption is that all electrons reflected at the second barrier successfully make it back to the source (in the quasi-ballistic regime, electrons can flow either way at the same energy. A positive drain bias simply injects higher energy electrons from the source compared to the drain). For practical sized geometries, transport is simulated with the ray tracing method [32] (Fig. 3.3). Due to multiple bounces at the edges after reflection from the second junction, the on-off ratio degrades to 10^2 [Fig. 3.3(A)]. In effect, these reflections can give electrons a second chance at squeezing through the tilted barrier, thereby creating states inside the transport-gap and turning it into a pseudogap. Figure 3.3(B) shows the optimized δ ($=45^\circ$) for minimum leakage current. While the pseudogap hurts the on-off ratio, it causes the output characteristic to saturate [Fig. 3.3(C)] [61] which increases the output resistance beyond the contact resistance and provides a much needed gain for RF device applications. The high output resistance r_{out} of a saturating I_D - V_D increases the unity power gain cut off frequency f_{max} needed for driving circuits such as oscillator applications. At the same time, the high mobility for pristine graphene provides us with high transconductance g_m and high unity current gain cut off frequency f_T needed for amplifiers [58]. Analog applications are described in more details in section 3.3.

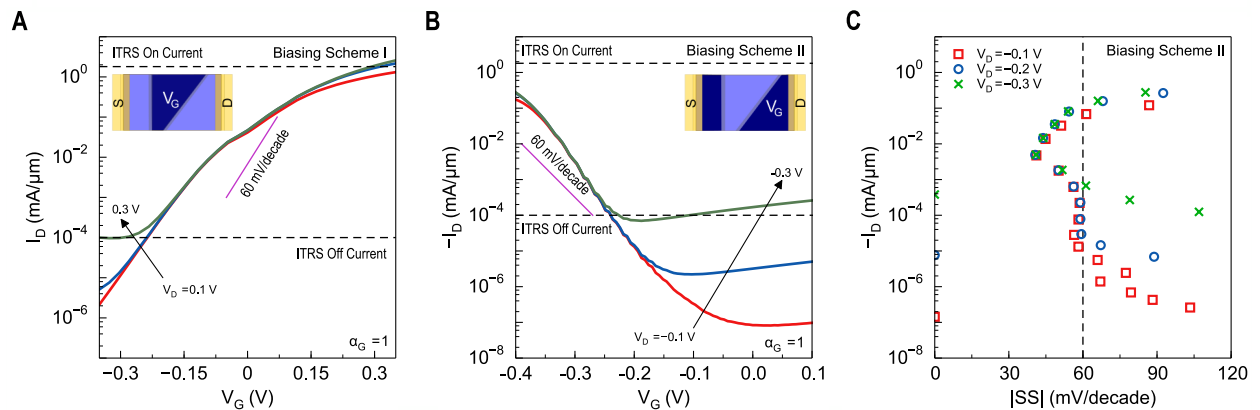


Figure 3.2: **Transfer characteristics using analytical equations without edge scattering** (gate transfer factor $\alpha_G = 1$ to show the intrinsic SS). **(A)** I_D vs. V_G for biasing scheme I ($n^+ - n - n^+$ (on) to $n^+ - p - n^+$ (off)). On-off ratio $> 10^4$ due to homogeneous graphene in on state, while $SS > 60$ mV/decade as both barriers diminish together. **(B)** I_D vs. V_G for biasing scheme II ($n^+ - p^+ - p$ (on) to $n^+ - p^+ - n$ (off)). On-off ratio $< 10^4$ as one junction still exists in the on state, while $SS < 60$ mV/decade as a single barrier is modulated. **(C)** SS extracted from (B). $SS < 60$ mV/decade over at least two decades of current change (high bias) and four decades for low bias. This figure is reproduced from Ref. [57] with permission © 2017 IEEE.

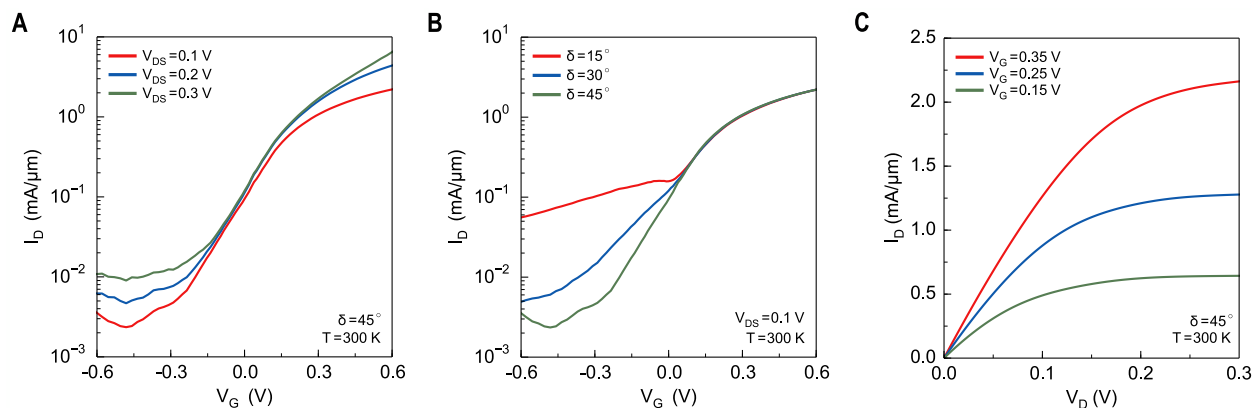


Figure 3.3: **Transfer and output characteristics from semi-classical ray tracing simulations** (i.e., including edge scattering) (gate transfer factor $\alpha_G < 1$, EOT = 1 nm for biasing scheme I). **(A)** I_D vs. V_G for $\delta = 45^\circ$. Due to the presence of edges, electrons reflected from the second junction tend to bounce around and leak through the junction into the drain in the off state. The on-off ratio degrades to 10^2 . **(B)** Device performance depends on the tilt angle because of angular filtering. $\delta = 45^\circ$ gives us the best performance (low off current). **(C)** I_D vs. V_D . Even with edge scattering, the compromised pseudogap at energies away from equilibrium Fermi level ($n^+ - n - n^+$), suffices to saturate the current in pristine graphene. This figure is reproduced from Ref. [57] with permission © 2017 IEEE.

There is now experimental support for the key physics of junction resistance enhancement with angular filtering [59,62]. The overall performance of the GKTFET ultimately depends on the tunability and robustness of the transport-gap. Unlike a regular TFET where tunneling underlies the on current, GKTFETs control Klein tunneling as a way to reduce the off current with momentum rather than energy filtering [Fig. 3.4(A,B)]. The single-crystal nature of graphene avoids traps or Auger recombination that complicates TFET off currents. The transport gap was estimated to be $\Delta V_G 2 \sin \delta / \cos^2 \delta$ from analytical calculations for a point-contact with a hole across a PN junction [55]. For the geometry mentioned, a good approximation to the ray tracing result is to replace $\delta \rightarrow \delta - 3\sigma$, σ being the collimation angle [Fig. 3.4(C)]. This modification comes from the fact that every point injects electrons from the extended source and the first junction filters all electrons other than those with $|\theta_i| > 3\sigma$ (0.99 confidence interval for a Gaussian function), where θ_i is the incident angle. Thus the effective angle for the second junction reduces. Although the tunability reduces, the transport-gap is still larger than the potential barrier created, thus making this device suitable for steep SS if the reflected electrons can be turned towards the source.

GKTFETs operate in a fundamentally different way than MOSFETs and TFETs, by using momentum rather than energy filtering. Oxide trap charges in III-V and at the interface between two channel materials in heterogeneous TFETs compromise energy filtering through band-to-band tunneling using multiphonon and Auger processes. Similarly, non-idealities such as edge roughness, junction roughness, and impurity scattering compromises angular filtering that underlies the GKTFET. Aggressive collimation ($\sigma < 5^\circ$) is needed to maintain a high on-off ratio in GKTFETs. Another challenge is the overall contact resistance for 2D materials that must be reduced below $\sim 100\text{-}200 \Omega\text{-}\mu\text{m}$ to allow junction filtering to be meaningful. However, one encouraging feature is that an on-off ratio of ~ 10 , already seen for GKTFETs, is sufficient for analog RF applications while clearly being inadequate for digital.

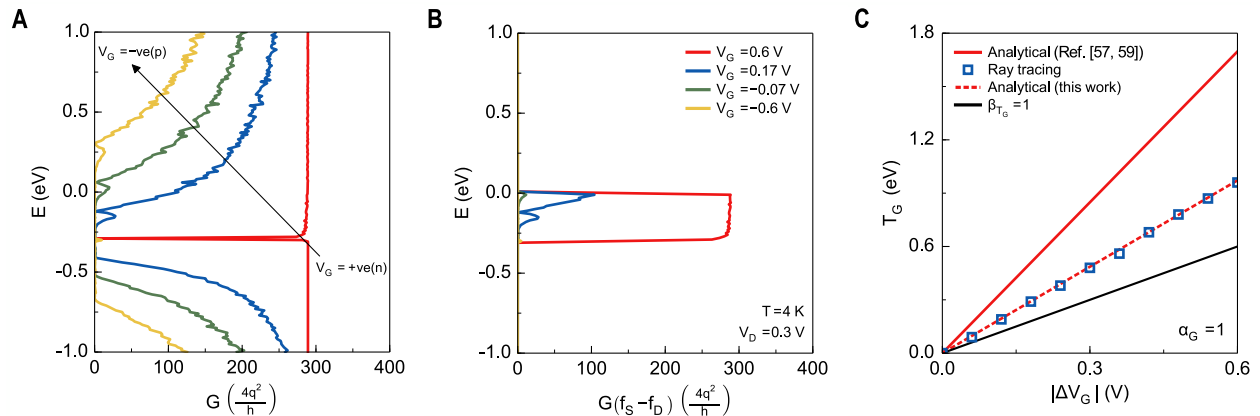


Figure 3.4: **Transmission engineering in GKTFET** (semi-classical ray tracing simulation, biasing scheme I). **(A)** An energy dependent conductance plot clearly shows that a pseudo transport-gap opens up for n-p-n combination, **(B)** Conductance multiplied by the Fermi window available ($qV_D = \mu_S - \mu_D = 0.3$ eV). The ultimate goal is to reduce the area under these curves to turn the device off. Due to the transport-gap, overall area reduces gradually from $V_G = +ve$ (n-type) to $V_G = -ve$ (p-type), **(C)** Pseudo transport-gap (T_G) vs. built in channel voltage (equal to ΔV_G for $\alpha_G = 1$) at the junction. Here $\beta_{T_G} (= T_G/q|\Delta V_G|)$ is the voltage amplification factor that underlies low SS. Analytical formula from [55, 60] is the red solid line, blue square shows the data from ray tracing simulation. Ref. [55, 60] assumed a point source and ignored edge scattering of reflected electrons. The pseudo gap for ray-tracing simulation is less than the original prediction with $\delta_{eff} = \delta - 3\sigma$ (red dash line), keeping it still quite tunable for low SS ($\beta_{T_G} > 1$). This figure is reproduced from Ref. [57] with permission © 2017 IEEE.

3.3 GKTFET for analog RF applications

Graphene is a promising channel material for radio frequency (RF) applications [63–66] due to its intrinsic high carrier mobility and long mean free path [3, 4, 12, 67]. In fact, graphene RF devices have been reported to achieve f_T 's larger than 300 GHz for sub-100 nm channels [68, 69]. However, the gaplessness of graphene makes its output resistance low, arising from the lack of any current saturation. Consequently, the power gain cut-off frequency f_{max} of most of the reported GFETs are much lower than their f_T , and does not scale with channel length [63–65] [Fig. 3.8(F)] because of the non-scalability of the dominant contact resistances.

Efforts to improve the f_{max} of graphene FETs (GFETs) have focused on reducing the input resistance and introducing current saturation. Recent work by Guo *et al.* [70] showed an

improved f_{max} in GFETs by significantly reducing the gate resistance using a T-shaped gate. To obtain current saturation in GFETs, an energy bandgap can in principle be introduced in graphene, such as by applying symmetry breaking strain [71] or using quantum confinement in graphene nanoribbons and nanotubes [72]. Furthermore, scattering process in a long graphene channel can also introduce natural current saturation [73]. However, those band gap opening mechanisms significantly reduce the carrier mobility due to the distorted bandstructure or carrier scattering events [74]. Thus a technique which introduces a transport gap in graphene without degrading the carrier mobility [55, 60] would be quite unique and highly desirable for graphene-based RF applications.

3.3.1 Pseudo transport gap for saturating output characteristics

The pseudo transport gap in GKTFETs can be used for RF applications to overcome the lack of current saturation in traditional GFETs. To understand the characteristics of GKTFETs, we performed semiclassical ray tracing calculations coupled with analytical models for Klein tunneling to model electron transport in GKTFETs [32]. The critical device parameters for a given geometry are extracted from finite element electrostatic calculations in order to estimate the cut-off frequencies. According to calculations, even a pseudogap suffices to allow GKTFETs to have distinct current saturation [61] and considerably larger output resistance r_0 than conventional GFETs, in fact, in excess of their contact resistances. In the process, the mobility in a GKTFET is not significantly degraded because the transmission gap dominates only for the off state and is kept just small enough in the on state to still allow saturation. GKTFET can reach a f_T of 33 GHz in a 1 μm channel device, and scale up to 350 GHz at 100 nm channel length assuming ideal single gate scaling. The f_{max} of GKTFET can reach 17 GHz in a device with a 1 μm channel and 53 GHz at 100 nm length, which is more than 10 times higher than that of GFETs at a comparable channel length. Higher f_{max} of 49 GHz(1 μm) and 158 GHz (100 nm) can be reached if the gate resistance of GKT-

FET can be significantly reduced by reducing the gate input resistance, such as with a T-Gate.

A gate dielectric with an equivalent SiO_2 thickness of 5 nm (EOT=5 nm) is considered in this work. In the on state, the three regions in the graphene channel are held as n-n⁻-n, so there is no angular filtering of electrons in the Fermi window between μ_S and μ_D for low V_{DS} . Filtering exists for portion of energy window [transmission gap shown in Fig. 3.6(B)] which comes into act for high V_{DS} . The small transmission gap exists due to slight differential doping (n-n⁻). This leads to current saturation in the on state. In the off state, the polarity of the central gate is moved to n-p-n where the gap increases substantially and the current drops.

It should be noted that the GKTFET proposed here is designed to establish proof-of-concept. In practice the geometry needs to be optimized keeping in mind the fabrication techniques, considering different approaches such as electrical gating [Fig. 3.5(B)] or contact-induced doping [48]/chemical doping [Fig. 3.5(C)] [75, 76] to create the side gated regions [blue n-doped regions in Fig. 3.5(A)]. According to our finite element electrostatic calculations using Ansoft Maxwell, the side gate in [Fig. 3.5(B)] at the drain end (back gate) introduces a large parasitic capacitance. This extra capacitance will possibly compromise the cut-off frequencies if it is AC connected to the ground directly. Extra care should be taken to get rid of the effect of this capacitance as discussed later. Compared with electrostatic side gate doping, the chemical doping shown in Fig. 3.5(C) does not suffer from these large gate capacitances. However chemically doped graphene has lower carrier mobility. In Fig. 3.5, a proposed device is shown with buried gates that was the basis for the calculations in this work; however, it is worth looking at alternate geometries, such as top gates [70, 77], with the associated design trade-offs.

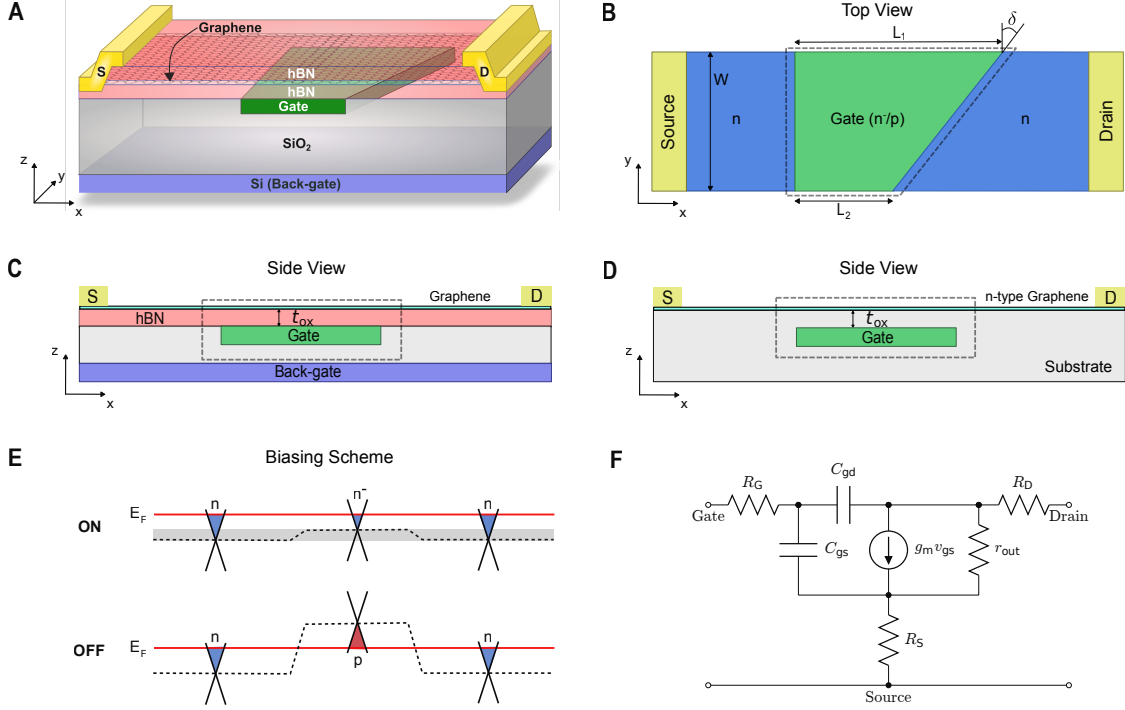


Figure 3.5: **Klein tunnel FET based on dual tilted graphene p-n junctions (GPNJ) for analog RF applications.** (A) 3D Schematic. Fabrication process is explained in Fig. 3.1. (B) Top view. Gate (local) controls the charge concentration in the central green region. In the off state (n-p-n), two back-to-back GPNJs are formed. The left GPNJ acts as a collimator and right GPNJ acts as a filter. In the on state (n-n⁻-n), GPNJ on the right is tilted by angle $\delta = 45^\circ$ with respect to the left one. The potential profile changes linearly across the junction (approximation) (see SI of Ref. [58]). In this work, the device has an average gate length of $(L_1 + L_2)/2 = 1 \mu\text{m}$ ($L_1 = 1.5 \mu\text{m}$, $L_2 = 0.5 \mu\text{m}$) and a width of $W = 1 \mu\text{m}$. Gate dielectric is equivalent to 5 nm SiO₂ (EOT = 5 nm). (C) Side view for electrostatic doping by gate. (D) Side view for chemical doping case where back-gate is not needed for controlling regions other than ones covered by a local gate. The essential part of the device is shown in dashed box, where the Klein tunneling effect near GPNJs dominates in (B, C, D). (E) Gate biasing scheme for on and off state. Gray region corresponds to the energy range of the transmission gap in the on state. (F) Equivalent small signal circuit. This figure is reproduced from Ref. [58].

In the proposed device, the total current I_{DS} across the GKTFET can be estimated by the Eq. (3.1). The resulting transconductance g_m can be written as

$$g_m = \frac{\partial I_{DS}}{\partial V_{GS}} \propto \int \frac{\partial (T_{av} M)}{\partial V_{GS}} [f(\mu_S) - f(\mu_D)] dE \quad (3.2)$$

$$\approx T_{av} M|_{\mu_S}^{\mu_D} \quad (3.3)$$

In the on state, the GKTFET has a small transmission gap around the Dirac point so that its mobility and g_m are expected to resemble a pristine GFET with the same dimensions. The presence of a transmission gap will, however, cause the current to saturate when the drain electrochemical potential μ_D moves towards the Dirac point and enters the transmission gap. In contrast, the g_m of ultra-clean GFETs has just a single point saturation precisely when μ_D hits the Dirac point since there is no gap in pristine graphene. This feature can be seen later in Fig. 3.7. The output resistance r_{out} can be estimated by

$$r_0 = \frac{\partial V_{DS}}{\partial I_{DS}} \propto \left(\int MT_{av} \frac{\partial f(\mu_D)}{\partial \mu} dE \right)^{-1}. \quad (3.4)$$

From Eq. (3.4), it can be seen that the output resistance depends on the modes inside the bandgap in quasi-ballistic limit. A perfect energy gap in principle leads to infinite output resistance because $MT_{av} = 0$ in the gap, while any states inside the gap due to imperfections (such as scattering, defects) will lead to a finite output resistance. In the proposed devices, the output resistance is limited primarily by the edge reflection and carrier scattering.

In calculations, GPNJ with perfect edges as well as rough edges - both the cases have been considered. Figure 3.6 shows the integrated transmission of (A) bulk graphene and (B) GKTFET, both for clean vs. dirty sample (charge puddles for bulk and edge roughness for GKTFETs). Pristine graphene has no band gap and its density of states $D(E) \propto |E|$ for a clean sample, while $D(E) \propto \sqrt{E^2 + 2\sigma^2/\pi}$ for a dirty sample [78], with $\sigma^2 \approx 2\hbar^2 v_F^2 n_{imp} + C$ describing the contribution of charge puddles in washing out the Dirac point through spatial averaging. A typical impurity density in a dirty sample with $n_{imp} = 1 \times 10^{12} \text{ cm}^{-2}$ from Ref. [78] is used. In contrast with GFETs, GKTFETs have a distinct transmission gap, as indicated in Fig. 3.6(B). Indeed, very few modes appear in the transmission gap. These gap states arise from edge reflection of electrons rejected by the second junction, a process that redirects them towards the drain. Ultimately these states contribute to the leakage current in

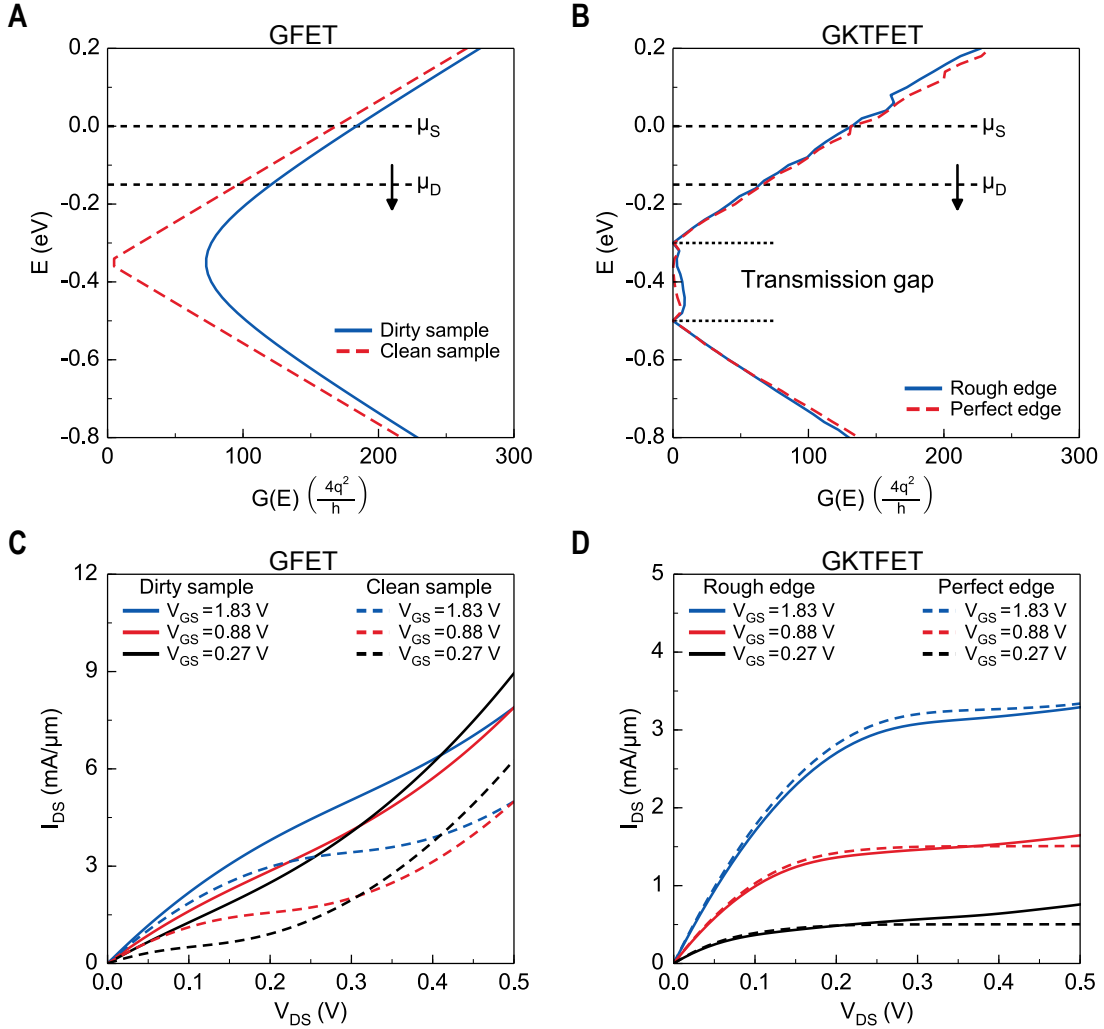


Figure 3.6: **Conductance and output characteristics.** (A) Energy resolved conductance for GFET (on-state). $G(E) \propto |E|$ corresponds to the Dirac cone-like band structure of clean sample (dash), and $G(E) \propto \sqrt{E^2 + 2\sigma^2/\pi}$ in dirty sample (solid) [78]. (B) Energy resolved conductance for GKTFET (on-state). A clear transmission gap can be observed unlike GFET in (A). $G(E)$ in the transmission gap is slightly non-zero due to the edge reflections even with the perfect edge. Adding edge roughness creates more states inside the transmission gap. (C) I_{DS} vs. V_{DS} for GFET. I_{DS} in dirty graphene sample (solid) is a linear function of V_{DS} whereas clean graphene sample (dash) shows one point saturation. (D) I_{DS} vs. V_{DS} for GKTFET. GKTFET shows obvious current saturation in both cases with (solid) and without (dash) edge roughness. With edge roughness, it shows slightly larger slope in the saturation region which in turn reduces r_{out} due to increment of states inside the transmission gap. Gate voltages are calculated considering quantum capacitance where 0.3 V, 0.2 V, and 0.1 V are dropped in channel respectively for gate voltages mentioned both in (C) and (D). This figure is reproduced from Ref. [58].

the off-state and lead to a finite r_{out} . Perfect edges in the GKTFET can reduce the leakage current by 20 to 40 times compared with GKTFET with rough edges in a 1 μm wide device. In calculation, the edge roughness introduces a random reflection angle with a variance of $\sigma = 18^\circ$.

3.3.2 Improvement in cut-off frequencies

Figure 3.6(C,D) shows the $I_{DS}-V_{DS}$ characteristics of GFETs and GKTFETs. In each case, the dashed lines are for clean samples while the solid lines include imperfections. It can be seen clearly that an ultraclean GFET shows $I_{DS} - V_{DS}$ with single-point saturation, while a GFET with a dirty sample shows a quasi-linear $I_{DS} - V_{DS}$ due to spatial averaging that washes out the Dirac point. In contrast, GKTFETs with both perfect and rough edges show a clear current saturation due to the presence of a pseudogap. The rough edges in GKTFETs lead to only a marginally smaller r_{out} because of the increase of MT_{av} in the transmission gap, which can be understood using Eq. (3.4).

Figure 3.7 shows the g_m and r_{out} of GFET and GKTFETs. The g_m of GFETs reach 0.5 to 1.5 $\text{mS}/\mu\text{m}$ (each gated region is 1 μm long in our simulation with linear transition length of 80 nm split length, d each), while the GKTFET turns out to have a slightly higher g_m of 1 to 2 $\text{mS}/\mu\text{m}$. The output characteristic however proves more dramatic than the transfer characteristic. The GFET shows a very low r_{out} of 0.1 $\text{k}\Omega\text{-}\mu\text{m}$ for dirty samples, and only around $r_{out} \sim 0.3 \text{ k}\Omega\text{-}\mu\text{m}$ for clean samples at saturation V_{DS} for all gate biases, dropping rapidly for other V_{DS} values. At zero temperature, $\frac{\partial f(\mu_2)}{\partial \mu_2} = \delta(E - \mu_2)$ in Eq. (3.4), $r_{out} = \infty$ as $MT_{av} = 0$ at the Dirac point.

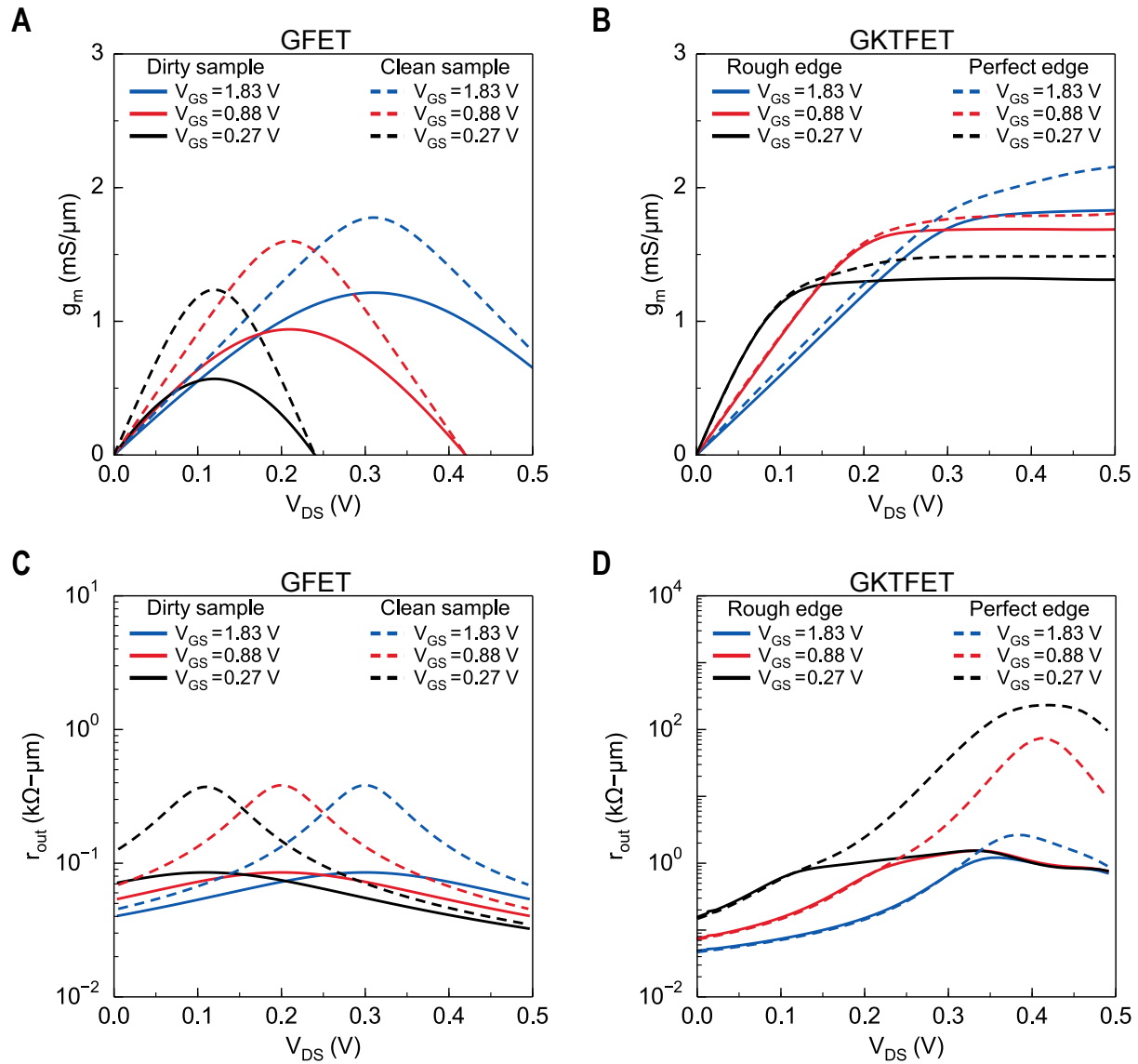


Figure 3.7: **Transconductance (g_m) and output resistance (r_{out}) for GFET and GKTFET.** (A) g_m vs. V_{DS} in GFET for dirty (solid) and clean (dash) sample where g_m is between 0.5 to 1.5 mS/ μm at saturation points. (B) g_m vs. V_{DS} in GKTFET with (solid) and without (dash) edge roughness where effect of edge roughness is not significant on g_m . (C) r_{out} vs. V_{DS} in GFET for dirty (solid) and clean (dash) sample where r_{out} is found to be around 0.1 k Ω - μm for dirty sample. (D) r_{out} vs. V_{DS} in GKTFET with (solid) and without (dash) edge roughness. Although r_{out} in GKTFET reduces from 10-100 k Ω - μm to about 1 k Ω - μm due to edge roughness, still in both cases, output resistances (r_{out}) are greater than the ones for GFET in (C) utilizing transmission gap. This figure is reproduced from Ref. [58].

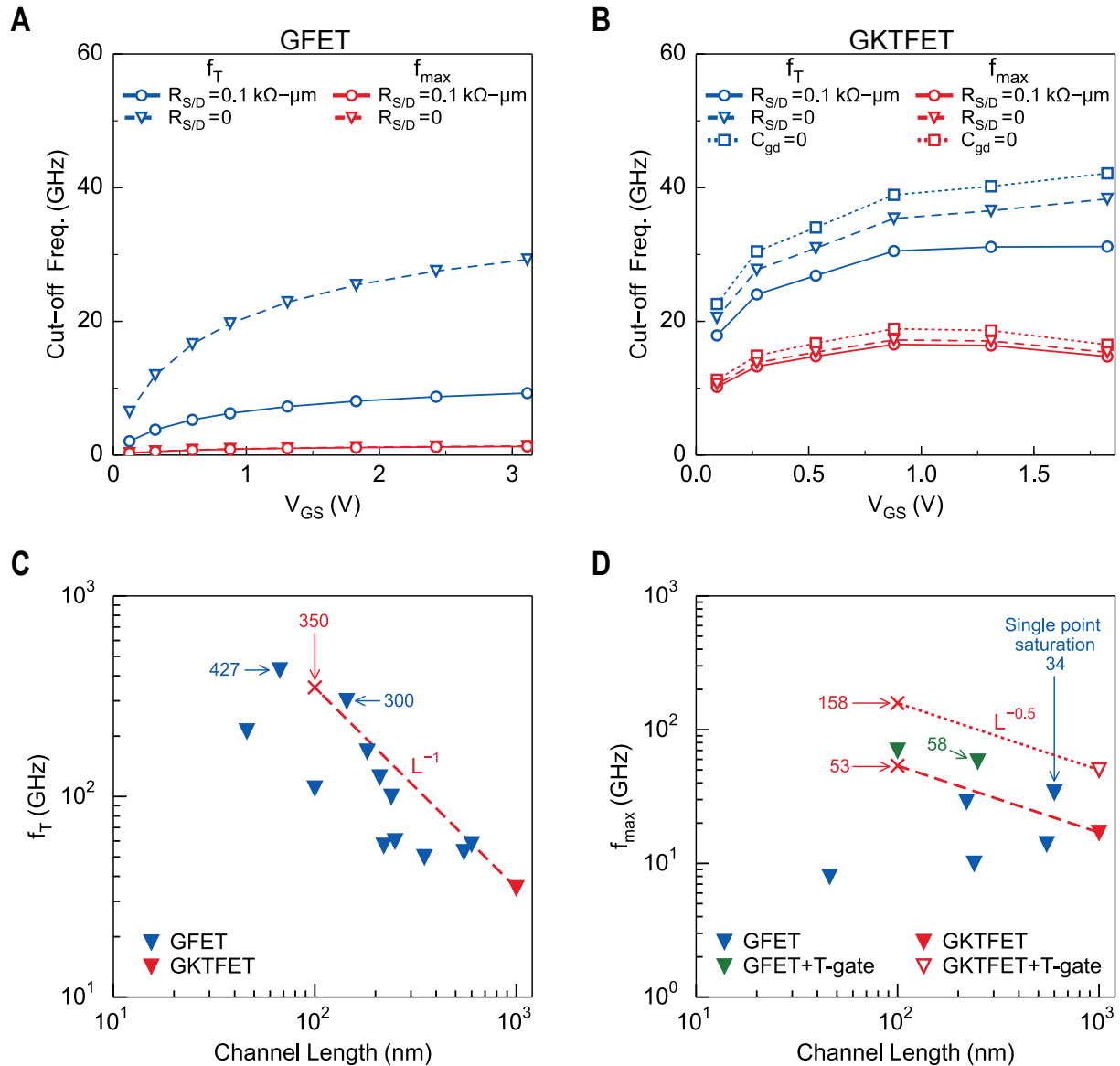


Figure 3.8: **Cut-off frequencies for GFET and GKTFET.** (A) f_T and f_{max} for GFET. The f_{max} of GFET is significantly smaller than f_T because of the small r_{out} . (B) f_T and f_{max} for GKTFET. f_T and f_{max} of GKTFET reach their maximum at the saturation region which range over 0.1 V to 0.3 V. Due to high output resistance, the max f_{max} in GKTFETs is about 50% of the maximum f_T . (C) f_T vs. channel length of GKTFET compared to reported GFETs. (D) f_{max} vs. channel length of GKTFET compared to reported GFETs. GFETs' data are from Ref. [69, 70, 77, 79–81]. Reported f_T s of GFETs are roughly inversely proportional to channel length, while the f_{max} s do not show this trend due to low output resistance. For ideally scaled GKTFET with 100 nm channel length, f_T is expected to reach 350 GHz (shown by red cross in (C)), which is comparable to the highest reported f_T s in GFETs (mentioned in the figure). The scaling of f_{max} of GKTFET follows $L^{-0.5}$ ideally. For a GKTFET with 100 nm channel, the f_{max} is expected to reach 53 GHz, and even high f_{max} =158 GHz can be expected if T-gate technique is used to reduce gate resistance (both shown by red cross in (D)). This figure is reproduced from Ref. [58].

At finite temperature r_{out} drops to a finite value because $\frac{\partial f(\mu_2)}{\partial \mu_2}$ has a non-vanishing spread of kT . Compared with GFETs, the GKTFET shows much higher r_{out} of 1 k Ω - μm even with edge roughness. GKTFET with perfect edges shows even higher r_{out} values that can reach 50 to 100 k Ω - μm . Furthermore, the saturation region corresponds to a V_{DS} in the range of 0.1 to 0.3 V instead of one point saturation.

To estimate the RF properties such as f_T and f_{max} of graphene-based RF devices, equivalent circuit for AC signals, shown in Fig. 3.5(E) has been considered. This structure assumes that the dominant capacitance is from the central gate that is swung between p and n polarities, while the side gated regions have lower capacitance (discussed later). For this equivalent circuit, the f_T and f_{max} can be estimated by [82].

$$f_T = \frac{g_m}{2\pi(C_{gs} + C_{gd})} \frac{1}{\sqrt{[1 + g_0(R_S + R_D)]^2 - (g_0 R_S)^2}} \quad (3.5)$$

with $g_0 = g_{ds} + g_m [C_{gd}/(C_{gs} + C_{gd})]$ and

$$f_{max} = \frac{f_T}{2\sqrt{\frac{R_G + R_S}{r_{ds}} + 2\pi f_T R_G C_{gd}}} \quad (3.6)$$

To illustrate the impact on f_T and f_{max} from improved g_m and r_{out} of GKTFET in comparison with GFETs, $C_{gs}=6.9$ pF/mm, $C_{gd}=0.7$ pF/mm and $R_G=1$ k Ω - μm for both transistors are used. However, it is worth re-emphasizing that the parameters are strongly dependent on the device geometry, for instance, the C_{gd} of the GKTFET in Fig. 3.5(B) is in fact negligible by finite element electrostatic calculation using Ansoft Maxwell. We accordingly choose an experimentally achievable ratio of $C_{gd}/C_{gs}=0.1$ [70] in the following calculations of f_T and f_{max} . It should be noted that calculations for f_T and f_{max} using small C_{gd} are only valid for saturation region.

Figure 3.8 shows the peak value of f_T and f_{max} of the GFET and GKTFET. The f_T reaches 9.3 to 29.3 GHz in GFETs with a channel length of $L_{channel}=1 \mu\text{m}$ (better contact resistances and smaller C_{gd} gives higher f_T). It is known that the f_T in pristine GFETs is inversely proportional to $L_{channel}$ [82]. Projecting accordingly, a channel length of 100 nm leads to an expected max $f_T=100$ to 300 GHz for a conventional GFET, which agrees with the published literature [69, 70, 77, 79–81]. The f_{max} of the GFET reaches only 1.3 GHz, i.e., 14% of f_T because of its small output resistance. Compared with the ideal case where $R_{S/D}=0$, the f_{max} of GFET with larger $R_{S/D}=0.1 \text{ k}\Omega\text{-}\mu\text{m}$ is reduced by 5%, while the peak f_T is reduced by 69%.

Compared with GFETs, the f_T of the GKTFET is larger due to a larger g_m arising from the opening of the transport gap and the resulting variation in density of states over the finite temperature window. More noticeably, the f_{max} and f_{max}/f_T ratio in GKTFET are significantly higher due to the current saturation arising from the engineered pseudogap. Figure 3.8(B,E) shows that the GKTFET with 1 μm channel length reaches a f_T of 31 GHz and f_{max} of 17 GHz. The f_{max} is 13 times larger than that of GFET. Furthermore, the contact resistance has a much weaker impact on f_T in GKTFET - in fact, 0.1 $\text{k}\Omega\text{-}\mu\text{m}$ R_S and R_D reduces the f_T by only $\sim 10\text{-}20\%$. The impact of R_S and R_D to f_T in both GFETs and GKTFET is determined by the factor $g_{ds}(R_S + R_D)$, $g_{ds} = 1/r_{out}$, as in the denominator of Eq. (3.5). The large output resistance r_{out} of GKTFET weakens the influence of R_S and R_D on the f_T . In Fig. 3.8, the f_T and f_{max} are shown in the limit of $C_{gd}=0$ by the dashed lines. It can be seen that the small C_{gd} leads to a 30% increase of the max f_T and 10% increase of max f_{max} .

While simulations are done for 1 μm , the ultimate advantage of the GKTFET for high-performance RF depends on its overall scalability, since the C_{gs} and R_G^{-1} are proportional to the channel length. In the GKTFET, the gate width and length are related, as a 45° tilted Junction is used. The f_T and f_{max} of GKTFETs and GFETs are shown in Fig. 3.8. Ideally, the f_T and f_{max} follow $f_T \propto C_{gs}^{-1} \propto L^{-1}$ and $f_{max} \propto C_{gs}^{-1} R_G^{-0.5} \propto L^{-0.5}$. The scaling of the

gate length of the GKTFET with from 1 μm to 100 nm is expected to increase the f_T and f_{max} by 10 and 3.2 times respectively, as indicated by the dashed lines. In contrast, the f_{max} of GFETs does not scale with channel length due to the low output resistance, as shown in Fig. 3.8. To estimate the f_T and f_{max} of 100 nm GKTFETs, following assumptions are made: the scaling down of the GKTFET does not change the electrostatics in the device (gate control is still dominant), the pseudogap can be effectively created by GPNJs in a scaled GKTFET, and device parameters such as C_{gs} and C_{gd} scale properly with channel length while maintaining the transition length (split length, d) across junctions in the range of 50-100 nm for better electron filtering resulting in transmission gap.

To summarize, a conceptual high-frequency RF device in Fig. 3.5 is proposed. This device operates by geometry engineering of a gate-tunable transport gap in pristine graphene, using the physics of Klein tunneling. In contrast to conventional GFETs which suffer from weak current saturation due to gaplessness, the engineering of a transmission gap allows the GKTFET to enjoy both high carrier lifetimes and current saturation. Our calculation of the GKTFET shows a significant improvement on f_{max} and a slightly higher f_T compared with GFETs. The device is expect to achieve an f_T of 33 GHz and a comparable f_{max} of 17 GHz in a device with 1 μm gate length, and ramp up to $f_T=350$ GHz and $f_{max}=53$ GHz as we shrink the gate to 100 nm. Higher f_{max} of 49 GHz for 1 μm channel and 158 GHz for 100 nm channel can be expected by reducing gate resistance with the technique of T-Gate. In addition, the cut-off frequencies of the GKTFET are seen to be much less sensitive to the contact resistance than GFETs, once again due to the significant increase in output resistance arising from current saturation.

3.4 Double source device

The strong angle dependence of Klein tunneling transmission has been proposed to realize a type of switching device based on DF optics (DFO) [25, 40, 55, 58, 60, 83]. Figure 3.9(A) shows a simple device scheme utilizing analogous electron optics. Here, a single-layer graphene channel is controlled by several local gates with predetermined shapes, dividing up electron-doped (n-type) and hole-doped (p-type) regions in the channel. The electrons leaving the source electrode pass through the first p-n junction orthogonal to the channel direction. This p-n junction filters out electrons with an oblique incident angle and collimates electron beams along the channel. The next p-n junction, placed at an angle ($\sim 45^\circ$), blocks the collimated electron beam due to the oblique incidence to the p-n junction and reflects it along a path orthogonal to the original. However, in this simplistic device design, the reflected beam hitting the rough physical edge of the device would diffusively scatter [Fig. 3.9(A)], leading ultimately to a leakage current into the drain electrode. On top of that, multiple bounces of electrons in between collimator and reflector junctions contribute to the leakage current. To circumvent these diffusive edge scattering and multiple bouncing events, one may design the collimator-reflector to minimize the channel edge scattering. For example, a sawtooth-shaped top gate, which can create double reflections sending the incoming DF beam back to source electrode, has been theoretically conceived based on DFO [24, 25]. The previous experimental study on such device architecture exhibited a signature of DFO behavior with the n-p⁺-n/n-p-n on/off ratio of 1.3 [62]. However, the definition and value of the on-off ratio can largely depend on the device operation scheme and other device specifics. Therefore, it can be challenging to use the on-off ratio as a universal and accurate metrics for quantifying the DFO contribution. The necessity for establishing device-independent methodology to measure the DFO contribution motivates us to develop a series of experimental designs that allow two independent methods of accurately characterizing DFO contribution. This section is reproduced from Ref. [59] coauthored with K. Wang, L. Wang, K. M. M. Habib, T. Taniguchi, K. Watanabe, J. Hone, A. W. Ghosh, G. Lee, and P. Kim.

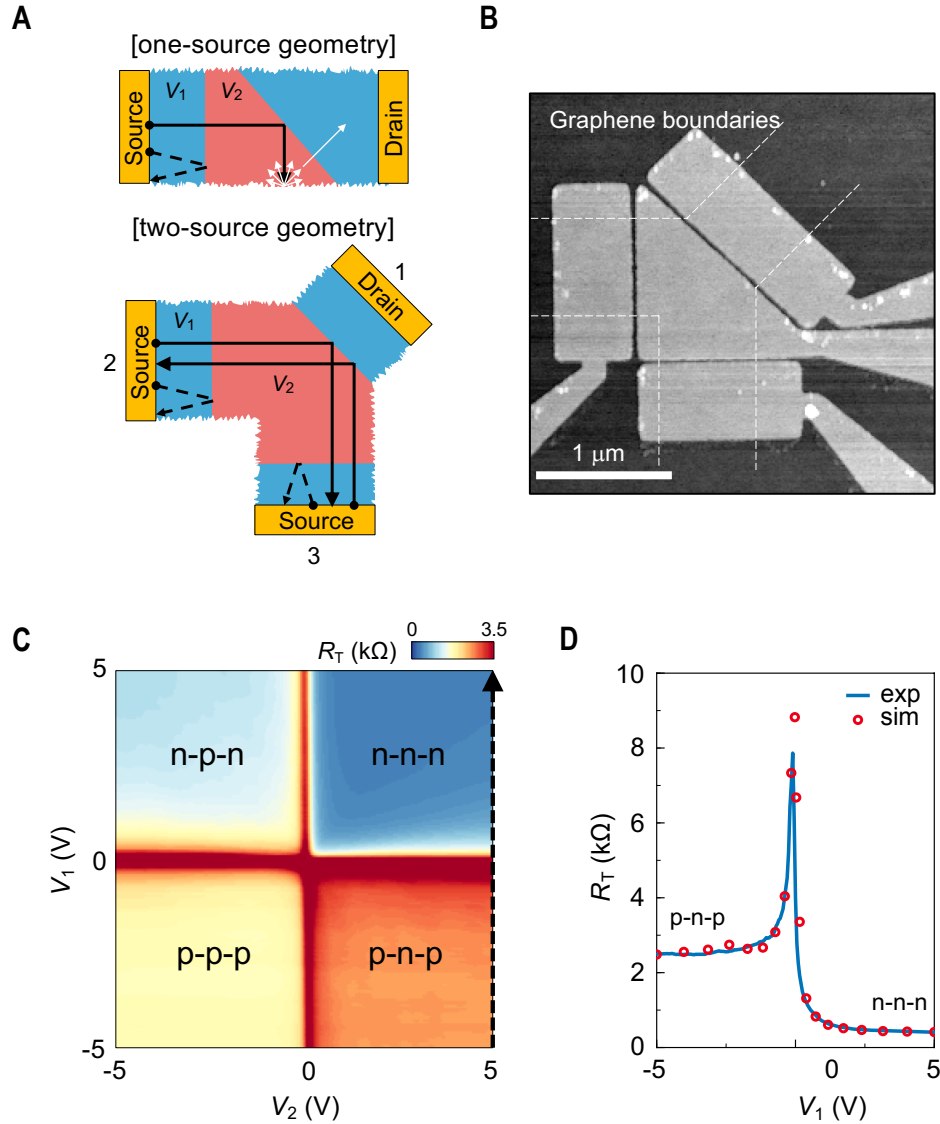


Figure 3.9: **Graphene quantum switch.** (A) Schematics of the device in the off mode. Central green area (gate voltage, V_1) and the blue areas (V_2) are doped in different polarity ($V_1, V_2 < 0$). The collimated electron beams through vertical and horizontal junctions are reflected toward the device edge in one-source geometry or back to the source in two-source geometry. (B) Atomic force microscope image of bottom gates was taken before transferring a stack of h-BN/graphene/h-BN. Overlaid broken lines guide the boundaries of graphene. (C) Colour-coded total resistance (R_T) as a function of V_1 and V_2 . (D) Slide cut of the resistance shows the on-off ratio of 6 at fixed $V_2 = 5$ V. Semi-classical ray tracing simulation matches experimental data especially for higher $|V_1|$ (on or off state). To fit the off state (p-n-p), we use edge roughness parameter $\sigma_e = 15^\circ$ (standard deviation of Gaussian distribution of added random angles to specular edge reflections). Reproduced from Ref. [59] with permission.

The dual source device design reduces diffusive scattering at edges and multiple bounces that are otherwise responsible for high off-state current leakage. Figure 3.9(B) shows a

schematic diagram of the proposed device and the overall operational procedure. When the central gate region (controlled by gate V_2) turns into the opposite carrier polarities of source and drain regions (controlled by gate V_1), carriers injected from each source will either reflect back to the same source (oblique incident angle) or travel ballistically to the other source contact (perpendicular incident angle). This collimation-reflection results in suppressed conduction between the source and the drain, and the device is in “off” state. When V_1 and V_2 are at the same polarity, the carriers flow ballistically to the drain, and the device is in “on” state. This device operation scheme has an advantage compared with the aforementioned single-source collimator-reflector scheme [Fig. 3.9(A)] or a sawtooth-shaped gate structure [24, 25, 62], as there is no significant channel edge contribution and only one reflection can be used for the off operation. Even with a nonideal reflector, we thus expect considerably enhanced DFO of the switch.

Figure 3.9(B) shows electron microscope image of the local gates used for the dual-source device before the integration of graphene channel with two-source and one-drain electrodes in place. Switching operation of our device can be demonstrated by measuring two terminal resistance R_T between the drain electrode (1) and source electrodes (2 and 3). A common bias voltage V_D is applied to the source electrodes while the drain electrode is grounded. Two gate regions, collimation gates and the central gate, are controlled by applied gate voltages V_1 and V_2 , respectively. Figure 3.9(C) shows the measured R_T as a function of V_1 and V_2 . The resistance map in (V_1, V_2) plane can be divided into four quadrants separated by the peak region of $R_T \sim 8 \text{ k}\Omega$, corresponding to the charge neutral Dirac point, $V_1, V_2 \sim 0$. These four distinctive quadrants represent the source collimation/central gate/drain collimation regions in the n-n-n, n-p-n, p-p-p, and p-n-p regimes, respectively. We note that the n-n-n regime has the lowest resistance R_T of $\sim 500 \Omega$, while the p-p-p regime exhibits considerably larger resistance of $\sim 1.5 \text{ k}\Omega$. In an ideal device, we expect a p/n symmetry in the device gate operation due to the particle-hole symmetry in the graphene band structure. However,

the graphene channel can exhibit asymmetry in contact resistance due to the metal-induced contact doping [84], which prefers n channel to have lower contact resistance in our devices. The best device performance, therefore, is shown along the p-n-p to n-n-n regime, because there arise additional angled p-n junctions between contacts and graphene in p-n-p (off) regime. Figure 3.9(D) shows a slice cut of R_T along V_1 at a fixed $V_2 = 5$ V, crossing the p-n-p (off) to n-n-n (on) regimes. We choose this particular gate operation scheme for a pragmatic demonstration of a large on-off ratio achieved in our device, although the on-off ratio defined in this way contains not only the DFO contribution but also the contact and p-n junction resistance as we will below.

To benchmark our experimental data, we perform semi-classical ray tracing simulation [32] utilizing a billiard model [46, 47, 85] coupled with analytical Klein tunnelling equations at junctions (simulation details in Appendix A). For Fig. 3.9(D), channel resistance (R_{Ch}) is calculated from simulation and R_C (contact resistance) is calculated from Fig. 3.9(C) diagonal elements ($V_1 = V_2$) (as for every V_1 contact resistance is changing). Then total resistance, $R_T = 2R_C + R_{Ch}$. To fit the off state (p-n-p), we include a random scattering angle around a specular trajectory (following a Gaussian distribution with standard deviation $\sigma_e = 15^\circ$) at the edges. Our analysis shows that on-off ratio degrades with increasing e as it creates more and more states inside the transport gap. We emphasize that the switching operation based on our DFO does not require a *bandgap* in the channel material, since the device operation relies on Klein tunneling of DFs, which in turn keeps the high mobility of graphene intact in the on state and uses a gate-tunable transport gap for off state.

3.5 Conclusion

In this chapter, we show how electron optics can be utilized to realize an electronic switching device. As we are using the angular resolution of electrons, any geometrical non-idealities (i.e.

edge roughness, junction roughness) degrades the device performance. Considering limited performance, we have shown how pseudo transport gap can be utilized for saturating output characteristics while keeping the mobility high which opens the door for the [GKTFET](#) for RF applications. In the next chapter, we will show the effects of the aforementioned non-idealities in details.

Chapter 4

Metrology and optimization: benchmarking non-idealities

In recent years, there has been a number of proposals [24–26, 33, 55, 58, 60, 62] of graphene devices that rely on transport gaps [56] instead of bandgaps exploiting the unique properties of Dirac cone systems at p-n junctions. Some of these initial device ideas relied on negative refractive index and Veselago lensing resulting from the conservation of transverse quasi-momentum at the junction [14, 49]. However, the switching properties of such waveguide-like devices are likely to be very modest, even for perfect geometries in scaled devices [33, 86], due to the need for sharp injectors and detectors. Angle dependent transmission of Dirac fermions [35] in graphene p-n junction (GPNJ), on the other hand, potentially offers more robust solutions with macroscopic gates and contacts. Part of this chapter is reproduced from Ref. [87], with the permission of AIP Publishing coauthored with K. M. M. Habib, K. Wang, G. Lee, P. Kim, and A. W. Ghosh; and reprinted with permission from Ref. [88] coauthored with X. Zhou, A. Kerelsky, D. Wang, K. M. M. Habib, R. N. Sajjad, P. Agnihotri, J. U. Lee, A. W. Ghosh, F. M. Ross, and A. N. Pasupathy. Copyright 2019 American Chemical Society.

A perfect match of the pseudospin structure at the interface causes a GPNJ to become

completely transparent to normally incident electrons (Klein tunneling [17, 38]) while it becomes more opaque as the incident angle increases. Ramping up the voltage barrier across the junction collimates the electrons by narrowing the distribution of their transmission angles. This collimation can be further enhanced with a smoothly varying barrier of finite width spanning a split gated junction, which imposes an added Gaussian distribution around normal incidence [35]. Subsequently, putting a second junction at a relative angle (δ) rejects most of the electrons as long as δ exceeds the maximum critical angle (θ_C) of the filtered and collimated electrons [60]. This two junction device, analogous to a polarizer/analyzer in optics, is broadly referred to as Graphene Klein Tunnel (GKT) transistor (Fig. 4.1).

Angle dependent transmission is key to getting a tunable resistance in a GKT, achieved by controlling the gate voltage. Sajjad *et al.* have shown that such a GKT transistor would show a clean transport gap in the off state leading to a nearly ideal transfer characteristic consisting of low off current, high on-off ratio ($I_{on}/I_{off}=R_{off}/R_{on}=10^4$) and steep subthreshold swing (SS) lower than the Boltzmann limit of 60 mV/decade [55, 60]. Beyond a desirable gate transfer characteristic, the GKT transistor was also shown to have an excellent output characteristic with a high saturating on current retaining a high mobility in the on state [58, 61]. In these calculations [55, 60, 61] however, non-idealities such as momentum scattering, in particular at the edges and junctions were not considered. In this chapter we will discuss effects of edge roughness (section 4.1) and junction roughness (section 4.2) on device performance as well as propose a method for characterizing edge roughness from tranverse magnetic focusing experiment (section 4.3).

4.1 Edge roughness

Edge scattering of rejected electrons or holes at the second junction compromises the off state leakage current, as the charge carriers keep bouncing around until some of them find themselves in the narrow transmission lobe of the second junction. Indeed, considering edges and secondary bounces, a more realistic calculation using both quantum and semi-classical models showed that the on-off ratio degrades to $\sim 10^2$ for perfect edges at widths of $\sim 1 \mu\text{m}$ [24, 25, 57]. Based on the initial two junction device idea [24, 60], Morikawa *et al.* [62] and Wang *et al.* [59] reported experimental on-off ratios of 1.3 and 6-13 respectively, but these on-off ratios are low compared to predictions. Multiple experiments have now confirmed the basic physics of angle dependent transmission at a single tilted junction [18, 32], and impact of Klein tunneling in a graphene quantum dot [89], yet no rigorous study has been found explaining the poor on-off ratio in double junction devices in general.

In this section, we explain the existing discrepancy between simulations (on-off ratio $\sim 10^2$) [24, 25, 57] and experiments (on-off ratio ~ 10) [59] of GKT devices. We find that in addition to the electrons suffering multiple bounces around the wedge shaped region between junctions, non-specular (diffusive) scattering by rough edges, shown by white arrow in Fig. 4.1B, plays an important role in degrading the on-off ratio by transforming the transport gap to a pseudogap with a non-zero floor (Fig. 4.2A). We study several variations of graphene p-n junction based devices. Starting from a basic building block, a single p-n junction, we extend to complex structures consisting of multiple junctions. Specifically, we consider a split-gated single junction (SJ), parallel split-gated dual junctions (DJ), two split-gated dual junctions in an angled trapezoidal geometry (DJT) [60], a triangular gated (TG) prism geometry (basic building block of saw-tooth geometry [24, 25]), a dual-source (DS) device [59], and finally a structure with two drains rotated at 90° relative to two sources, generating an effective EdgeLess device (EL). In Fig. 4.3, all the structures are shown with their off state electron paths marked in red. Our comparative study shows advantages and disadvantages of one struc-

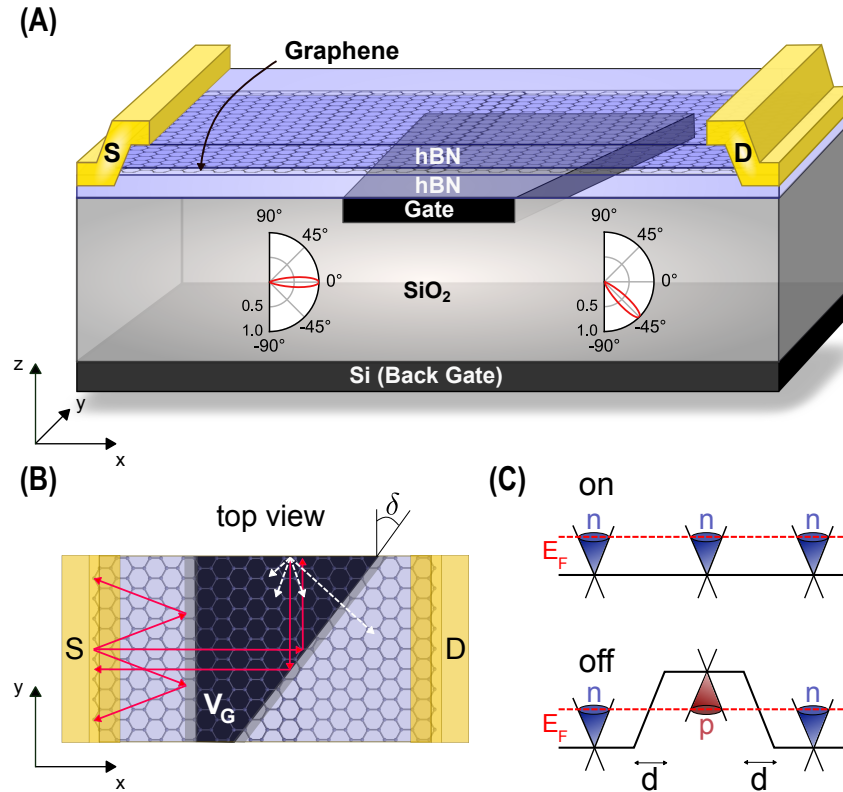


Figure 4.1: **Graphene Klein Tunnel transistor using electron optics.** (A) 3D schematic. The polar plots in inset show angle dependent transmission probability of electrons at each junction in the off state (n-p-n). First junction only permits normal incident electrons. Second junction, tilted at $|\delta| = 45^\circ$, is allowing only electrons close to -45° , thereby filtering most of the electrons. (B) Top view. Off state electron paths are shown in red color and white color path shows non-specular reflection from rough edge resulting in leakage in off state. (C) Potential profile in on (n-n-n) and off (n-p-n) state. Here, d is the junction width. Reproduced from Ref. [87], with the permission of AIP Publishing.

ture over another, providing a guideline for designing electron optics inspired devices in future.

A finite transport gap generated by the angular filtering of electrons differentiates GKT devices from conventional graphene Field Effect Transistors (gFET). In Fig. 4.2(A), we see a transport gap arising from the double junction structure (DJT). Here, conductance unit is $4q^2/h$ where $q = 1.6 \times 10^{-19}$ C is the charge of an electron and h is the Planck's constant. We also show the case for abrupt p-n junction ($d = 0$ nm) where filtering is not that robust. A smooth p-n junction ($d = 70$ nm) performs better than an abrupt one due to added Gaussian filtering due to angle-dependent tunneling. In presence of edge roughness, the transport

gap turns into a gap with a nonzero floor and increases the overall off state conductance [Fig. 4.2(A)]. We see dips at $E = \pm 0.3$ eV due to Dirac points. As shown in Fig. 4.2(B), edge roughness degrades the off state performance ($V_G \sim -10$ V) for any given δ . We also show that $\delta = 45^\circ$ gives the lowest off current even in the presence of edge roughness, as suggested earlier [40]. Here, local gate dielectric (hexagonal boron nitride, hBN) thickness is 32 nm and device width (W) is 1 μm (also for all other cases unless otherwise stated). To discuss the effect of edge roughness in detail as well as the dependence on device geometry, we analyze a variety of structures in this paper (Fig. 4.3).

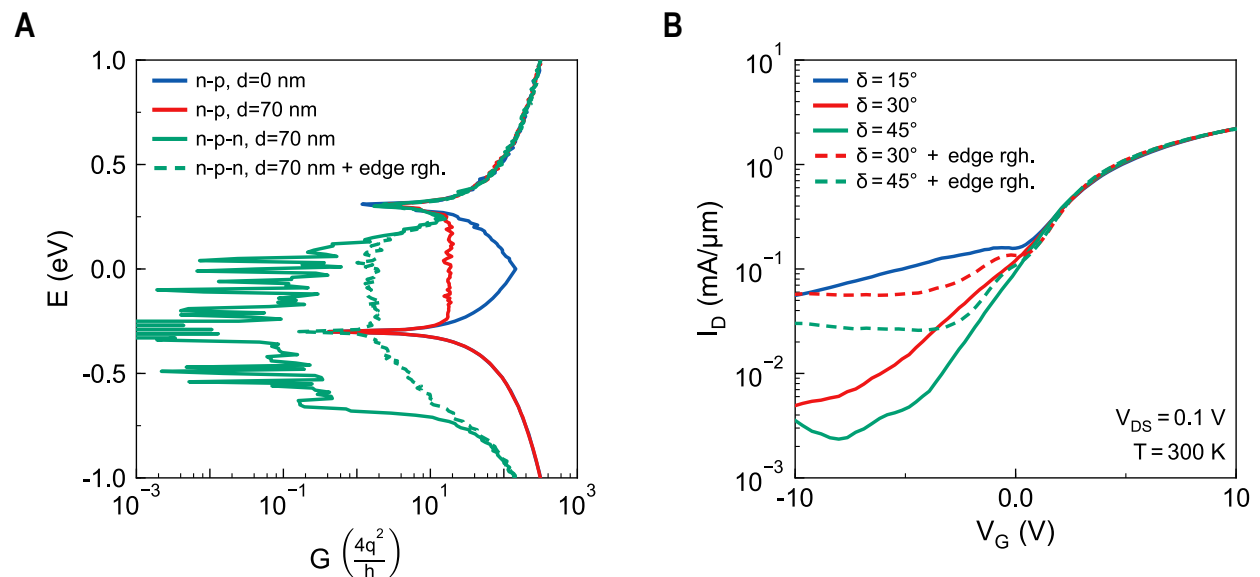


Figure 4.2: **DJT Device characteristics.** (A) Conductance of p-n junction devices in off state (n-p or n-p-n). Transport gap between -0.67 eV and +0.3 eV arises due to electron filtering in ideal n-p-n device with $|\delta|=45^\circ$. Adding edge roughness increases the floor value of the gap shown by dashed line. For comparison we also show single n-p junction conductance (abrupt and smooth with junction width $d = 70$ nm). (B) Transfer characteristics from semiclassical ray tracing simulation with source-drain voltage $V_{DS}=0.1$ V. Reproduced from Ref. [87], with the permission of AIP Publishing.

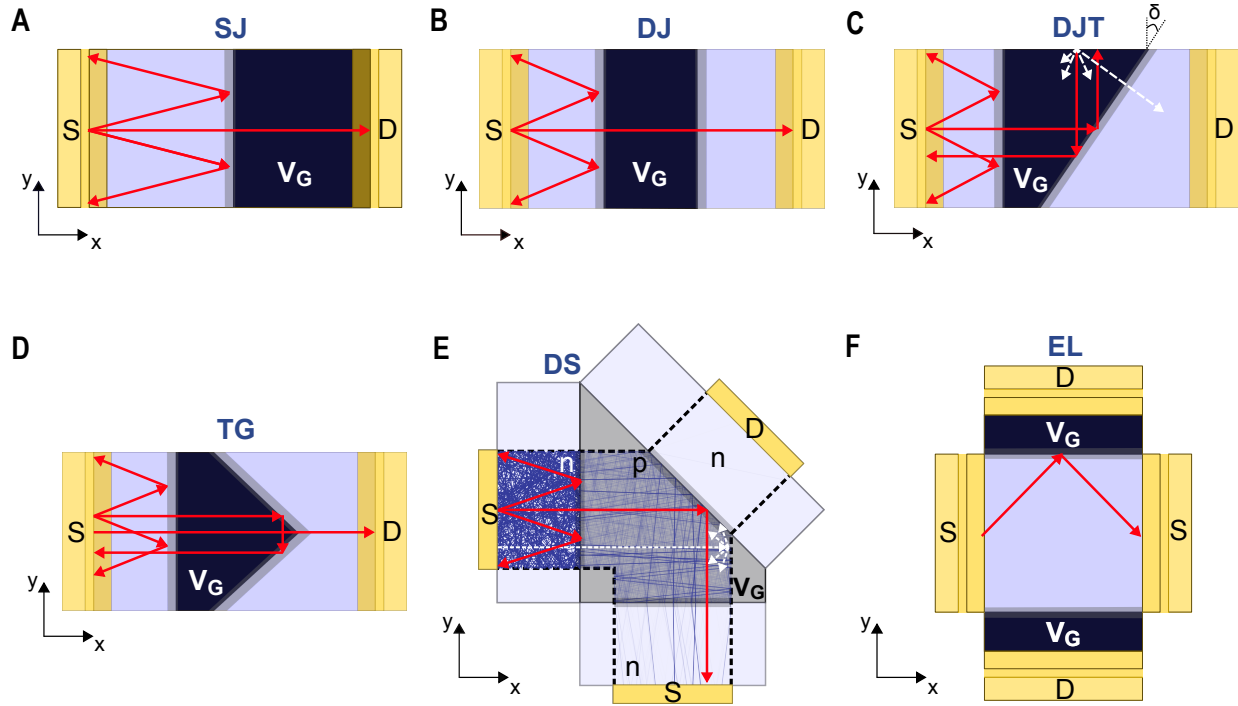


Figure 4.3: **Device family schematic.** (A) SJ device. (B) DJ device. Both the junctions are parallel to each other. (C) DJT device with $\delta=45^\circ$. White arrows show spreading of electrons when they hit the edge in case of non-specular reflections and leakage path through the second junction (small incidence angle). (D) TG device. Only gate is used to reflect back the electrons making the device less susceptible to edge roughness, although tip of the triangle suffers from leakage path. (E) DS device [59] with ray tracing simulation paths. Electrons are reflected back to the other source, thus it is free from multiple bounce issue of electrons. (F) EL device. The junction is rotated 90° with respect to source, thus most of the electrons are reflected back in off state. Moreover, this device does not have an edge so edge roughness does not play any role in this device's performance. In all the cases, red arrows show electrons path in off state. Reproduced from Ref. [87], with the permission of AIP Publishing.

4.1.1 Simulation method

In this study, we adopt semiclassical ray tracing approach [32, 57] based on a billiard model [46, 47, 85] that has been benchmarked against experiments [32]. A charge carrier hitting a perfect edge reflects back with an angle equal to the incident angle (specular reflection). In presence of edge roughness, a Gaussian distributed random angle of reflection with standard deviation σ_e (higher σ_e denoting rougher edges) is added. The transmission probability (T) for each electron across a junction is calculated analytically, using a general-

ized version [60] (see supplementary material, Eq. (S1)) of the well-known equation [35] for symmetric junction, $T \sim e^{-\pi k_F \frac{d}{2} \sin^2 \theta}$. Here, k_F is the magnitude of the Fermi wave vector on each side for a symmetric p-n junction, d is the junction width, and θ is the incident angle at the junction. We calculate channel resistance R_{Ch} for low-bias and total resistance using $R_T = R_{Ch} + 2R_C$, where R_C is the contact resistance between graphene and source/drain electrodes (see supplementary material for details). To explain experimental data [59], contact resistance $R_C \sim 100 \Omega\text{-}\mu\text{m}$ and non-specular edge scattering are included in our semiclassical simulation model. The junction width d is 70 nm and temperature is 50 K unless otherwise mentioned. The main advantage of ray tracing over the Non-equilibrium Greens function (NEGF) formalism is its computational practicality.

4.1.2 Results and Discussions

We now discuss the impact of gate geometry on various flavors of ballistic, perfect edge GKT transistors, as quantified by their low-bias resistances and on-off ratios. Figure 4.4(A) shows the results of the low-bias on and off state resistances for each geometry. The back gate voltage is kept fixed to $V_{BG}=100$ V (corresponding to charge density $n_1=6.63 \times 10^{12} \text{ cm}^{-2}$ for SiO_2 thickness of 300 nm in addition to 32 nm hBN) for all these devices while we sweep the local gate V_G to vary the corresponding charge density of middle gate region (n_2) from negative (p-type) to positive (n-type), giving us the off and on states respectively. Our first structure, an SJ device [Fig. 4.3(A)] filters out carriers at angles other than normal incidence, exhibiting Klein tunneling. Adding another junction aligned to the first one [Fig. 4.3(B)B, DJ] does not help in increasing on-off ratio significantly, but instead adds another comparable resistance along the path. With a tilted second junction [Fig. 4.3(C), DJT with $\delta = 45^\circ$], we can achieve orders of magnitude larger off state resistance for ballistic flow. Next the TG device [Fig. 4.3(D)] uses the second junction to reflect back strongly collimated carriers towards the source away from the edges. However, it has a poorer performance in the off

state than DJT structure because it allows electrons to Klein tunnel through its vertex on the first try. The DS device [59] [Fig. 4.3(E)] has an overall L-shape, so that each segment of the split source recaptures carriers injected from the other segment and rejected by the tilted junction, without letting them bounce again at the edges. As a result, its off state performance is superior to the DJT device. Finally, the EL [Fig. 4.3(F)] device capitalizes on a structure that is free from edge effects. In the EL structure shown, electrons enter along one axis from both sources, while the drains are along a perpendicular axis with the gate induced p-n junctions sitting in between. Such EL structures reduce the off current because most electrons incident at the junction are at large angles. Compared to an ideal DJT device, the off state resistance is still low as it uses only one junction. Moreover, the on state current of the EL, determining its device speed, is compromised by the right angle separating source and drain - moving the drain away from the natural ‘line of sight’ of the injected source electrons. The low on current degrades the overall on-off ratio of the EL device.

Edge roughness tends to decrease the on-off ratio of these devices by diffusive scattering of the reflected electrons providing a leakage path to the drain as shown in Fig. 4.3(C, E) by the white dashed lines. Thus the transport gap turns into a pseudo gap with a finite floor (Fig. 4.4B) with increasing edge roughness. For ideal edges we see a transport gap spanning -0.67 eV to $+0.3$ eV. With increasing edge roughness, the floor value of the gap also increases (other than at $E = -0.3$ eV due to a clear Dirac point, which in turn could be washed out by impurity scattering and puddles [78]), thus increasing off state conductance and decreasing resistance. In Fig. 4.4C, we show the evolution of resistance characteristics of the DS device with increasing edge roughness. Here we use device parameters $d = 60$ nm, width=800 nm, and voltages $V_G = -6$ V to 6 V, $V_{BG} = 60$ V, emulating a local gate voltage of 6 V, as in the experiment [59]. In Ref. [59], all the regions (n-n-n/n-p-n) are controlled by local gates whereas in our simulation only the middle region is controlled by a local gate (V_G) while other regions are controlled by back gate (V_{BG}). We match the on state ($V_G =$

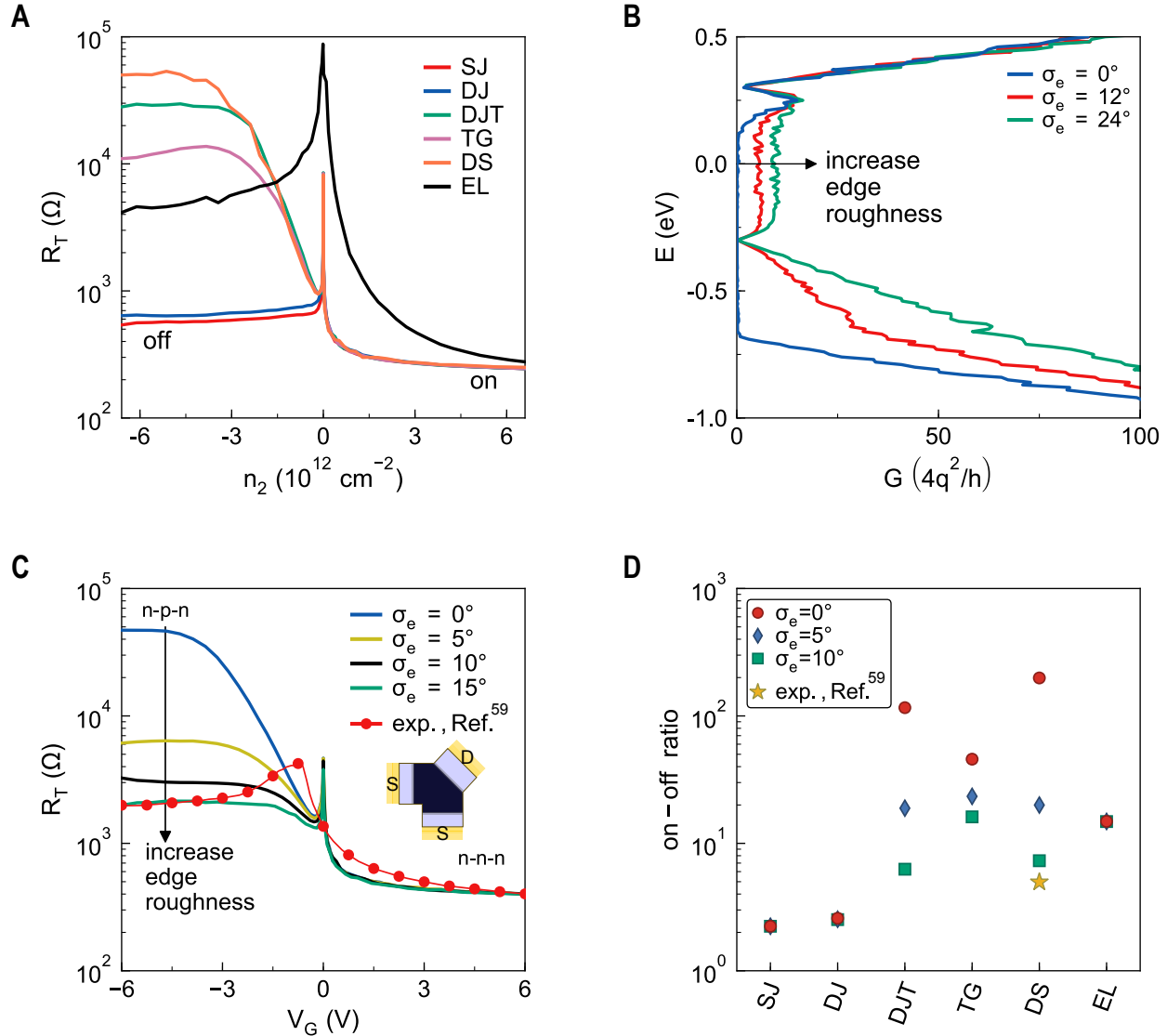


Figure 4.4: **Low-bias resistance characteristics and effect of edge roughness.** (A) Calculated total resistance for different geometries. (B) With increasing edge roughness in a DS device, transport gap turns in to a pseudo gap having higher nonzero floor value due to additional leakage path. (C) Low-bias resistance characteristics of DS device (experiment [59] vs. simulation). Off state (n-p-n) degrades significantly with increasing edge roughness. Contact resistance ($117 \Omega\text{-}\mu\text{m}$) and edge roughness parameter ($\sigma_e=15^\circ$) are adjusted to match experimental values of on and off state resistance respectively. (D) On-off ratio for different gate geometries with various edge roughness. For reference, experimental on-off ratio [59] from (C) is also shown, although device width and doping conditions are not same as simulation. Reproduced from Ref. [87], with the permission of AIP Publishing.

6 V) result by fitting a contact resistance ($R_C = 117 \Omega\text{-}\mu\text{m}$) and off state ($V_G = -6$ V) resistance by fitting edge roughness parameter $\sigma_e=15^\circ$. We see a mismatch between our simula-

tion and experiment at $V_G \sim 0$ V due to charge puddles that average out the Dirac points [78].

Figure 4.4D shows the evolution of the on-off ratio for all the device geometries in presence of edge roughness. We clearly see orders of magnitude enhancement of on-off ratio in DJT compared to SJ and DJ, but in the presence of edge roughness the on-off ratio degrades significantly. In contrast, although the TG device starts with a lower on-off ratio due to Klein tunneling at the vertex, it shows robustness against edge roughness as it directs the collimated electrons away from the edges (Fig. 4.3D). The DS device is supposed to perform better even in presence of edge roughness. However, as the device geometry [59] is not optimized considering edge roughness (Fig. 4.3E, second junction position, electrons shown in white arrow hits edge), the on-off ratio degrades significantly. Improved device geometry (DS_{imp}) shows at least 2 times better on-off ratio in presence of edge roughness (see supplementary material, Fig. S2). In Fig. 4.4D, we also show the experimental on-off ratio [59] from Fig. 4.4C, notably with different device width and doping than for simulation. Finally, the EL device which starts with an even lower on-off ratio than the TG device, but the on-off ratio remains constant with increasing edge roughness as the electrons do not hit any edge before getting filtered out.

In this work, we focus on low-bias characteristics to explain the discrepancy between experiments and simulations (even at low temperature) by adding edge roughness scattering and quantifying its effect on pseudo transport gap in off state. Graphene remains ballistic over length scales in excess of $1 \mu\text{m}$ even at room temperature [5]. For any scattering process in the off state, what matters is the length scale of the local (middle) gated region ($<1 \mu\text{m}$ for $W=1 \mu\text{m}$) as the first junction will filter electrons with random incident angles. Other than edge roughness scattering, phonon scattering at high-bias (V_{DS}) and high temperature is supposed to be suppressed due to high remote optical phonon (OP) energy (102 meV) [90] in graphene on hBN, and limiting self-heating process [91] due to high thermal conductivity of hBN [92]. On top of that, the transport gap of ~ 600 meV ($\gg 102$ meV, remote OP energy at

room temperature) helps to reduce the effect of phonon scattering. Moreover, the measured on-off ratio of the DS device is relatively insensitive to temperature over a large range (1.8 K to 230 K) as well as to a wide range of bias current [59], indicating insignificant presence of phonon scattering in the device. Also, electron-electron interactions are expected to be screened out due to the presence of the gate, and lower impurity scattering [12] is expected for hBN as a substrate. Therefore, our assumption of momentum scattering due to edge roughness being the dominant scattering mechanism for leakage currents in the off state, leading to low on-off ratio, is justified within the scope of this study.

4.1.3 Improving device performance

As a transistor, a ballistic GKT greatly outperforms wave-guided structures based on the Veselago effect. However, even a GKT faces challenges arising from the presence of edges - in particular rough ones, together with contact resistance and finite doping of graphene by metal contacts. A 1 μm wide structure with perfect edges is predicted to have a gate transfer characteristic with an on-off ratio $\sim 10^2$, but current technology limits the edge smoothness and degrades the on-off ratio to ~ 10 , demonstrated experimentally [59]. With decreasing on-off ratio, another important parameter for digital logic tied to that, SS increases well beyond 60 mV/decade (lowest 121 mV/decade and highest 253 mV/decade for effective oxide thickness of 1 nm at room temperature with edge roughness). So comparison of SS owing to low power applications for different structures is out of scope for this study unless graphene-edge roughness limitation is resolved. Such a low on-off ratio and high SS are not suitable for digital logic.

The output characteristic, however, bears more promise. At high drain bias (V_{DS}), a small transport gap ($n^+ - n - n^+$, on state) at energies far from the equilibrium Fermi level is predicted to produce a strongly saturating $I_D - V_D$ that is robust against edge roughness [58]. Even cases with an on-off ratio ~ 10 can result in an order of magnitude increment in r_{out}

(output resistance) without hurting the mobility. Devices like this with high mobility and output resistance can be quite useful for analog RF applications, delivering a high f_T (unity current gain cutoff frequency) and f_{max} (unity power gain cutoff frequency) [58]. To improve device performance, a superlattice potential may be incorporated into the device to create an anisotropic band structure and create a much more aggressive collimation of electrons [93, 94]. Further improvements may be possible with abrupt junctions if doping can be improved in the first region, so that the reflected electrons at the second junction are no longer stopped by an abrupt first junction on their way to the source (recall that total internal reflection only works one way like a diode, from a denser to a rarer medium). A major factor in determining the overall performance of all these structures is edge roughness, included here as a phenomenological parameter, the standard deviation σ_e of a Gaussian angular smear. The relationship between σ_e and physical roughness parameters, as well as decay rates extracted from magnetoconductance measurements is out of scope of this study and will be reported elsewhere.

4.1.4 Conclusion

In summary, the performance challenges of a GKT transistor are outlined in this subsection. Although junction line-edge roughness [88] and other scattering events are expected to play a role, we focused here on edge roughness that is expected to be the most deleterious to the on-off ratio through momentum redirection. We quantified the role of graphene-edge roughness and attempted to design around it, such as the EL device. We analyzed a family of devices and find that TG, DS_{imp} and EL device are less susceptible to edge roughness. We further showed that an angle of 45° between collimator and reflector gives the best performance even in the presence of edge roughness. Our analysis shows that even with geometry optimization the on-off ratio may not be enough for scaled digital switching, but may still offer advantages for high frequency RF analog applications [58].

4.2 Junction roughness

In our previous simulations, we considered perfect junction. Junction roughness may affect the device performance like edge roughness does. Having characterized the parameters at the atomic scale in real graphene p-n junctions in Ref. [88] (see for details of Scanning Tunneling Microscope characterization of graphene p-n junction), we now assess the impact of these parameters on two key electron-optical functions: collimation and Veselago lensing. We do this through model simulations using the [Non-Equilibrium Green's Function \(NEGF\)](#) formalism. The analysis is helped by the fact that the width of the junction (40-100 nm) is much larger than the length scale of the lateral roughness (a few nm) in the junction. We can therefore independently model the effect of lateral roughness and of the doping profile in our junctions. Veselago lensing happens for a sharp p-n junction where $k_F d \ll 1$, while carrier collimation happens for $k_F d \gg 1$. For our graphite gate device with a symmetric profile (a single k_F value for both electron and hole doped side), a rough estimate gives $k_F d \approx 1$. For the polySi gate device which has an asymmetric profile (different k_F values for electron and hole doped sides), a rough estimate gives $k_F d \approx 1 \sim 10$. These estimates put our junction devices in an intermediate regime between ideal collimation and ideal Veselago lensing. Given these considerations, we proceed to study what one would observe for each case with the real junction parameters. Figure 4.5(A) shows the device structure in our model where we have an electron injection source with finite contact width W_s on the left side of the junction and an extended drain on the right side to reduce multiple scattering from the edge and quantum interference effects. This device is a generic structure for both polySi gate and graphite gate devices (in the graphite case, Gate 2 region is controlled by the back gate).

4.2.1 Effect of roughness on collimation

We first look at collimation. We use an extended source ($W_s =$ device width (160 nm) for Fig. 4.5(B, C)) to evaluate the performance as this permits electrons to arrive with various

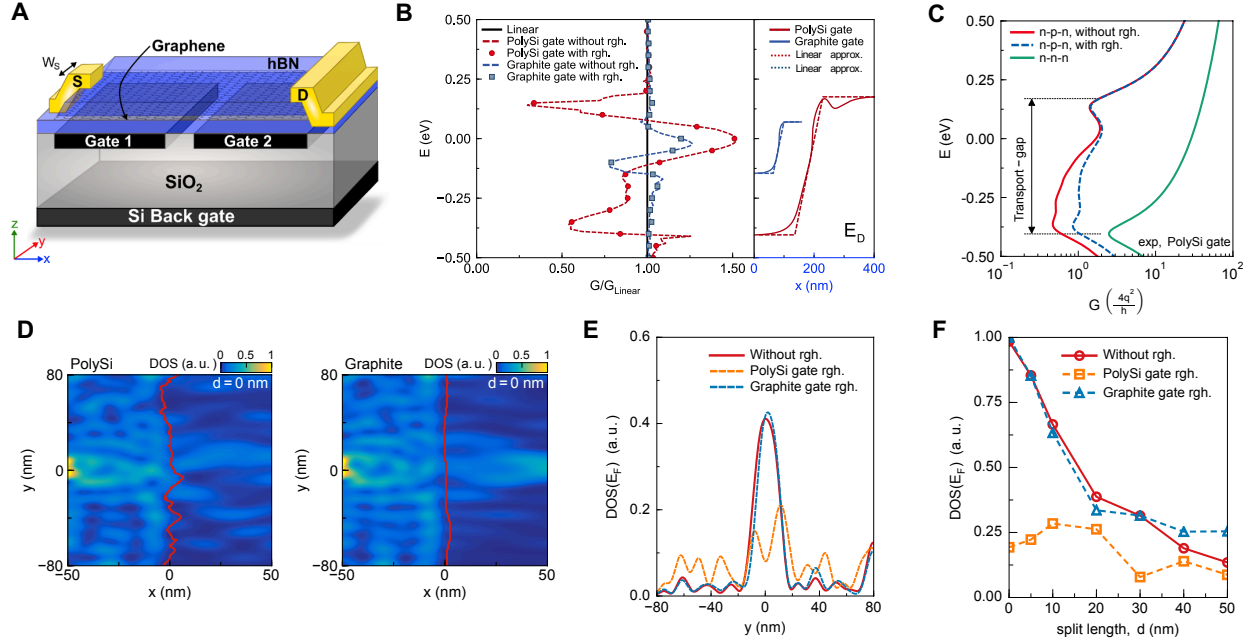


Figure 4.5: (A) Schematic of device structure to evaluate the performance of collimation and Veselago lensing under practical junction parameters. (B) Effect of non-linear potential in collimation of a single p-n junction. Junction interface roughness plays no role, whereas potential non-linearity causes the conductance to deviate from the linear case. (C) Effect of interface roughness on a double junction device. The added roughness increases the conductance resulting in a reduced current on/off ratio for such a device. (D) LDOS plot for the polySi and graphite gate devices. Both plots are for $d = 0$ (abrupt junction) to show the effect of roughness alone. (E) Linecut at $x = 50$ nm from (D). Focusing is evident for the ideal and graphite gate devices but not the polySi gate device. (F) Effect of junction width on focusing. Signal intensity at the focal point decays rapidly with increasing junction width due to reduced electron transmission. Reprinted with permission from Ref. [88]. © 2019 American Chemical Society.

incidence angles allowing us to assess the angular filtering function. We calculate the low bias conductance G of a single p-n junction at 300 K,

$$G(E_F) = \frac{4q^2}{h} \int T(E) \left(-\frac{\partial f_0}{\partial E} \right) dE \quad (4.1)$$

Here, $T(E)$ is the transmission probability, $f_0 = f(E - E_F)$ is the Fermi function, q is the electron charge and h is Planck's constant (see Supplementary section 5 for calculation details). G , the conductance, characterizes the efficiency of electron transmission through the p-n junction. A higher conductance thus indicates a lower collimation, and vice versa.

We first calculate the conductance for a linear doping profile with no roughness, which we use as a baseline for our calculations of real junctions. We then consider both the graphite and the polySi gate structures, and calculate the transmission through the junction with and without lateral roughness included in the calculation. The right panel of Fig. 4.5b shows the experimentally measured non-linear junction profile and its linear approximation for both devices which are both used in the calculation. Finally, the conductance for each case is scaled by the conductance for the linear doping profile, and the resultant conductance ratios are plotted in Fig. 4.5b. We clearly see that conductance of both devices deviates from the linear case in the p-n junction regime ($-0.4 \text{ eV} < E < 0.175 \text{ eV}$ for polySi and $-0.15 \text{ eV} < E < 0.07 \text{ eV}$ for graphite). This deviation is highest for the energy values close to the energy boundary of the junction where the slopes of the non-linear potential also differ most compared to the linear approximation. The deviation from unity in the conductance ratio is due to a variation in the slope for the non-linear case: a smaller slope of the potential is associated with a larger junction width d , which, in turn, creates a longer effective barrier (from the transmission probability formula stated above) and hence lower transmission probability (and hence higher collimation) and lower conductance. Similarly, larger slopes lead to higher transmission/conductance and lower collimation. The disadvantage of having a non-linearity is that the conductance $G(E_F)$ (hence the collimation) now strongly depends on the actual energy position of the Fermi level E_F which itself is hard to control in real junction devices due to the substrate doping. In other words, the non-linearity makes collimation performance unpredictable, and therefore is a disadvantage from a design point of view. At the level of a single junction, the non-linearity in the junction doping profile plays an important role in determining the conductance of the junction, while the roughness does not have a significant impact on the conductance.

Although roughness does not greatly influence single junction conductance, it does affect the conductance of a two junction device. Sajjad *et al.* proposed using a graphene double p-n junction for electronic switching, taking advantage of a highly angle selective transmission [60].

For such a two junction device where electron transmission through each junction is coupled with the other, one can create an effective gate-tunable “transport gap” in graphene to turn the current on and off by using it in a unipolar regime or bipolar regime (p-n junction). We have calculated the electron conduction through such a two junction device. Figure 4.5c shows results for the polySi gate devices. The green curve corresponds to a unipolar regime while the red curve represents a bipolar regime with a much lower conductance within the “transport gap”. However, as we add the interface roughness, the conductance in the bipolar regime increases (blue dashed curve), implying a reduction in the effective current on/off ratio for such a device.

4.2.2 Effect of roughness on Veselago lensing

Next we look at Veselago lensing. For the Veselago simulation, we adopt a point source in our model ($W_s (= 32\text{nm}) \ll \text{device width} (=160 \text{ nm})$) and a symmetric junction (equal doping on both sides) to evaluate the impact of the junction width and interface roughness on the focusing. We first consider an abrupt junction ($d = 0$) to isolate the contribution of interface roughness. Figure 4.5d shows the calculated LDOS for polySi gate and graphite gate devices. We also calculate the LDOS for the ideal junction without roughness as a comparison [result not shown in Fig. 4.5(D)]. The LDOS was calculated using $\text{LDOS}(x_i, y_i; E) = A(x_i, y_i; E)/2\pi$ where (x_i, y_i) is the coordinate of site i and A is the spectral function given by $A = 2\text{Im}\{G^R\}$ with G^R being the retarded Green’s function obtained from the recursive Green’s function algorithm [95]. LDOS represents the probability density profile in the channel. In the case of Veselago focusing, electrons coming from the left point contact (source) should converge to a point on the right side of the junction at an equal distance from the junction. Therefore, the probability of finding electrons in the vicinity of the focal point should be higher and hence LDOS should also be higher than in the rest of the channel. Figure 4.5(D) suggests that Veselago focusing is robust against relatively low roughness of the graphite gate for an abrupt junction. However, focusing characteristic is strongly smeared out at the high

roughness seen in the polySi gate, even for an abrupt junction. This is clearly shown in Fig. 4.5(e), where line-cuts of Fig. 4.5(D) at $x = 50$ nm are compared. For the polySi gate case, the junction roughness plays an important role in randomizing the electron paths as they transit across the junction in a manner similar to roughness on an optical lens, and this effect is clearly seen in the LDOS as well. As the roughness is reduced (as is the case with the graphite gate), the focusing characteristics of the junction reappear and the LDOS becomes indistinguishable from the ideal junction case. We also repeat this calculation by varying the junction width d to see its impact on the focusing. In Fig. 4.5(f), we plot the central peak intensity (at $y = 0$ nm) of the $x = 50$ nm line-cut as a function of junction width d for ideal, polySi gate and graphite gate roughness cases. Again, the graphite gate shows a comparable performance to the ideal case, while the polySi gate randomizes the electron trajectories so much that the signal at the center point fluctuates at all widths. When the junctions are smooth enough (ideal and graphite gate cases), the focusing decays rapidly as the junction width d increases, since fewer electrons can penetrate the junction and thus the signal intensity is reduced significantly. Two lessons are learned from these simulations. Firstly, the graphite gate is uniform and smooth enough to realize Veselago lensing whereas the polySi gate is fundamentally limited in these respects. Secondly, even in a perfect junction, the junction width sets another limitation on lensing, thus preventing the graphite gate device from lensing even though it meets other requirements. In the future, one should consider exploring improved devices using graphite gates, for instance with thinner h-BN, to utilize the uniformity and smoothness of the graphite gate junctions and to create sharper junctions where signatures of Veselago lensing may be seen in experiments.

4.2.3 Conclusions

We have reported atomic level characterization of two state-of-the-art types of graphene p-n junction devices using STM/STS. We find inherent imperfections as each junction exhibits finite width and lateral roughness as well as a chemical potential profile non-linearity and

asymmetry which are directly measured with STS. We show that a significant improvement is exhibited in these parameters if one adopts an exfoliated graphite gate device geometry. To investigate the impact of these imperfections, we use our experimental findings as inputs into graphene p-n junction simulations of two important electron-optical applications: collimation and Veselago lensing. For Veselago lensing, junction roughness makes it impossible for polySi gates to lens for any junction width; graphite gates, although smooth enough, are inhibited by a junction width too large to lens. Collimation, as characterized by the conductance, is robust against junction roughness, but significantly affected by the non-linearity in the potential profile. These results represent an advance in characterizing and analyzing graphene p-n junctions for both fundamental research and practical applications, and provide insights into future research directions for electron optics based devices.

4.3 Characterization of edge roughness

Edge roughness plays an important role in electron optics based devices as angular resolution of electrons is utilized. Ideally specular reflections from an edge is considered in simulation (section 3.2), but in experiments non-specular reflection is observed [32, 45]. The specularity (S) defined as a ratio of second resonance and first resonance in TMF experiments is a well known parameter in literature. On the other hand, in section 3.3, 4.1, and 3.4, we introduced an edge roughness parameter σ_e . In this section, we connect these two parameters and develop an analytical relation which is validated through numerical simulations. In this section, a simple hallbar like structure (Fig. 2.1) is considered without any p-n junction. Contact (middle) to contact (middle) distance is L_{CC} and contact width is W_c . We first derive the specularity parameter (S) in terms of edge roughness parameter (σ_e) and contact injection parameter (σ_{inj}) for single electron picture and then for multi-electron picture. To simplify our model, we assume the probability of electron injection is highest at the middle of the contact. For the receiving contact we will consider the full width (W_c) of the contact.

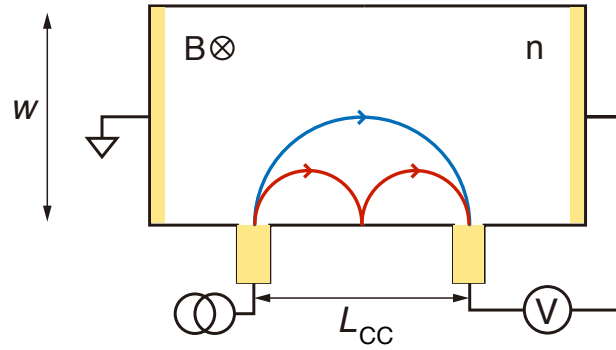


Figure 4.6: **Specularity characterization device schematic.** Blue color shows the first resonance path and red color shows the second resonance path.

4.3.1 Single electron picture, $\sigma_{inj} = 0^\circ$

In single electron picture, contact injection model is in its simplest form. All the electrons are considered to be coming out of the left bottom contact middle point at an injection angle of zero degree. So in this case, first resonance relative peak value will always be one. Second resonance peak is calculated by the ratio of number of electrons collected by the bottom right contact after electrons are hitting the edge and the number of electrons coming out from the bottom left contact. After hitting the edge, a random angle is added to its original specular path (Fig. 4.7). The randomization follows Gaussian distribution with standard deviation σ_e .

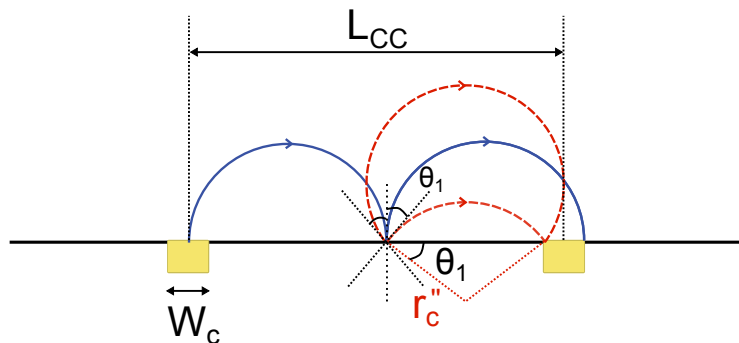


Figure 4.7: **Single electron path for rough edge.** After hitting the edge a random angle is added to its specular path. The randomization follows a Gaussian distribution with standard deviation of σ_e . Electron is injected from left bottom contact. After hitting the edge, blue color shows the specular reflection path and red dash color shows the non-specular paths which still end up at the bottom right contact.

$$S_{\theta_{inj}(=0)} = \text{erf} \left(\frac{\theta_1}{\sqrt{2}\sigma_e} \right) \quad (4.2)$$

Let, $L_c = L_{CC}/2$ and $L = (L_{CC} + W_c/2)/2$ So,

$$\theta_1 = \cos^{-1} \left(\frac{L - W_c}{2r_c''} \right) \quad (4.3)$$

Here, $r_c'' = \frac{L_{CC} + \frac{W_c}{2}}{2}$

4.3.2 Multi-electron picture ($\sigma_{inj} > 0^\circ$)

First resonance

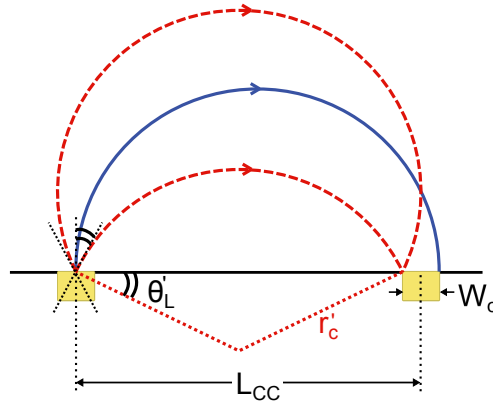


Figure 4.8: **Path of electron for first resonance.** Here θ'_L is the highest injection angle for which electron can still reach the receiving contact.

Let r'_c is the cyclotron radius for first resonance peak, then

$$r'_c = \frac{L_{CC} + \frac{W_c}{2}}{2}$$

If θ'_L is the highest injection angle for which electron can still reach the receiving contact, then

$$\theta'_L = \cos^{-1} \left(\frac{L_{CC} - \frac{W_c}{2}}{2r'_c} \right)$$

Now transmission can be calculated for the first resonance peak from below equation.

$$T' = 2 \times \frac{1}{2} \operatorname{erf} \left(\frac{\theta'_L}{\sqrt{2}\sigma_{inj}} \right) \quad (4.4)$$

Second resonance

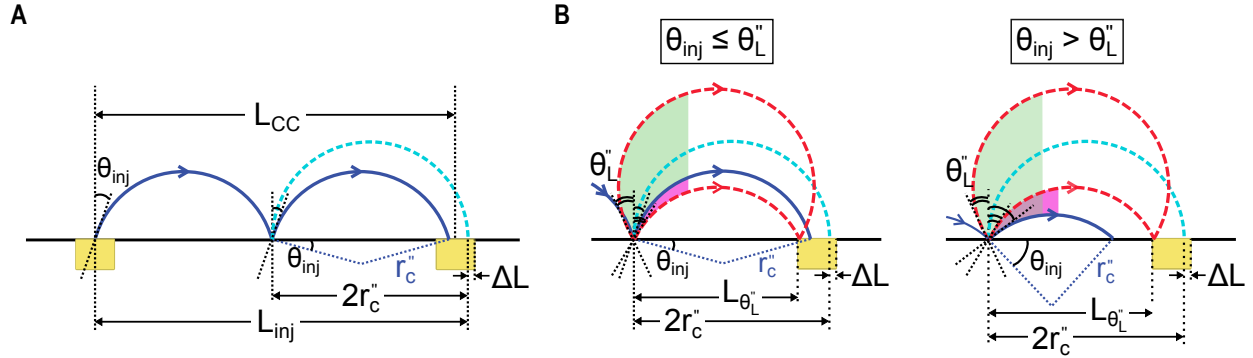


Figure 4.9: **Path of electron for second resonance with specific injection angle.** (A) Electron is injected from bottom left contact with θ_{inj} . For a specular reflection it will bounce on the edge and come back with an angle equal to θ_{inj} . (B) Non specular reflection at the edge. Depending on θ_{inj} and θ_L value, transmission can be calculated for non specular reflection.

If r_c'' is the cyclotron radius for second resonance peak, which can be found for $\theta_{inj} = 0^\circ$

$$r_c'' = \frac{L_{cc} + \frac{W_c}{2}}{4}$$

Now from Fig. 4.9

$$L_{inj} = 2r_c'' \cos \theta_{inj} + 2r_c''$$

For electrons to end up at receiving contact, $L_{inj} > L_{cc} - \frac{W_c}{2}$.

$$\Delta L = L_{cc} + \frac{W_c}{2} - L_{inj}$$

$$L_{\theta_L''} = 2r_c'' - (W_c - \Delta L)$$

$$\theta_L'' = \cos^{-1} \left(\frac{L_{\theta_L''}}{2r_c''} \right)$$

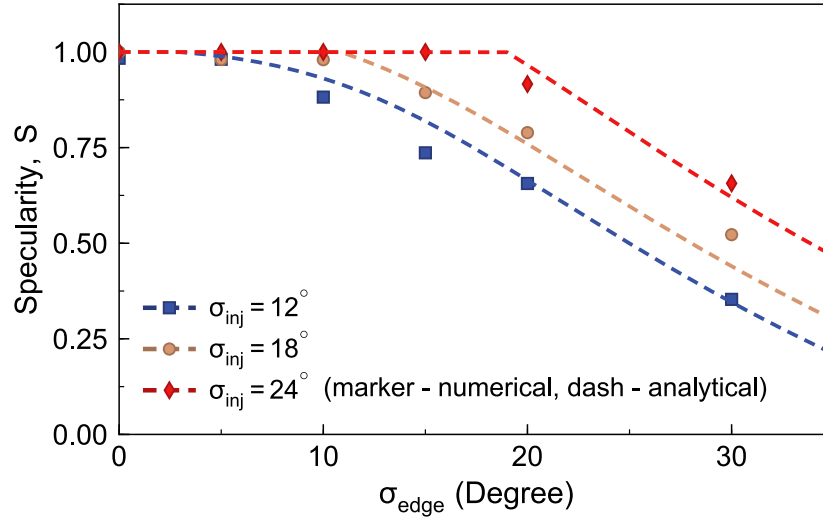


Figure 4.10: **Specularity vs. edge spreading.** Numerical simulation is from ray tracing method.

$$T''_{\theta_{inj}} = \begin{cases} \frac{1}{2} \left[\operatorname{erf} \left(\frac{\theta'_L + \theta_{inj}}{\sqrt{2}\sigma_{edge}} \right) + \operatorname{erf} \left(\frac{\theta'_L - \theta_{inj}}{\sqrt{2}\sigma_{edge}} \right) \right], & \text{if } \theta_{inj} \leq \theta_L \\ \frac{1}{2} \left[\operatorname{erf} \left(\frac{\theta'_L + \theta_{inj}}{\sqrt{2}\sigma_{edge}} \right) - \operatorname{erf} \left(\frac{\theta_{inj} - \theta'_L}{\sqrt{2}\sigma_{edge}} \right) \right], & \text{if } \theta_{inj} > \theta_L \end{cases}$$

From individual transmission ($T''_{\theta_{inj}}$) for each θ_{inj} , we can take Gaussian weighted integral to have the total transmission, T'' for second resonance.

$$T'' = \frac{1}{\operatorname{erf} \left(\frac{\theta_{inj, Lim}}{\sqrt{2}\sigma_{inj}} \right)} \int_{-\pi/2}^{\pi/2} T''_{\theta_{inj}} \frac{1}{\sqrt{2\pi}\sigma_{inj}} \exp \left(-\frac{\theta_{inj}^2}{2\sigma_{inj}^2} \right) d\theta_{inj} \quad (4.5)$$

Specularity

$$S' = \frac{T''}{T'} \quad (4.6)$$

$$S = S' - (1 - S') \quad (4.7)$$

Figure 4.10 shows the specularity versus edge roughness parameter (σ_e) for different injection angle spreads (σ_{inj}). Numerical simulation is from ray tracing method (see details in Appendix A), which shows good agreement with the analytical expression we developed. With increasing

σ_e , the specularity reduces as non-specular reflection probability increases. In future works, we will connect these two parameters σ_{inj} and σ_e with physical graphene-edge roughness parameters like RMS value of amplitude and correlation length.

Chapter 5

Characterization of graphene p-n junction and Corbino geometry

5.1 Graphene p-n junction characterization

The discovery of graphene as a new two-dimensional (2D) electron system with high intrinsic mobility has led to a surge of interest in applying it towards solid state electron optics systems where the wave nature of electrons is explored in order to manipulate the flow of an electron beam, analogous to light optical systems [96]. The key to success in this business is to create the electronic counterpart of optical components in solid state systems, such as mirrors, lenses, prisms, wave guides, beam splitters and collimators. Early experiments employed electrostatically defined nanostructures, such as quantum point contact, to demonstrate such electron optics in a 2D electron gas formed at the AlGaAs/GaAs heterostructure, taking advantage of the sample's ballistic electron transport [21, 97, 98]. A breakthrough came when graphene emerged as a new 2D electron system with high intrinsic mobility which allows ballistic transport over micrometer length scale even at room temperature [12]. The ballistic transport, together with the easy tunability of graphene's carrier type and density via electrostatic gating, makes it very appealing for electron optics applications. Experimental efforts have been

devoted to exploring the aforementioned functions in graphene-based electron optics, such as wave-guiding [33,99], focusing [32] and collimating [100], fueled by theoretical proposals of how graphene can be used to create new electron optics devices [24,55,60,101,102]. A key component in these studies is the graphene p-n junction, created by an interface between a p-type (hole-like) and an n-type (electron-like) region on the same graphene sheet [36,103]. Part of this chapter is reprinted with permission from Ref. [88] coauthored with X. Zhou, A. Kerelsky, D. Wang, K. M. M. Habib, R. N. Sajjad, P. Agnihotri, J. U. Lee, A. W. Ghosh, F. M. Ross, and A. N. Pasupathy. Copyright 2019 American Chemical Society.

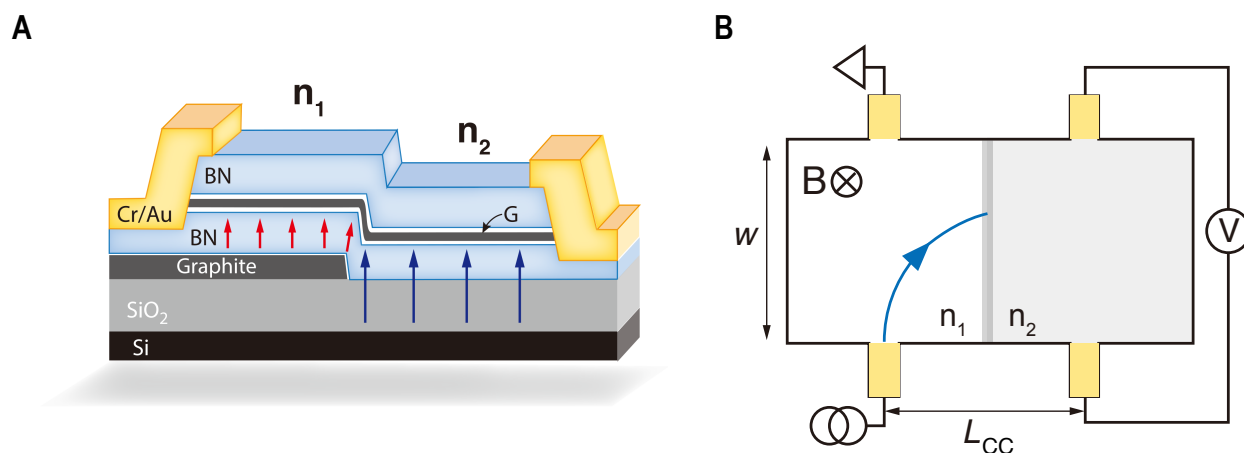


Figure 5.1: **Graphene p-n junction characterization.** (A) Transverse magnetic field is used to focus electrons onto a split gate junction at variable incident angles. The cyclotron radius, determined by the magnetic field and Fermi momentum (or related carrier density), determines the incidence angle. The density difference across the boundary, induced by the two gate voltages, determines the refraction angle (see text). (B) Schematic of split gate device. A naturally cleaved graphite edge is utilized to define an atomically smooth electrostatic boundary. Reproduced from Ref. [32]. Reprinted with permission from AAAS.

We demonstrate how four-probe transverse magnetic focusing data can be used to characterize quasi-ballistic graphene junctions. The positions of the magnetoresonance peaks give us the contact-to-contact separations, while the presence of kinks in these data relate to the location of an electrostatically generated p-n junction. We develop an analytical expression for the second resonance for TMF experiment of a graphene p-n junction which can be useful for finding contact to contact distance as well as exact location of the p-n junction

along with the first resonance analytical expression from Ref. [32]. Such a detailed characterization may help us design quasi-ballistic graphene devices, such as Klein tunnel transistors.

5.1.1 Contact to contact distance

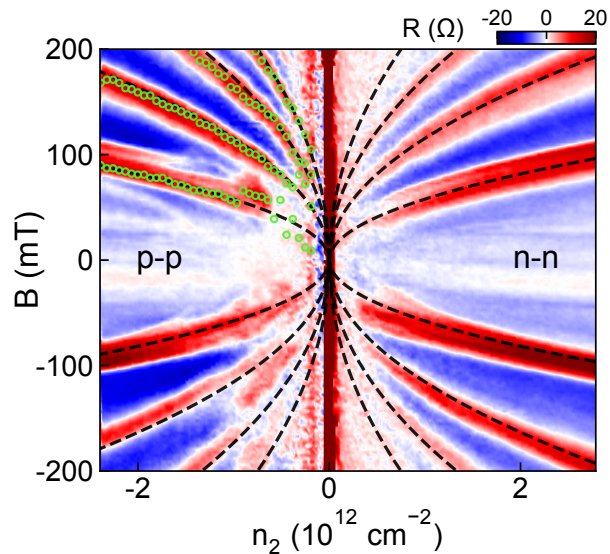


Figure 5.2: **Extracting L_{CC} from the experiment (density matched).** We extract L_{CC} by fitting Eq. (5.2) for matched density experiment peak points. Here, $L_{CC} = 4.05 \mu\text{m}$ which is also supported by the AFM results from experiment [32]. Black dash lines show parabolic fitting relation $B \sim \sqrt{n}$, which is expected for p-p and n-n cases. Green dots are the peak points in experiment. It shows that Reproduced from Ref. [32]. Reprinted with permission from AAAS.

Contact to contact distance (L_{CC}) is one of the important parameters in four probe TMF experiments. Most of the other parameters are derived from equations where contact to contact distance is used as a known parameter from Atomic Force Microscopy (AFM) data. Here, we will show two methods to extract L_{CC} without doing AFM characterization. We also benchmark our data against AFM results from Ref. [32] to validate our analytical extraction procedure.

TMF experiment for a hallbar like structure is a well known procedure in graphene literature [32, 45]. The below equation can be derived from Lorentz force due to magnetic

field applied in transverse direction and centrifugal force for a rotating object (here electrons are considered as classical particle as billiard balls [46]).

$$B = \left(\frac{2\hbar k_F}{qL_{CC}} \right) p = \left(\frac{2\hbar\sqrt{\pi n}}{qL_{CC}} \right) p \quad (5.1)$$

where $p - 1$ is the number of reflections off the edge of the system (for example, $p = 1$ corresponds to a direct injector to collector trajectory, without reflections). \hbar is the reduced Plank constant, e is the elementary charge, $k_F = \sqrt{\pi n}$ (for graphene) is the Fermi momentum, with n being the carrier density.

Figure 5.2(A) shows matched density experiment results for both electrons (negative n) and holes (positive n). We can easily fit the parabolic relation between B and n in Eq. (5.1) to extract L_{CC} which is found to be $\sim 4.05 \mu\text{m}$.

TMF experiment for ballistic graphene p-n junction has been reported recently with high quality junction with graphite gate [32] [Fig. 5.2(B)]. Due to its high quality junction, electron optics at the junction applies almost like an ideal interface for two materials with different refractive indexes. For the p-p' side, first resonance analytical equation has already been derived in SI of Ref. [32]. In this work, we also show the analytical expression for second resonance which consists of two piece-wise equations due to different geometrical path. Two equations converge at a single point which we call the 'kink' (explained in details in the next section). From first and second resonance analytical equations for p-p' side, we extract $L_{CC} = 4.05 \mu\text{m}$ which is close to the matched density experiment described earlier. AFM experiment gives the distance between contacts close to be $4 \pm 0.05 \mu\text{m}$ which confirms that both the procedures can predict the contact to contact distance.

For both cases,

$$\sqrt{n_1} \sin(\theta_1) = \sqrt{n_2} \sin(\theta_2) \quad (5.2)$$

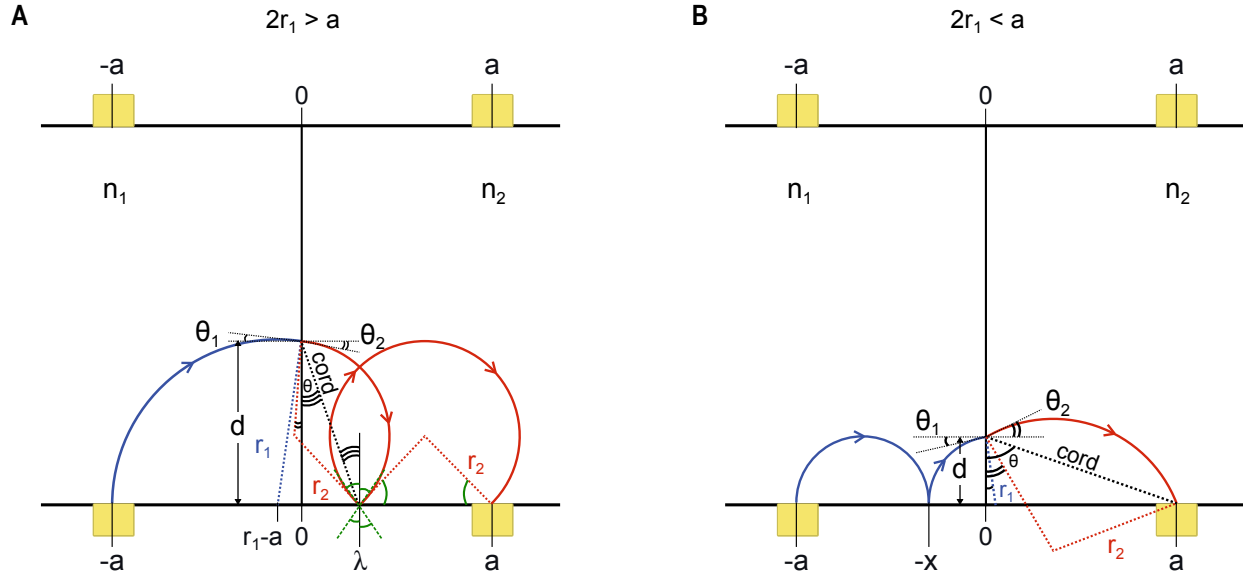


Figure 5.3: **Second resonance paths for p-p' side in TMF experiment.** (A) $|n_1| > |n_2|$ or, $2r_1 > a$. (B) $|n_1| < |n_2|$ or, $2r_1 < a$.

where n_1 and n_2 are the electron densities on left and right sides respectively. θ_1 is the incident angle and θ_2 is the refraction angle.

$$B = \frac{\hbar\sqrt{\pi n}}{qr} \quad (5.3)$$

where B is the magnetic field, \hbar is the reduced Planck's constant, n is the electron density, r is the cyclotron radius of electrons.

For $|n_1| > |n_2|$ or, $2r_1 > a$

From Fig. 5.3(A),

$$\begin{aligned} r_1^2 &= d^2 + (r_1 - a)^2 \\ \text{or, } d &= \sqrt{2ar_1 - a^2} \end{aligned} \quad (5.4)$$

Now,

$$2r_2 \cos(x) + \lambda = a \quad (5.5)$$

where $x = \frac{\pi}{2} - \theta_2 - 2\theta$, $\text{cord} = 2r_2 \cos(\theta_2 + \theta)$ and $\lambda = \text{cord} \cdot \sin(\theta)$.

So, from Eq. (5.5),

$$2r_2 \cos\left(\frac{\pi}{2} - \theta_2 - 2\theta\right) + 2r_2 \cos(\theta_2 + \theta) \sin(\theta) = a \quad (5.6)$$

or, $2r_2 \cos(\theta_2 + \theta) \sin(\theta) = a - 2r_2 \sin(\theta_2 + 2\theta)$

We check the convergence of both sides of Eq. (5.6) with different angles (θ) and magnetic fields (B) for specific electron density (n_2) on right side of the junction. Thus we find the solution pair (n_2, B).

For $|n_1| < |n_2|$ or, $2r_1 < a$

From Eq. (5.2) and Fig. 5.3(B),

$$\begin{aligned} \sin(\theta_2) &= \sqrt{\frac{n_1}{n_2}} \sin(\theta_1) \\ &= \sqrt{\frac{n_1}{n_2}} \frac{3r_1 - a}{r_1} \end{aligned} \quad (5.7)$$

and

$$\tan(\theta) = \frac{\sin(\theta)}{\cos(\theta)} = \frac{\frac{a}{\text{cord}}}{\frac{d}{\text{cord}}} \quad (5.8)$$

For finding d ,

$$\begin{aligned} d^2 + (r_1 - x)^2 &= r_1^2 \\ \text{or, } d^2 + (r_1 - a + 2r_1)^2 &= r_1^2 \\ \text{or, } d &= \sqrt{6ar_1 - a^2 - 8r_1^2} \end{aligned} \quad (5.9)$$

For finding cord length,

$$\begin{aligned} \text{cord} &= \sqrt{d^2 + a^2} \\ &= \sqrt{6ar_1 - 8r_1^2} ; [\text{using Eq. (5.9)}] \end{aligned} \quad (5.10)$$

From Fig. 5.3(B),

$$\begin{aligned}
 2r_2 \cos(\theta - \theta_2) &= \text{cord} \\
 \text{or, } 2r_2[\cos(\theta_2) \cos(\theta) + \sin(\theta_2) \sin(\theta)] &= \text{cord} \\
 \text{or, } \sqrt{1 - \frac{n_1}{n_2} \left(3 - \frac{a}{r_1}\right)^2} \sqrt{6ar_1 - a^2 - 8r_1^2} + \sqrt{\frac{n_1}{n_2} \frac{3r_1 - a}{r_1}} a &= 3a \sqrt{\frac{n_1}{n_2}} - 4r_1 \sqrt{\frac{n_1}{n_2}}
 \end{aligned} \tag{5.11}$$

We solve Eq. (5.11) for r_1 where n_1 , n_2 , and a are known. Then from r_1 , we find the magnetic field B using Eq. (5.3).

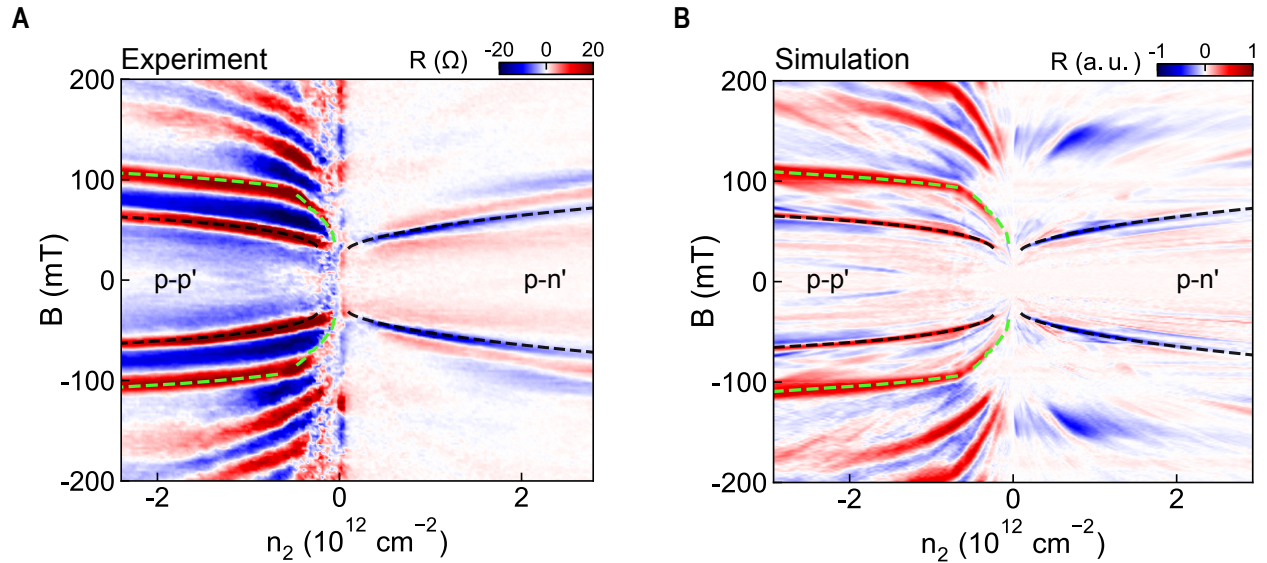


Figure 5.4: **Second resonance analytical expression (A) Experiment. (B) Semi-classical ray tracing simulation.** Black dash line is from the analytical expression of first resonance [32]. Green dash line is from the analytical expression of second resonance (this work) in the p-p' side. Green dash line clearly breaks down at the kink point where $|n_1| = |n_2|$. Part of this figure is reproduced from Ref. [32]. Reprinted with permission from AAAS.

5.1.2 Junction position

The ‘kink’ in p-p’ side for TMF experiment happens when electrons perfectly completes two semicircle, in other words hit the edge at the junction. So from the position of the ‘kink’ we can extract the position of the junction. From Eq. (5.1), we can write the equations for

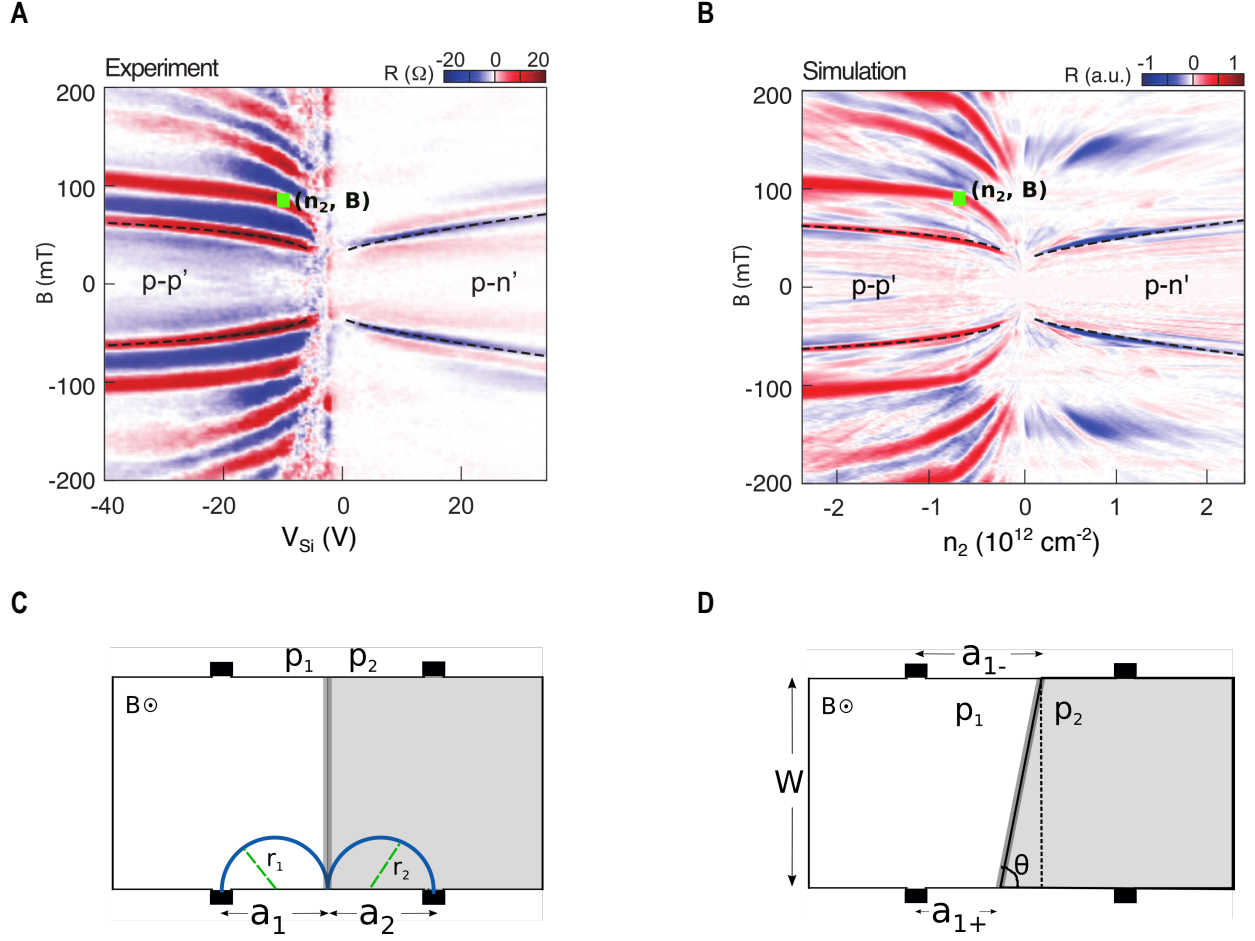


Figure 5.5: **Extracting Junction Position.** (A) The point shown in the experimental plot represents the kink point when the cyclotron path is exactly half circle on the left and right side of the junction represented in (C), (B) Simulation also shows distinct kink point. The values of a_1 and a_2 extracted from both (A) and (B) using Eqs. (5.12) and (5.13) agree with each others. Part of this figure is reproduced from Ref. [32]. Reprinted with permission from AAAS.

extracting a_1 and a_2 .

$$B = \left(\frac{2\hbar\sqrt{\pi n_1}}{q2r_1} \right) = \left(\frac{2\hbar\sqrt{\pi n_1}}{qa_1} \right) \quad (5.12)$$

$$B = \left(\frac{2\hbar\sqrt{\pi n_2}}{q2r_2} \right) = \left(\frac{2\hbar\sqrt{\pi n_2}}{qa_2} \right) \quad (5.13)$$

where, n_1 is constant as we fix the gate voltage ($V_{graphite}$) of the left side (p type) and B is the value shown in Fig. 5.5 for $n_2 = n_1$.

Junction tilt can be calculated from a_{1+} and a_{1-} (extracted from positive B and negative B quadrant kink points respectively for p-p' side), and W (device width).

$$\theta = \tan^{-1} \left(\frac{W}{|a_{1-} - a_{1+}|} \right) \quad (5.14)$$

5.2 Corbino geometry

In recent years, exploring bulk properties of graphene using Corbino geometry (especially useful for resolving fractional quantum hall edge states) have been demonstrated in multiple studies [104–108]. This kind of devices can be useful for probing electron optics in monolayer as well as bilayer graphene due to their high mobility thus low scattering probability. Due to the limitation of the incident angle range for a hallbar like structure (Fig. 2.1 and 2.2), we investigate Corbino disk like structures for graphene p-n junctions both in monolayer and bilayer graphene. Our aim is to study these simple structures and understand Klein (monolayer) and anti-Klein tunneling (bilayer) in depth. All the experimental data shown in this section are provided by Yihang Zeng and Cory R. Dean from [Dean Lab, Columbia University, NY](#).

5.2.1 Monolayer graphene

Figure 5.6(A, B) show the side and top view of the device. The device consists three circular region controlled by one bottom and on top gate. Inner (electron density, n_1) and outer (n_3) regions are controlled by bottom gate and middle region (n_2) is controlled by top gate. Thus we form two junctions and the electrostatics can be controlled by h-BN thickness. Top h-BN thickness is 31 nm and bottom h-BN thickness is 116 nm, $R_{contact.in} = 0.5 \mu\text{m}$, $R_{in} = 1 \mu\text{m}$, $R_{out} = 2.5 \mu\text{m}$, and $R_{contact.out} = 3 \mu\text{m}$. In these calculations, contact resistance of $250 \Omega\text{-}\mu\text{m}$ as it is a two prob experiment (also benchmarked by high density experimental resistance). Figure 5.6(C, D) shows ray tracing simulation paths for electrons for n-n'-n and n-p'-n cases

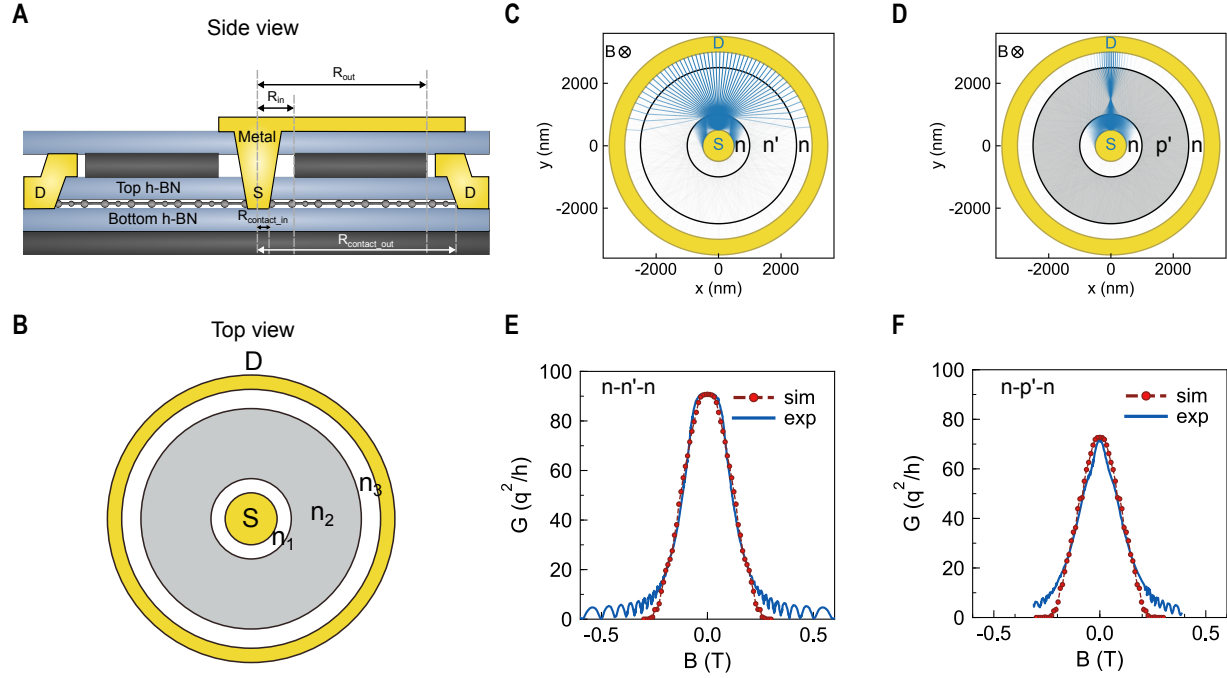


Figure 5.6: **Electron optics in Corbino graphene (monolayer) p-n junction.** (A) Side view of Corbino monolayer GPNJ device. (B) Top view of Corbino monolayer GPNJ device. (C) Ray tracing paths for n-n'-n device for $B = 0$ mT. Most of the electrons go through the junctions. (D) Ray tracing paths for n-p'-n device for $B = 0$ mT. Most of the electrons other than close to zero degrees incidence are reflected back. (E) Conductance between the source and the drain for n-n'-n. (F) Conductance between the source and the drain for n-p'-n. Experimental data and device structure are provided by Yihang Zeng and Cory R. Dean from [Dean Lab, Columbia University, NY](#).

respectively. For n-p'-n case, most of the electrons are filtered out other than close to zero degree incidences. Figure 5.6(E, F) show conductance variation versus magnetic field for n-n'-n and n-p'-n cases respectively. For n-p'-n case, peak conductance is less than n-n'n case due to exponential filtering Eq. (2.1) of electrons for higher angles. The conductance profile is also sharp for n-p'-n case for the same reason. The starting decay point for n-n'-n case can be analytically calculated from Ref. [109]. For high magnetic field, semi-classical results do not match experimental data due to quantum hall regime. The oscillations in experimental data are called Shubnikov-de Haas (SdH) oscillations [110].

5.2.2 Bilayer graphene

When two graphene sheets are oriented at sixty degrees relative to each other to create so-called Bernal stacking, the A and B sublattice atoms get coupled across the planes. This extra coupling turns the linear dispersion into a quadratic one. We can treat this as simply two copies of the original monolayer graphene, but tied together by only the $A_2 - B_1$ terms.

The winding number for bilayer graphene (BLG) is twice that of monolayer graphene, so that the pseudospin flips over at an angle of only $\theta = \pi/2$ and reverts at angle $\theta = \pi$. This means for normal incidence (i.e., 1-D) the entire conduction band shares the same pseudospin, while as always, the valence band has the opposite pseudospin. The implications for BLG p-n junctions is that electrons cannot go forward from conduction to valence band without flipping their pseudospins. For an n-n' or p-p' junction however, every branch of the bands are accessible. Proceeding as before [14, 17], but with the bilayer wave-function, we can show that the transmission probability for an abrupt junction

$$T = \frac{2 \sin(2\theta_1) \sin(2\theta_2)}{1 \mp \cos(2\theta_1 + 2\theta_2)} \quad (5.15)$$

with $-$ for n-n' and $+$ for p-n' junctions. Here, θ_1 is the incident angle and θ_2 is the refraction angle. It is easy to see that at $\theta_1 = 0$, we get zero transmission, even for symmetric p-n junctions, which means that we get no forward scattering for normal incidence, which we call anti-Klein tunneling. Like monolayer Corbino structure, a similar experiment can be done for bilayer. Figure 5.7(A) show the side view of the device. One intriguing aspect for the bilayer graphene conductance shown in Fig. 5.7(B) is, at $B = 0$ T we see a dip unlike monolayer graphene due to anti-Klein tunneling. The peak value for conductance at $B = 0.039$ T is due to the matching of pseudospin on both sides of the junction for mean electron incident angle and the transmission becomes highest.

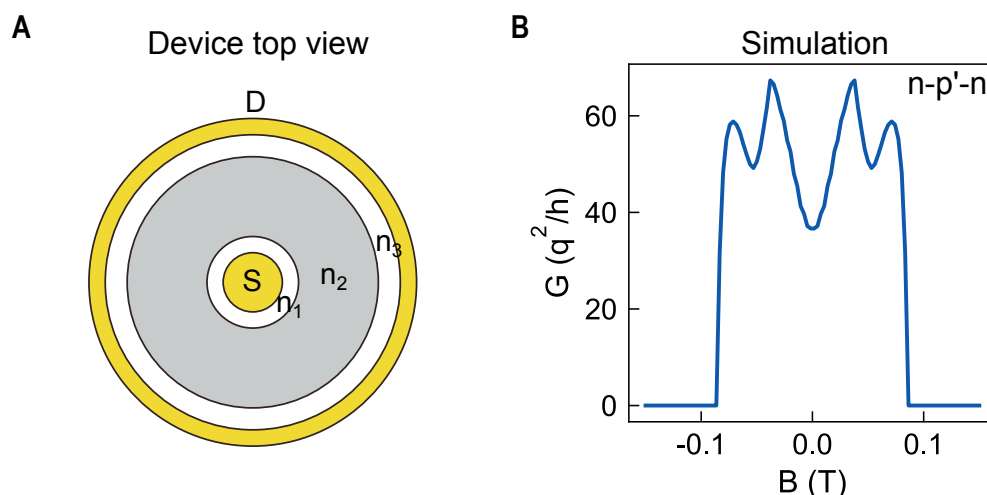


Figure 5.7: **Electron optics in Corbino graphene (bilayer) p-n junction.** (A) Side view of Corbino bilayer GPNJ device. (B) Conductance between the source and the drain for n-p'-n. The dip at $B = 0$ T is due to the anti-Klein tunneling in bilayer graphene. The experimental device structure is provided by Yihang Zeng and Cory R. Dean from [Dean Lab, Columbia University, NY](#).

5.2.3 Exploring devices with bilayer graphene:

Bilayer graphene has anti-Klein tunneling in the p-n but not p-p' or n-n' sectors. In Fig. 5.8, we show a device structure consisting of one monolayer p-n junction and one bilayer p-n junction. As only junction is used to reflect back electrons to the source for the off state, we expect this device to be free from edge roughness effect. On top of that, the geometry can be considerably simpler and more scalable than the angled junction device shown in chapter 3.

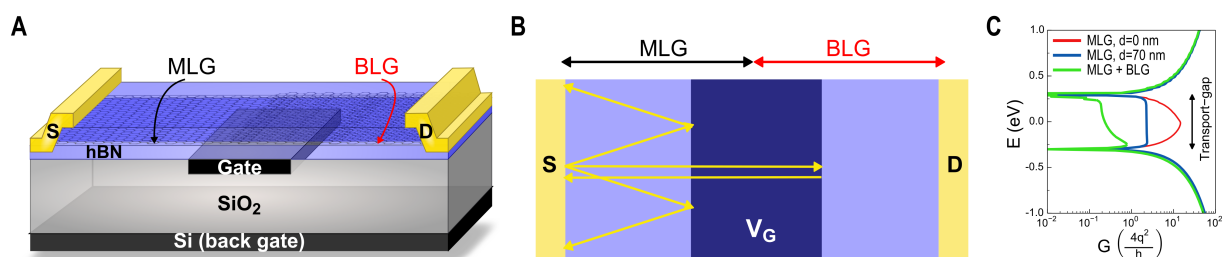


Figure 5.8: **Monolayer and bilayer graphene device.** (A) Side view of MLG+BLG device combining Klein and anti-Klein tunneling. (B) Top view shows expected electron trajectory. (C) An abrupt MLG+BLG p-n junction pair suppresses transmission more aggressively than a single MLG with a 70 nm split length. Split gates are expected to make this exponentially more aggressive.

5.3 Conclusion

In this chapter, we have developed analytical expressions to characterize monolayer graphene p-n junction both in hallbar like structure and Corbino disk geometry and benchmarked with experimental [TMF](#) data. We proposed a Corbino disk geometry to probe anti-Klein tunneling in bilayer graphene (experiment in progress at Dean Lab). Based on these understanding, we showed a device structure consisting of a monolayer and a bilayer p-n junction which is expected less susceptible to edge roughness effect.

Chapter 6

Conclusion

The purpose of this study is to understand electron optics in 2D Dirac materials (especially graphene) and limitations of emerging devices based on this for practical applications in electronic systems. Photon-like band structure of graphene leads to transport properties that can well be described with ray tracing and geometric optics. We discuss how those properties can be controlled by gate geometry. In previous studies, the gate geometry was utilized to achieve a transport gap and high on-off ratio in the absence of specular edge scattering. We show by numerical simulations, in the presence of edge scattering, large-scale graphene still gives large current modulation since the edge effects are minimal. Although the on-off ratio degrades with non-idealities, saturation can be achieved in output characteristics while keeping mobility high, which allows the device to be used for analog applications. The aforementioned findings make the electron optics with 2D Dirac fermions an exciting candidate for new electronic systems.

In this study, we have developed multiple open source simulation techniques to understand the fundamental physics and effects of non-idealities (edge and junction roughness) on device performance. We have one analytical and two numerical tools; the numerical tools include semi-classical ray tracing and fully quantum NEGF methods. Although the analytical method

is the fastest one, it suffers from multiple issues like decoupled transmission for two junction devices, and not capturing leakage due to the multiple electron bounce effect. On the other hand, the NEGF method is capable of capturing all the physics, but it is computationally expensive. We show that the semi-classical ray tracing method results in a good balance between speed and capturing the essential physics for large scale devices. In the semi-classical ray tracing method, we incorporated quantum mechanical effects (tunneling at the junction) by analytical consideration. In the rest of the device, electrons are considered as classical particles. Thus, it overcomes the issues of the analytical tool without being as computationally expensive as the NEGF method. With these simulation tools, we benchmarked experimental results and developed a simple metrology scheme for characterizing graphene p-n junctions as well as edge roughness from TMF data. We found that any geometrical non-idealities like edge roughness and junction roughness play an important role in these devices as we are utilizing the angular resolution of electrons. We also show an example of device geometry engineering (double source device) to improve performance and propose a new device structure (edgeless) which is completely free from edge effects. Extracting parameters from just experimental results and examples of the improved geometries can provide a good guideline for designing electron optics based devices in future.

Many of the electron optics properties that we discussed for monolayer graphene are also applicable to bilayer graphene. However, pseudospin rotates twice as fast in bilayer graphene compared to monolayer due to the double winding number. Because of this, anti-Klein tunneling originates for which transmission probability for zero degree incidence is always zero (for monolayer it is always one). We proposed an experimental method to probe anti-Klein tunneling in bilayer graphene using Corbino geometry. Our initial simulation shows that bilayer graphene p-n junction shows significantly different characteristics with the variation of the magnetic field than the monolayer. Based on Klein and anti-Klein tunneling, we also propose a device structure combining monolayer and bilayer graphene to remove edge effects

and improve device performance.

Future works

There are numerous challenges to address before electron optics based devices can be used for practical applications. These can be divided into two fronts – understanding electron transport in 2D Dirac materials and using that understanding to develop efficient tools to analyze devices. The challenges we faced in our study can lead to a number of possible extensions of our work:

Electron optics in bilayer graphene

In bilayer graphene, a bandgap opens up due to a differential voltage between two layers. This may lead to breaking pseudospin symmetry for a p-n junction in bilayer graphene. Exactly how much this affects the pseudospin symmetry remains unknown. One can study this effect by analytical and NEGF framework to verify the transmission probability across a p-n junction in bilayer graphene.

Effect of phonon scattering on RF performance

Phonon scattering plays an important role in high bias device operation. In the RF calculations, we assumed phonon scattering is not significant as the optical phonon energy for graphene on h-BN is smaller than the transmission gap we generate. In the presence of non-idealities, the transmission gap turns in to a pseudo-gap and phonon scattering may play a role in degrading the performance of the device by providing extra leakage paths inside the transmission gap. One may study the effect of phonon scattering in GKTFET to quantify its effect on performance.

Appendices

Appendix A

Semi-classical ray tracing simulation

Semiclassical ray tracing model relies on the assumption that the most relevant quantum effects in GKT devices manifest during tunneling at the junctions, while for large-scale devices with rough edges, interference effects are expected to be washed out under the gated regions. The underlying assumption is $L_\phi < \text{length of gated region} < L_{mfp}$, where L_ϕ is the phase coherence length and L_{mfp} is the electron mean free path. Accordingly, we throw electrons from a source with random injection angles following a cosine distribution function [98], and evolve each electronic trajectory with constant speed v_F (Fermi velocity) and band effective mass, $m = (E - qV)/v_F^2$ following classical trajectories.

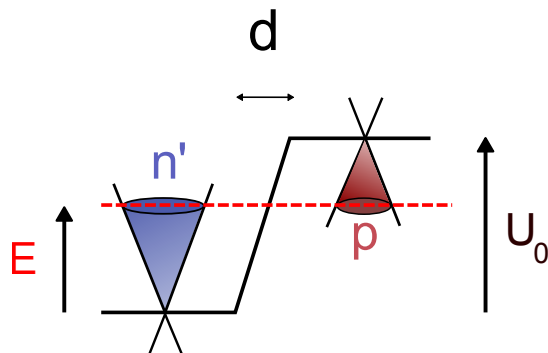


Figure A.1: **Potential profile for asymmetric junction.** For symmetric junction $E = U_0/2$.

The transmission probability (T) of electrons at the junction is calculated [40, 60] using a generalized form of Eq. (17) of Ref. [35] :

$$T(E, \theta_1) = \begin{cases} \Theta(\theta_C - \theta_1) \frac{\cos(\theta_1) \cos(\theta_2)}{\cos^2\left(\frac{\theta_1 + \theta_2}{2}\right)}, & \text{for p-p' or n-n'} \\ \Theta(\theta_C - \theta_1) \frac{\cos(\theta_1) \cos(\theta_2)}{\cos^2\left(\frac{\theta_1 + \theta_2}{2}\right)} e^{-\pi \hbar v_F d k_y^2 / U_0}, & \text{for p-n' or n-p'} \end{cases} \quad (\text{A.1})$$

where, E is the energy of the electron, θ_1 and θ_2 are the incident and refraction angle, θ_C is the critical angle from Snell's Law, d is the junction width, k_y is the transverse quasimomentum and U_0 is the potential barrier across the junction. Here, θ_1 and θ_2 is related by Snell's law [14] , $E \sin(\theta_1) = (E - U_0) \sin(\theta_2)$, arising from transverse quasimomentum ($k_y = k_1 \sin(\theta_1) = k_2 \sin(\theta_2)$) conservation. Here, $k_1 = \frac{E}{\hbar v_F}$ and $k_2 = \frac{E - U_0}{\hbar v_F}$ are the wave vectors on each side of the junction. For incident angles above critical angle, $\theta_C = \sin^{-1}(|(E - U_0)/E|)$, k_y cannot be conserved and T becomes zero.

Assuming non-interacting charge carriers, we consider a fraction T of each electron at the junction that passes through, while a fraction $1 - T$ is reflected back to the incident region. The trajectories of the reflected and transmitted fractional electrons are allowed to evolve once again through multiple such transmission-reflection events until they end up either at the source or the drain. The average transmission probability ($T_{ij} = N_j / N_{Total}$) from contact i to contact j is calculated by counting electrons (N_j) that eventually make it to the contact j for a given total number N_{Total} of carriers injected from contact i . Thereafter the Landauer-Büttiker formalism at low-bias is used to calculate channel conductance (G_{Ch}) by summing up the terminal transmissions.

$$G_{Ch}(E_F) = \frac{4q^2}{h} \int M(E) \bar{T}(E) \left(-\frac{\partial f_0}{\partial E} \right) dE \quad (\text{A.2})$$

where $q = 1.6 \times 10^{-19}$ C is the charge of an electron, h is the Planck's constant, E_F is the Fermi energy, M is the number of modes, \bar{T} is the sum over all transmissions, and $f_0 = f(E - E_F)$ is the equilibrium Fermi function.

Appendix B

Geometry improvement of Double Source (DS) device

The main motivation behind DS device in Ref. [59] was to use only junction in filtering procedure at the local gated region. In Fig. B.1(A), we can clearly see that this region is not free from edges and can be further optimized. Fig. B.1(B) shows the structure (DS_{imp}) to improve the device performance in presence of edge roughness. L_{ext} is kept to have feasible smooth electrostatics for both junction and reduce leakage path at the corners. Figure B.1(C) shows comparison between DS and DS_{imp} structure in terms of on-off ratio and we clearly see that DS_{imp} is less sensitive to edge roughness. This appendix is reproduced from supplementary materials of Ref. [87], with the permission of AIP Publishing coauthored with K. M. M. Habib, K. Wang, G. Lee, P. Kim, and A. W. Ghosh.

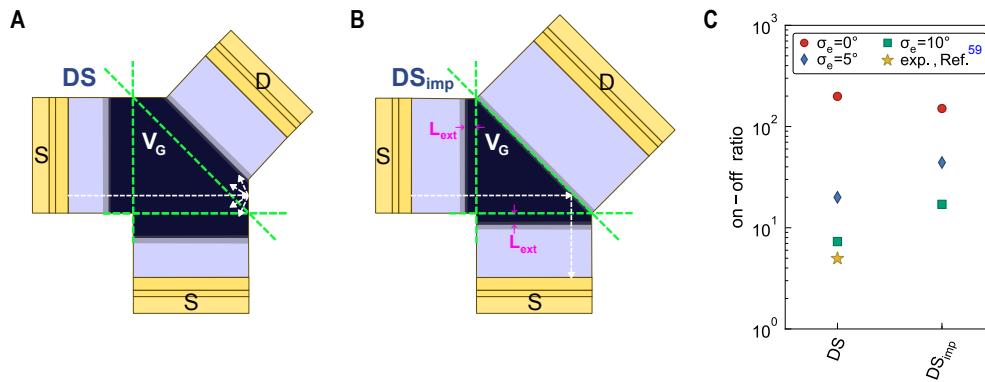


Figure B.1: **Improving DS device geometry.** (A) Device structure from Ref. [59]. (B) Improved device structure (DS_{imp}) to reduce edge roughness for reflected electrons from second junction. Ideally, the local gate should be restricted within the triangle enclosed by green dash line to make the region free from edges and electrons can be redirected to the other source by second junction shown by white dash lines. However, it is impossible to maintain smooth potential at the corners. Therefore, the left and bottom sides are kept extended ($L_{ext} = 100$ nm). (C) Comparison of on-off ratio of DS vs. DS_{imp}. DS_{imp} shows less sensitivity to edge roughness. Reproduced from Ref. [87], with the permission of AIP Publishing.

Appendix C

Non-Equilibrium Green's Function (NEGF) formalism

In a quantum transport simulation, the current is obtained using Landauers formula,

$$I = \frac{q}{h} \int T(E) [f_1(E, \mu_1) - f_2(E, \mu_2)] dE \quad (\text{C.1})$$

where $T(E)$ is the transmission spectrum between contacts 1 and 2, $f(E, \mu_i)$ is the Fermi function of contact i , q is the charge of an electron and h is Planck's constant. For numerical efficiency, we use the Recursive Green's function (RGF) algorithm [111] where the channel is divided into N blocks with block 1 connected to contact 1 and block N connected to contact 2. In this approach, the transmission is calculated using a computationally efficient Green's function formula,

$$T(E) = \text{tr}\{\Gamma_{11}[-2\text{Im}(G_{11}) - G_{11}\Gamma_{11}G_{11}^\dagger]\} \quad (\text{C.2})$$

where G_{11} is the Green's function for block 1 calculated using the RGF algorithm, and $\Gamma_{11} = -i(\Sigma_{11} - \Sigma_{11}^\dagger)$ with Σ_{ii} being the self-energy of contact i calculated using the decimation algorithm. In the above calculations, we obtain the Hamiltonian matrix using the modified approach for computational efficiency [112]. The electrostatic potential energy is modeled

by modifying the diagonal elements of the Hamiltonian matrix by $-qV_i$ where V_i is the electrostatic potential at site i . This appendix is reprinted with permission from SI of Ref. [88] coauthored with X. Zhou, A. Kerelsky, D. Wang, K .M. M. Habib, R. N. Sajjad, P. Agnihotri, J. U. Lee, A. W. Ghosh, F. M. Ross, and A. N. Pasupathy. Copyright 2019 American Chemical Society.

Appendix D

Publications

D.1 Journal Articles

1. K. Wang, M. Elahi, L. Wang, K. Habib, T. Taniguchi, K. Watanabe, J. Hone, G-H Lee, A. Ghosh, and P. Kim, “Graphene transistor based on tunable Dirac fermion optics”, *Proc. Natl. Acad. Sci. U.S.A.*, p. 201816119, 2019.
2. X. Zhou, A. Kerelsky, M. Elahi, D. Wang, K. Habib, R. Sajjad, P. Agnihotri, J. Lee, A. Ghosh, F. Ross, and A. Pasupathy, “Atomic scale characterization of graphene p-n junctions for electron-optical applications”, *ACS Nano*, vol. 13, no. 2, p. 2558, 2019.
3. M. Elahi, K. Habib, K. Wang, G-H Lee, P. Kim, and A. Ghosh, “Impact of geometry and non-idealities on electron ‘optics’ based graphene p-n junction devices”, *Appl. Phys. Lett.*, vol. 114, no. 1, p. 013507, 2019.
4. Y. Tan, M. Elahi, H-Y Tsao, K. Habib, N. Barker, and A. Ghosh, “Graphene Klein tunnel transistors for high speed analog RF applications”, *Sci. Rep.*, vol. 7, no. 1, p. 9714, 2017.

5. S. Chen, Z. Han, M. Elahi, K. Habib, L. Wang, B. Wen, Y. Gao, T. Taniguchi, K. Watanabe, J. Hone, A. Ghosh, and C. Dean, “Electron optics with p-n junctions in ballistic graphene”, *Science*, vol. 353, no. 6307, pp. 1522-1525, 2016.

D.2 Conferences Proceedings

1. M. Elahi, K. Habib, and A. Ghosh, “Gate tunable transport-gap to beat the Boltzmann limit: a Graphene Klein Tunnel Field Effect Transistor”, *5th Berkeley Symposium on Energy Efficient Electronic Systems & Steep Transistors Workshop (E3S)*, 2017.
2. M. Elahi, and A. Ghosh, “Current saturation and steep switching in graphene PN junctions using angle-dependent scattering”, *Device Research Conference (DRC)*, vol. 1, pp. 1-2, 2016.

Bibliography

- [1] K. S. Novoselov, A. K. Geim, S. V. Morozov, D. Jiang, Y. Zhang, S. V. Dubonos, I. V. Grigorieva, and A. A. Firsov, “Electric field effect in atomically thin carbon films,” *Science*, vol. 306, no. 5696, pp. 666–669, 2004.
- [2] S. Zhou, G.-H. Gweon, J. Graf, A. Fedorov, C. Spataru, R. Diehl, Y. Kopelevich, D.-H. Lee, S. G. Louie, and A. Lanzara, “First direct observation of dirac fermions in graphite,” *Nat. Phys.*, vol. 2, no. 9, pp. 595–599, 2006.
- [3] S. Morozov, K. Novoselov, M. Katsnelson, F. Schedin, D. Elias, J. A. Jaszczak, and A. Geim, “Giant intrinsic carrier mobilities in graphene and its bilayer,” *Phys. Rev. Lett.*, vol. 100, no. 1, p. 016602, 2008.
- [4] K. I. Bolotin, K. Sikes, Z. Jiang, M. Klima, G. Fudenberg, J. Hone, P. Kim, and H. Stormer, “Ultrahigh electron mobility in suspended graphene,” *Solid State Commun.*, vol. 146, no. 9, pp. 351–355, 2008.
- [5] L. Wang, I. Meric, P. Huang, Q. Gao, Y. Gao, H. Tran, T. Taniguchi, K. Watanabe, L. Campos, D. Muller, *et al.*, “One-dimensional electrical contact to a two-dimensional material,” *Science*, vol. 342, no. 6158, pp. 614–617, 2013.
- [6] A. A. Balandin, S. Ghosh, W. Bao, I. Calizo, D. Teweldebrhan, F. Miao, and C. N. Lau, “Superior thermal conductivity of single-layer graphene,” *Nano Lett.*, vol. 8, no. 3, pp. 902–907, 2008.
- [7] C. Lee, X. Wei, J. W. Kysar, and J. Hone, “Measurement of the elastic properties and intrinsic strength of monolayer graphene,” *Science*, vol. 321, no. 5887, pp. 385–388, 2008.
- [8] R. R. Nair, P. Blake, A. N. Grigorenko, K. S. Novoselov, T. J. Booth, T. Stauber, N. M. Peres, and A. K. Geim, “Fine structure constant defines visual transparency of graphene,” *Science*, vol. 320, no. 5881, pp. 1308–1308, 2008.
- [9] A. L. Grushina, D.-K. Ki, and A. F. Morpurgo, “A ballistic pn junction in suspended graphene with split bottom gates,” *Appl. Phys. Lett.*, vol. 102, no. 22, p. 223102, 2013.
- [10] P. Rickhaus, R. Maurand, M.-H. Liu, M. Weiss, K. Richter, and C. Schönenberger, “Ballistic interferences in suspended graphene,” *Nat. Commun.*, vol. 4, no. 2342, 2013.

- [11] V. Calado, S.-E. Zhu, S. Goswami, Q. Xu, K. Watanabe, T. Taniguchi, G. C. Janssen, and L. Vandersypen, “Ballistic transport in graphene grown by chemical vapor deposition,” *Appl. Phys. Lett.*, vol. 104, no. 2, p. 023103, 2014.
- [12] C. R. Dean, A. F. Young, I. Meric, C. Lee, L. Wang, S. Sorgenfrei, K. Watanabe, T. Taniguchi, P. Kim, K. L. Shepard, *et al.*, “Boron nitride substrates for high-quality graphene electronics,” *Nat. Nanotechnol.*, vol. 5, no. 10, pp. 722–726, 2010.
- [13] F. Amet, J. Williams, K. Watanabe, T. Taniguchi, and D. Goldhaber-Gordon, “Insulating behavior at the neutrality point in single-layer graphene,” *Phys. Rev. Lett.*, vol. 110, no. 21, p. 216601, 2013.
- [14] V. V. Cheianov, V. Fal’ko, and B. Altshuler, “The focusing of electron flow and a veselago lens in graphene pn junctions,” *Science*, vol. 315, no. 5816, pp. 1252–1255, 2007.
- [15] J. Cserti, A. Pályi, and C. Péterfalvi, “Caustics due to a negative refractive index in circular graphene p- n junctions,” *Phys. Rev. Lett.*, vol. 99, no. 24, p. 246801, 2007.
- [16] V. G. Veselago, “The electrodynamics of substances with simultaneously negative values of ϵ and μ ,” *Sov. Phys.-Uspekhi*, vol. 10, no. 4, p. 509, 1968.
- [17] M. Katsnelson, K. Novoselov, and A. Geim, “Chiral tunnelling and the klein paradox in graphene,” *Nat. Phys.*, vol. 2, no. 9, pp. 620–625, 2006.
- [18] S. Sutar, E. Comfort, J. Liu, T. Taniguchi, K. Watanabe, and J. Lee, “Angle-dependent carrier transmission in graphene p–n junctions,” *Nano Lett.*, vol. 12, no. 9, pp. 4460–4464, 2012.
- [19] D. Dragoman and M. Dragoman, “Optical analogue structures to mesoscopic devices,” *Prog. Quantum Electron*, vol. 23, no. 4, pp. 131–188, 1999.
- [20] H. van Houten and C. Beenakker, *Confined Electrons and Photons*. Springer, 1995.
- [21] J. Spector, H. Stormer, K. Baldwin, L. Pfeiffer, and K. West, “Electron focusing in two-dimensional systems by means of an electrostatic lens,” *Appl. Phys. Lett.*, vol. 56, no. 13, pp. 1290–1292, 1990.
- [22] U. Sivan, M. Heiblum, C. Umbach, and H. Shtrikman, “Electrostatic electron lens in the ballistic regime,” *Phys. Rev. B*, vol. 41, no. 11, p. 7937, 1990.
- [23] C.-H. Park, Y.-W. Son, L. Yang, M. L. Cohen, and S. G. Louie, “Electron beam supercollimation in graphene superlattices,” *Nano Lett.*, vol. 8, no. 9, pp. 2920–2924, 2008.
- [24] M. S. Jang, H. Kim, Y.-W. Son, H. A. Atwater, and W. A. Goddard, “Graphene field effect transistor without an energy gap,” *Proc. Natl. Acad. Sci. U.S.A.*, vol. 110, no. 22, pp. 8786–8789, 2013.

- [25] Q. Wilmart, S. Berrada, D. Torrin, V. H. Nguyen, G. Fève, J.-M. Berroir, P. Dollfus, and B. Plaçais, “A klein-tunneling transistor with ballistic graphene,” *2D Mater.*, vol. 1, no. 1, p. 011006, 2014.
- [26] P. Rickhaus, P. Makk, M.-H. Liu, K. Richter, and C. Schönenberger, “Gate tuneable beamsplitter in ballistic graphene,” *Appl. Phys. Lett.*, vol. 107, no. 25, p. 251901, 2015.
- [27] V. M. Shalaev, “Optical negative-index metamaterials,” *Nat. Photonics*, vol. 1, no. 1, pp. 41–48, 2007.
- [28] J. B. Pendry, “Negative refraction makes a perfect lens,” *Phys. Rev. Lett.*, vol. 85, no. 18, p. 3966, 2000.
- [29] R. A. Shelby, D. R. Smith, and S. Schultz, “Experimental verification of a negative index of refraction,” *Science*, vol. 292, no. 5514, pp. 77–79, 2001.
- [30] N. Fang, H. Lee, C. Sun, and X. Zhang, “Sub-diffraction-limited optical imaging with a silver superlens,” *Science*, vol. 308, no. 5721, pp. 534–537, 2005.
- [31] D. Schurig, J. Mock, B. Justice, S. A. Cummer, J. B. Pendry, A. Starr, and D. Smith, “Metamaterial electromagnetic cloak at microwave frequencies,” *Science*, vol. 314, no. 5801, pp. 977–980, 2006.
- [32] S. Chen, Z. Han, M. M. Elahi, K. M. Habib, L. Wang, B. Wen, Y. Gao, T. Taniguchi, K. Watanabe, J. Hone, A. W. Ghosh, and C. R. Dean, “Electron optics with p-n junctions in ballistic graphene,” *Science*, vol. 353, no. 6307, pp. 1522–1525, 2016.
- [33] J. Williams, T. Low, M. Lundstrom, and C. Marcus, “Gate-controlled guiding of electrons in graphene,” *Nat. Nanotechnol.*, vol. 6, no. 4, pp. 222–225, 2011.
- [34] T. Taychatanapat, J. Y. Tan, Y. Yeo, K. Watanabe, T. Taniguchi, and B. zyilmaz, “Conductance oscillations induced by ballistic snake states in a graphene heterojunction,” *Nat. Commun.*, vol. 6, no. 6093, 2015.
- [35] V. V. Cheianov and V. I. Fal’ko, “Selective transmission of dirac electrons and ballistic magnetoresistance of n- p junctions in graphene,” *Phys. Rev. B*, vol. 74, no. 4, p. 041403, 2006.
- [36] B. Huard, J. Sulpizio, N. Stander, K. Todd, B. Yang, and D. Goldhaber-Gordon, “Transport measurements across a tunable potential barrier in graphene,” *Phys. Rev. Lett.*, vol. 98, no. 23, p. 236803, 2007.
- [37] R. V. Gorbachev, A. S. Mayorov, A. K. Savchenko, D. W. Horsell, and F. Guinea, “Conductance of pnp graphene structures with air-bridge top gates,” *Nano Lett.*, vol. 8, no. 7, pp. 1995–1999, 2008.
- [38] A. F. Young and P. Kim, “Quantum interference and klein tunnelling in graphene heterojunctions,” *Nat. Phys.*, vol. 5, no. 3, pp. 222–226, 2009.

- [39] N. Stander, B. Huard, and D. Goldhaber-Gordon, “Evidence for klein tunneling in graphene p- n junctions,” *Phys. Rev. Lett.*, vol. 102, no. 2, p. 026807, 2009.
- [40] R. N. Sajjad, S. Sutar, J. Lee, and A. W. Ghosh, “Manifestation of chiral tunneling at a tilted graphene p-n junction,” *Phys. Rev. B*, vol. 86, no. 15, p. 155412, 2012.
- [41] P. Rickhaus, P. Makk, M.-H. Liu, E. Tóvári, M. Weiss, R. Maurand, K. Richter, and C. Schönemberger, “Snake trajectories in ultraclean graphene p–n junctions,” *Nat. Commun.*, vol. 6, p. 6470, 2015.
- [42] M. Topinka, B. LeRoy, R. Westervelt, S. Shaw, R. Fleischmann, E. Heller, K. Maranowski, and A. Gossard, “Coherent branched flow in a two-dimensional electron gas,” *Nature*, vol. 410, no. 6825, pp. 183–186, 2001.
- [43] K. E. Aidala, R. E. Parrott, T. Kramer, E. Heller, R. Westervelt, M. P. Hanson, and A. C. Gossard, “Imaging magnetic focusing of coherent electron waves,” *Nat. Phys.*, vol. 3, no. 7, pp. 464–468, 2007.
- [44] J. Baringhaus, A. Stöhr, S. Forti, U. Starke, and C. Tegenkamp, “Ballistic bipolar junctions in chemically gated graphene ribbons,” *Sci. Rep.*, vol. 5, p. 9955, 2015.
- [45] T. Taychatanapat, K. Watanabe, T. Taniguchi, and P. Jarillo-Herrero, “Electrically tunable transverse magnetic focusing in graphene,” *Nat. Phys.*, vol. 9, no. 4, pp. 225–229, 2013.
- [46] C. Beenakker and H. Van Houten, “Billiard model of a ballistic multiprobe conductor,” *Phys. Rev. Lett.*, vol. 63, no. 17, p. 1857, 1989.
- [47] S. Milovanović, M. Ramezani Masir, and F. Peeters, “Magnetic electron focusing and tuning of the electron current with a pn-junction,” *J. Appl. Phys.*, vol. 115, no. 4, p. 043719, 2014.
- [48] J. Cayssol, B. Huard, and D. Goldhaber-Gordon, “Contact resistance and shot noise in graphene transistors,” *Phys. Rev. B*, vol. 79, no. 7, p. 075428, 2009.
- [49] G.-H. Lee, G.-H. Park, and H.-J. Lee, “Observation of negative refraction of dirac fermions in graphene,” *Nat. Phys.*, vol. 11, no. 11, pp. 925–929, 2015.
- [50] A. C. Seabaugh and Q. Zhang, “Low-voltage tunnel transistors for beyond cmos logic,” *Proc. IEEE*, vol. 98, no. 12, pp. 2095–2110, 2010.
- [51] S. Salahuddin and S. Datta, “Use of negative capacitance to provide voltage amplification for low power nanoscale devices,” *Nano Lett.*, vol. 8, no. 2, pp. 405–410, 2008.
- [52] N. Shukla, A. V. Thathachary, A. Agrawal, H. Paik, A. Aziz, D. G. Schlom, S. K. Gupta, R. Engel-Herbert, and S. Datta, “A steep-slope transistor based on abrupt electronic phase transition,” *Nat. Commun.*, vol. 6, p. 7812, 2015.

- [53] H. Kam, D. T. Lee, R. T. Howe, and T.-J. King, "A new nano-electro-mechanical field effect transistor (nemfet) design for low-power electronics," in *Electron Devices Meeting, 2005. IEDM Technical Digest. IEEE International*, pp. 463–466, IEEE, 2005.
- [54] S. Das, "Two dimensional electrostrictive field effect transistor (2d-efet): A sub-60mv/decade steep slope device with high on current," *Sci. Rep.*, vol. 6, 2016.
- [55] R. N. Sajjad and A. W. Ghosh, "High efficiency switching using graphene based electron "optics"," *Appl. Phys. Lett.*, vol. 99, no. 12, p. 123101, 2011.
- [56] A. W. Ghosh, "Transmission engineering as a route to subthermal switching," *IEEE J. Electron Devices Soc.*, vol. 3, no. 3, pp. 135–143, 2015.
- [57] M. M. Elahi, K. M. M. Habib, and A. W. Ghosh, "Gate tunable transport-gap to beat the boltzmann limit: a graphene klein tunnel field effect transistor," in *5th Berkeley Symposium on Energy Efficient Electronic Systems (E3S)*, IEEE, 2017.
- [58] Y. Tan, M. M. Elahi, H.-Y. Tsao, K. Habib, N. S. Barker, and A. W. Ghosh, "Graphene klein tunnel transistors for high speed analog rf applications," *Sci. Rep.*, vol. 7, no. 9714, 2017.
- [59] K. Wang, M. M. Elahi, L. Wang, K. M. Habib, T. Taniguchi, K. Watanabe, J. Hone, A. W. Ghosh, G.-H. Lee, and P. Kim, "Graphene transistor based on tunable dirac fermion optics," *Proc. Natl. Acad. Sci. U.S.A.*, p. 201816119, 2019.
- [60] R. N. Sajjad and A. W. Ghosh, "Manipulating chiral transmission by gate geometry: switching in graphene with transmission gaps," *ACS Nano*, vol. 7, no. 11, pp. 9808–9813, 2013.
- [61] M. M. Elahi and A. W. Ghosh, "Current saturation and steep switching in graphene pn junctions using angle-dependent scattering," in *Device Research Conference (DRC), 2016 74th Annual*, pp. 1–2, IEEE, 2016.
- [62] S. Morikawa, Q. Wilmart, S. Masubuchi, K. Watanabe, T. Taniguchi, B. Plaças, and T. Machida, "Dirac fermion reflector by ballistic graphene sawtooth-shaped npn junctions," *Semicond. Sci. Technol.*, vol. 32, no. 4, p. 045010, 2017.
- [63] F. Schwierz, "Graphene transistors," *Nat. Nanotechnol.*, vol. 5, no. 7, pp. 487–496, 2010.
- [64] F. Schwierz, "Graphene transistors: status, prospects, and problems," *Proc. IEEE*, vol. 101, no. 7, pp. 1567–1584, 2013.
- [65] G. Fiori, F. Bonaccorso, G. Iannaccone, T. Palacios, D. Neumaier, A. Seabaugh, S. K. Banerjee, and L. Colombo, "Electronics based on two-dimensional materials," *Nat. Nanotechnol.*, vol. 9, no. 10, pp. 768–779, 2014.
- [66] J. Chauhan and J. Guo, "Assessment of high-frequency performance limits of graphene field-effect transistors," *Nano Res.*, vol. 4, no. 6, pp. 571–579, 2011.

- [67] J.-H. Chen, C. Jang, S. Xiao, M. Ishigami, and M. S. Fuhrer, “Intrinsic and extrinsic performance limits of graphene devices on SiO_2 ,” *Nat. Nanotechnol.*, vol. 3, no. 4, pp. 206–209, 2008.
- [68] Y. Wu, K. A. Jenkins, A. Valdes-Garcia, D. B. Farmer, Y. Zhu, A. A. Bol, C. Dimitrakopoulos, W. Zhu, F. Xia, P. Avouris, *et al.*, “State-of-the-art graphene high-frequency electronics,” *Nano Lett.*, vol. 12, no. 6, pp. 3062–3067, 2012.
- [69] R. Cheng, J. Bai, L. Liao, H. Zhou, Y. Chen, L. Liu, Y.-C. Lin, S. Jiang, Y. Huang, and X. Duan, “High-frequency self-aligned graphene transistors with transferred gate stacks,” *Proc. Natl. Acad. Sci. U.S.A.*, vol. 109, no. 29, pp. 11588–11592, 2012.
- [70] Z. Guo, R. Dong, P. S. Chakraborty, N. Lourenco, J. Palmer, Y. Hu, M. Ruan, J. Hankinson, J. Kunc, J. D. Cressler, *et al.*, “Record maximum oscillation frequency in c-face epitaxial graphene transistors,” *Nano Lett.*, vol. 13, no. 3, pp. 942–947, 2013.
- [71] Z. H. Ni, T. Yu, Y. H. Lu, Y. Y. Wang, Y. P. Feng, and Z. X. Shen, “Uniaxial strain on graphene: Raman spectroscopy study and band-gap opening,” *ACS Nano*, vol. 2, no. 11, pp. 2301–2305, 2008.
- [72] M. Y. Han, B. Özyilmaz, Y. Zhang, and P. Kim, “Energy band-gap engineering of graphene nanoribbons,” *Phys. Rev. Lett.*, vol. 98, no. 20, p. 206805, 2007.
- [73] V. Perebeinos and P. Avouris, “Inelastic scattering and current saturation in graphene,” *Phys. Rev. B*, vol. 81, no. 19, p. 195442, 2010.
- [74] I. Meric, N. Baklitskaya, P. Kim, and K. L. Shepard, “Rf performance of top-gated, zero-bandgap graphene field-effect transistors,” in *Electron Devices Meeting, (IEDM) 2008. IEEE International*, pp. 1–4, IEEE, 2008.
- [75] K. Brenner and R. Murali, “Single step, complementary doping of graphene,” *Appl. Phys. Lett.*, vol. 96, no. 6, p. 063104, 2010.
- [76] B. Tang, H. Guoxin, and H. Gao, “Raman spectroscopic characterization of graphene,” *Appl. Spectrosc. Rev.*, vol. 45, no. 5, pp. 369–407, 2010.
- [77] L. Liao, Y.-C. Lin, M. Bao, R. Cheng, J. Bai, Y. Liu, Y. Qu, K. L. Wang, Y. Huang, and X. Duan, “High-speed graphene transistors with a self-aligned nanowire gate,” *Nature*, vol. 467, no. 7313, pp. 305–308, 2010.
- [78] R. N. Sajjad, F. Tseng, K. M. Habib, and A. W. Ghosh, “Quantum transport at the Dirac point: Mapping out the minimum conductivity from pristine to disordered graphene,” *Phys. Rev. B*, vol. 92, no. 20, p. 205408, 2015.
- [79] Y.-M. Lin, K. Jenkins, D. Farmer, A. Valdes-Garcia, P. Avouris, C.-Y. Sung, H.-Y. Chiu, and B. Ek, “Development of graphene FETs for high frequency electronics,” in *Electron Devices Meeting (IEDM), 2009 IEEE International*, pp. 1–4, IEEE, 2009.

- [80] Y.-M. Lin, C. Dimitrakopoulos, K. A. Jenkins, D. B. Farmer, H.-Y. Chiu, A. Grill, and P. Avouris, “100-ghz transistors from wafer-scale epitaxial graphene,” *Science*, vol. 327, no. 5966, pp. 662–662, 2010.
- [81] I. Meric, C. R. Dean, S.-J. Han, L. Wang, K. A. Jenkins, J. Hone, and K. Shepard, “High-frequency performance of graphene field effect transistors with saturating iv-characteristics,” in *Electron Devices Meeting (IEDM), 2011 IEEE International*, pp. 1–2, IEEE, 2011.
- [82] C. Rutherglen, D. Jain, and P. Burke, “Nanotube electronics for radiofrequency applications,” *Nat. Nanotechnol.*, vol. 4, no. 12, pp. 811–819, 2009.
- [83] M.-H. Liu, C. Gorini, K. Richter, *et al.*, “Creating and steering highly directional electron beams in graphene,” *Phys. Rev. Lett.*, vol. 118, no. 6, p. 066801, 2017.
- [84] G. Giovannetti, P. Khomyakov, G. Brocks, V. v. Karpan, J. Van den Brink, and P. J. Kelly, “Doping graphene with metal contacts,” *Phys. Rev. Lett.*, vol. 101, no. 2, p. 026803, 2008.
- [85] S. Milovanović, M. Ramezani Masir, and F. Peeters, “Spectroscopy of snake states using a graphene hall bar,” *Appl. Phys. Lett.*, vol. 103, no. 23, p. 233502, 2013.
- [86] T. Low, S. Hong, J. Appenzeller, S. Datta, and M. S. Lundstrom, “Conductance asymmetry of graphene pn junction,” *IEEE Trans. Electron Devices*, vol. 56, no. 6, pp. 1292–1299, 2009.
- [87] M. M. Elahi, K. Masum Habib, K. Wang, G.-H. Lee, P. Kim, and A. W. Ghosh, “Impact of geometry and non-idealities on electron optics based graphene pn junction devices,” *Appl. Phys. Lett.*, vol. 114, no. 1, p. 013507, 2019.
- [88] X. Zhou, A. Kerelsky, M. M. Elahi, D. Wang, K. M. Habib, R. N. Sajjad, P. Agnihotri, J. U. Lee, A. W. Ghosh, F. M. Ross, *et al.*, “Atomic scale characterization of graphene pn junctions for electron-optical applications,” *ACS Nano*, vol. 13, no. 2, pp. 2558–2566, 2019.
- [89] C. Gutiérrez, L. Brown, C.-J. Kim, J. Park, and A. N. Pasupathy, “Klein tunnelling and electron trapping in nanometre-scale graphene quantum dots,” *Nat. Phys.*, vol. 12, no. 11, pp. 1069–1075, 2016.
- [90] M. A. Yamoah, W. Yang, E. Pop, and D. Goldhaber-Gordon, “High-velocity saturation in graphene encapsulated by hexagonal boron nitride,” *ACS Nano*, vol. 11, no. 10, pp. 9914–9919, 2017.
- [91] A. Y. Serov, Z.-Y. Ong, M. V. Fischetti, and E. Pop, “Theoretical analysis of high-field transport in graphene on a substrate,” *J. Appl. Phys.*, vol. 116, no. 3, p. 034507, 2014.
- [92] E. Sichel, R. Miller, M. Abrahams, and C. Buiocchi, “Heat capacity and thermal conductivity of hexagonal pyrolytic boron nitride,” *Phys. Rev. B*, vol. 13, no. 10, p. 4607, 1976.

- [93] C.-H. Park, L. Yang, Y.-W. Son, M. L. Cohen, and S. G. Louie, “Anisotropic behaviours of massless dirac fermions in graphene under periodic potentials,” *Nat. Phys.*, vol. 4, no. 3, p. 213, 2008.
- [94] C. Forsythe, X. Zhou, K. Watanabe, T. Taniguchi, A. Pasupathy, P. Moon, M. Koshino, P. Kim, and C. R. Dean, “Band structure engineering of 2d materials using patterned dielectric superlattices,” *Nat. Nanotechnol.*, vol. 13, pp. 566–571, 2018.
- [95] N. A. Bruque, R. R. Pandey, and R. K. Lake, “Electron transport through a conjugated molecule with carbon nanotube leads,” *Phys. Rev. B*, vol. 76, no. 20, p. 205322, 2007.
- [96] H. van Houten and C. W. J. Beenakker, *Confined Electrons and Photons: New Physics and Applications*, vol. 340. Springer US: Boston, MA, 1 ed., 1995. E. Burstein, C. Weisbuch, Eds.
- [97] H. Van Houten, C. Beenakker, J. Williamson, M. Broekaart, P. Van Loosdrecht, B. Van Wees, J. Mooij, C. Foxon, and J. Harris, “Coherent electron focusing with quantum point contacts in a two-dimensional electron gas,” *Phys. Rev. B*, vol. 39, no. 12, p. 8556, 1989.
- [98] L. Molenkamp, A. Staring, C. Beenakker, R. Eppenga, C. Timmering, J. Williamson, C. Harmans, and C. Foxon, “Electron-beam collimation with a quantum point contact,” *Phys. Rev. B*, vol. 41, no. 2, p. 1274, 1990.
- [99] M. Kim, J.-H. Choi, S.-H. Lee, K. Watanabe, T. Taniguchi, S.-H. Jhi, and H.-J. Lee, “Valley-symmetry-preserved transport in ballistic graphene with gate-defined carrier guiding,” *Nat. Phys.*, vol. 12, no. 11, p. 1022, 2016.
- [100] A. W. Barnard, A. Hughes, A. L. Sharpe, K. Watanabe, T. Taniguchi, and D. Goldhaber-Gordon, “Absorptive pinhole collimators for ballistic dirac fermions in graphene,” *Nat. Commun.*, vol. 8, p. 15418, 2017.
- [101] A. Vakil and N. Engheta, “Transformation optics using graphene,” *Science*, vol. 332, no. 6035, pp. 1291–1294, 2011.
- [102] C. G. Péterfalvi, L. Oroszlány, C. J. Lambert, and J. Cserti, “Intraband electron focusing in bilayer graphene,” *New J. Phys.*, vol. 14, no. 6, p. 063028, 2012.
- [103] B. Özyilmaz, P. Jarillo-Herrero, D. Efetov, D. A. Abanin, L. S. Levitov, and P. Kim, “Electronic transport and quantum hall effect in bipolar graphene p-n-p junctions,” *Phys. Rev. Lett.*, vol. 99, no. 16, p. 166804, 2007.
- [104] B. Schmidt, K. Bennaceur, S. Bilodeau, G. Gervais, L. Pfeiffer, and K. West, “Second landau level fractional quantum hall effects in the corbino geometry,” *Solid State Commun.*, vol. 217, pp. 1–5, 2015.
- [105] J. Yan and M. S. Fuhrer, “Charge transport in dual gated bilayer graphene with corbino geometry,” *Nano Lett.*, vol. 10, no. 11, pp. 4521–4525, 2010.

-
- [106] Y. Zhao, P. Cadden-Zimansky, F. Ghahari, and P. Kim, “Magnetoresistance measurements of graphene at the charge neutrality point,” *Phys. Rev. Lett.*, vol. 108, no. 10, p. 106804, 2012.
- [107] E. C. Peters, A. Giesbers, M. Burghard, and K. Kern, “Scaling in the quantum hall regime of graphene corbino devices,” *Appl. Phys. Lett.*, vol. 104, no. 20, p. 203109, 2014.
- [108] M. Kumar, A. Laitinen, and P. Hakonen, “Unconventional fractional quantum hall states and wigner crystallization in suspended corbino graphene,” *Nat. Commun.*, vol. 9, no. 1, p. 2776, 2018.
- [109] G. Kirczenow, “Quantum transport in ballistic nano-scale corbino disks,” *J. Phys.: Cond. Matt.*, vol. 6, no. 39, p. L583, 1994.
- [110] Z. Tan, C. Tan, L. Ma, G. Liu, L. Lu, and C. Yang, “Shubnikov-de haas oscillations of a single layer graphene under dc current bias,” *Phys. Rev. B*, vol. 84, no. 11, p. 115429, 2011.
- [111] N. A. Bruque, M. Ashraf, G. J. Beran, T. R. Helander, and R. K. Lake, “Conductance of a conjugated molecule with carbon nanotube contacts,” *Phys. Rev. B*, vol. 80, no. 15, p. 155455, 2009.
- [112] K. M. Habib, R. N. Sajjad, and A. W. Ghosh, “Modified dirac hamiltonian for efficient quantum mechanical simulations of micron sized devices,” *Appl. Phys. Lett.*, vol. 108, no. 11, p. 113105, 2016.